TECHNISCHE UNIVERSITÄT WIEN

ATOMINSTITUT

DIPLOMARBEIT

Comparative Analysis of sCVD, SiC, and Si Detectors for Neutron Measurements in Nuclear Fusion

zur Erlangung des akademischen Grades

Diplom-Ingenieur

im Rahmen des Studiums

Masterstudium Technische Physik

eingereicht von

Julian Melbinger

Matrikelnummer 11802601

ausgeführt am

Atominstitut

der Fakultät für Physik

der Technischen Universität Wien

unter der Anleitung von

Priv.-Doz. Dipl.-Ing. Dr. Stephan Sponar

Ass.Prof. Dipl.-Ing. Dr.techn. Erwin Jericha

Wien, am 07.05.2024 Unterschrift Verfasser Unterschrift Betreuer

Die approbierte gedruckte Originalversion dieser Diplomarbeit ist an der TU Wien Bibliothek verfügbar
The approved original version of this thesis is available in print at TU Wien Bibliothek.

TU Bibliothek Your knowledge hub WIEN

Zusammenfassung

Die Vision von Kernfusion als saubere Energiequelle galt jahrzehntelang als „noch 30 Jahre entfernt“. Diese Perspektive wandelt sich nun rapide, und angesichts des drängenden Bedarfs an nachhaltigen Energien könnte Kernfusion bald Wirklichkeit werden. Herausforderungen, insbesondere die Plasma-Kontrolle in Fusionsreaktoren, bleiben bestehen. Zur Überwindung dieser Hürden kommen verschiedenste Plasmadiagnostiken zum Einsatz, darunter die Neutronendiagnostik, die Materialien erfordert, die als Neutronenkonverter und Sensor dienen. Drei Materialien wurden hierfür in dieser Arbeit evaluiert: Silizium (Si), einkristalliner CVD-Diamant (sCVD) und Siliziumkarbid (SiC).

Die Untersuchungen für die vorliegende Arbeit wurden in Athen bei NCSR "Demokritos" druchgeführt. Hierfür wurden Messungen mit monoenergtischen Neutronen durchgeführt. Es wurden Messungen bei 2.45 MeV (entspricht der Deuterium-Deuterium-Fusion), 2.95 MeV, 3.45 MeV und 3.95 MeV durchgeführt, um die Detektoren eingehend zu analysieren. Die Detektorantworten wurden mit Monte-Carlo Geant4 Simulationen abgeglichen.

Ein spektroskopischer Verstärker und ein Digitalisierungssystem mit 14-Bit-Auflösung wurden entwickelt, um die Messungen zu ermöglichen. Ein BF_3-Zähler diente als Referenzdetektor zum Vergleich der Neutronenantwortfunktionen der Detektoren bei unterschiedlichen Energien.

Der sCVD-Detektor zeigte sich aufgrund höherer Neutronendetektion und besserer γ-Untergrundunterdrückung dem SiC-Detektor überlegen. Der Si-Detektor wurde wegen seiner γ-Empfindlichkeit und mangelnder neutroneninduzierter Antwort ausgeschlossen.

Die approbierte gedruckte Originalversion dieser Diplomarbeit ist an der TU Wien Bibliothek verfügbar
The approved original version of this thesis is available in print at TU Wien Bibliothek.

Abstract

"Nuclear fusion is always 30 years away" was for a long time the answer to any nuclear fusion related question. But a green and sustainable energy source is needed more then ever before. Nuclear fusion is close to being a reality, but some challenges still remain. One remaining challenge is the control of the plasma inside the reactor, which uses different diagnostic systems. Neutron diagnostics are one of the diagnostics utilised and are therefore of great interest for future large scale fusion reactors. Ideally the sensor material acts as neutron converter and sensor at the same time. Three contestants are in consideration, a silicon detector (Si), a single-crystal CVD diamond detector (sCVD) or a silicon-carbide detector (SiC).

This works has used monoenergetic neutron beams at NCSR “Demokritos” in Athens to compare the three detector contestants at four different neutron energies, one being 2.45 MeV, precisely the neutron energy in Deuterium-Deuterium fusion. To gain a deeper understanding, three additional neutron energies, 2.95 MeV, 3.45 MeV and 3.95 MeV, were also investigated. To do so, the response function of each detector was measured and processed to obtain the measured neutron response function. Additionally, the neutron response function was subsequently compared with GEANT4 simulations.

For this purpose, a spectroscopic amplifier was developed and characterised and a new digitizer system was developed to take the data with 14-bit resolution. Furthermore is the data analysis described in great detail in this work. A BF_3 counter was used as a reference detector to compare the detectors and to compare the measured neutron response functions of the detectors at different neutron energies.

The sCVD detector performance was found to be superior to the SiC detector due to its higher identifiable neutron count percentage as well as a better γ-background rejection. The Si detector was discarded as a contestant due to its γ sensitivity and lack of neutron induced response function feature.

Die approbierte gedruckte Originalversion dieser Diplomarbeit ist an der TU Wien Bibliothek verfügbar
The approved original version of this thesis is available in print at TU Wien Bibliothek.
TU Bibliothek Your knowledge hub WIEN

Contents

Die approbierte gedruckte Originalversion dieser Diplomarbeit ist an der TU Wien Bibliothek verfügbar
The approved original version of this thesis is available in print at TU Wien Bibliothek.
TU Bibliothek Your knowledge hub WIEN

Die approbierte gedruckte Originalversion dieser Diplomarbeit ist an der TU Wien Bibliothek verfügbar
The approved original version of this thesis is available in print at TU Wien Bibliothek.

Chapter 1

Introduction

Climate change is one, if not the most important challenge humanity faces today. Nuclear fusion has long been seen as a dream for clean abundant energy but was still years away from a working reactor. But now, nuclear fusion could be achievable in this decade. Some challenges to have a stable nuclear fusion plasma which can generate power 24/7 still remain. One of the biggest challenges is to have precise control of the plasma itself to suppress any plasma instabilities. As every detector directly mounted in the inner plasma vessel takes up space which could be used for power generation, plasma diagnostics outside the main vessel are needed. Neutron diagnostics could be well suited, as neutrons interact only weakly with the surrounding materials. Using the neutron flux, the plasma temperature can be inferred as well as the number of fusion events and additional plasma related parameters [1]. Detecting neutrons is difficult and often a converter from neutrons to a charged particle, like protons, is required. A material capable of acting as both neutron converter and detector would therefore be the ideal choice. Three different detector materials are presently the best contestants:

1. A silicon detector (Si).
2. A single-crystal CVD diamond detector (sCVD).
3. A silicon-carbide detector (SiC).

This work used a monoenergetic neutron beam at the NCSR "Demokritos" facility in Athens [2] to compare the three detector contestants at neutron energies of 2.45 MeV, 2.95 MeV, 3.45 MeV and 3.95 MeV, respectively. Especially the first neutron energy is of great interest as it is the energy of neutrons produced in Deuterium-Deuterium (DD) nuclear fusion. Therefore, twelve different measurements are presented and compared to investigate the detectors in regards to their neutron detection capabilities. This is done by recording the response function of

Die approbierte gedruckte Originalversion dieser Diplomarbeit ist an der TU Wien Bibliothek verfügbar
The approved original version of this thesis is available in print at TU Wien Bibliothek.

the detector, meaning the deposited energy in the detector is recorded and histogrammed. This data is then processed to obtain the measured neutron response function which should ideally include only neutron counts. Due to the nature of any neutron experiment, γ-background is always present which cannot be distinguished from neutron interactions. This results in a measured neutron response function which also includes γ counts. To ensure a rigorous comparison between detectors, a threshold energy is chosen, assigning all counts above it to neutron interactions, called identifiable neutron counts. This threshold must be derived from the respective neutron response function, therefore demanding a neutron induced feature in it. The three obtained stages of data processing are therefore:

1. **Detector response function:** The measured deposited energy spectrum.
2. **Measured neutron response function:** The processed spectrum to obtain only counts from neutron interactions and the γ-background.
3. **Identifiable neutron counts:** All counts which are above a chosen threshold and are counted as neutron interactions.

To allow for a precise comparison, an established CIVIDEC CxL Spectroscopic Amplifier [3] was modified and characterised and a new digitizer generation was developed. Accompanying GEANT4 simulations were used to qualify the obtained measured neutron response functions. These were then compared to a reference boron trifluoride (BF_3) neutron counter permanently installed at Demokritos to calculate a relative neutron detection efficiency (ϵ). Combining all the aforementioned aspects, a rigorous study of the three detector contenders was conducted to determine the most suitable candidate for future fusion neutron diagnostics.

1.1 Neutron diagnostic for nuclear fusion

Nuclear fusion uses either a Deuterium-Deuterium (DD) or a Deuterium-Tritium mixture. When using DD plasma, neutrons with an energy of 2.45 MeV are produced, compared to 14.1 MeV neutrons from DT plasma. Neutron diagnostics are therefore a frequently chosen method to obtain a wide range of plasma parameters, as neutrons do not interact with the plasma and can leave the strong magnetic field in nuclear fusion plasma's undisturbed. Neutron diagnostics are utilised to obtain various parameters such as the neutron flux, fusion power, neutron profile, and ion temperature [4].

Die approbierte gedruckte Originalversion dieser Diplomarbeit ist an der TU Wien Bibliothek verfügbar
The approved original version of this thesis is available in print at TU Wien Bibliothek.
TU Bibliothek Your knowledge hub WIEN

To date, the International Thermonuclear Experimental Reactor (ITER) is the most ambitious project to achieve stable nuclear fusion and generate excess energy. Therefore the neutron diagnostics planned for ITER are in active research. Currently planned neutron diagnostic systems for ITER include neutron activation systems [4, 5], fission chambers [4, 6], plastic scintillators [4, 7, 8].

In addition to the previously mentioned diagnostics, neutron spectrometers are planned for ITER. These will use Stilbene detector [9], NE213 compact spectrometer [10] or sCVD diamond detectors [11–14]. Using these, the energy and flux of neutrons can be resolved in time, enabling a better understanding of the dynamics inside the Tokamak reactor.

Of the three candidates studied, one (sCVD) is already envisaged as part of future nuclear fusion projects such as ITER, but SiC detectors are also being studied as part of future fusion reactors. [15, 16]. In contrast, hardly any research on direct neutron measurements for Si detectors can be found, although they have been an integral part of various physics experiments for a long time. But all this research and active use of solid-state detectors shows the great interest and potential of them to be a reliable part of future neutron diagnostics to obtain a multitude of plasma parameters. They will be a key part to any currently built or planned nuclear fusion device and will enable time resolved measurements of the neutron flux and energy. The parameters obtained from these two raw parameters can be used to understand and control the plasma, which is of utmost importance for stable operation and for the safety of the reactor. The importance of neutron diagnostics is underlined by the aim of DEMO, the successor to ITER, which will generate electricity for the first time [17], to reduce the total number of diagnostics but still have a multitude of neutron diagnostics [18].

1.2 Detectors working principle

This section introduces the basic working principle of solid-state detectors. This should provide the prerequisites for understanding the following chapters.

The two main components of a detector are the PCB material and the sensor. The sensor consists of the bulk material and the electrodes to read-out the particle signals and provide a bias voltage if needed. The electrodes of the investigated detectors were identical, with different layers of gold, titanium and platinum. The working principle, meaning how a particle is detected, is the same for all of them and depends on the type of particle.

Die approbierte gedruckte Originalversion dieser Diplomarbeit ist an der TU Wien Bibliothek verfügbar
The approved original version of this thesis is available in print at TU Wien Bibliothek.
TU Bibliothek Your knowledge hub WIEN

To detect a particle, the particle needs to interact with the bulk material and a current needs to be created. This is done by ionising the atoms of the bulk material, either by continuous ionisation along the particle path through the detector or at one point, both visualised in figure 1.1.

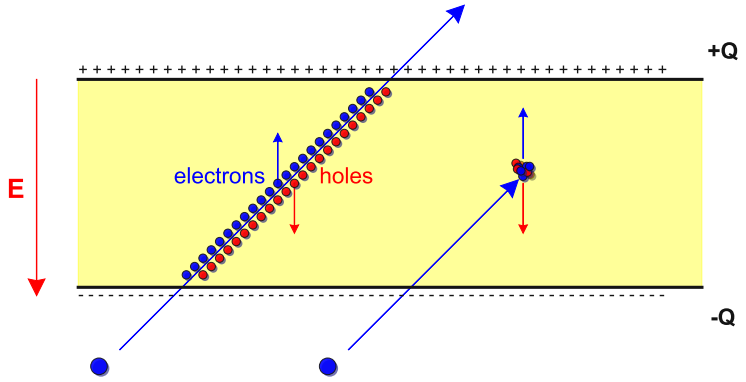

Figure 1.1: The ionisation process of a traversing particle inside a solid-state detector. On the left a continuous ionisation, on the right a point-like ionisation.

For both mechanism, some kinetic energy of the incoming particle is transferred to the electrons of the bulk material atoms. Charged particles interact via electromagnetic elastic scattering. Uncharged particles on the other hand interact via different mechanism which need to produce a charged particle, which ionises the bulk material. Through the ionisation process, a positively charged hole (h^+) is created at the location of the ionised atom and an electron is emitted. This e^-/h^+ pair (visualised as blue and red dots) recombines instantaneously if no electric field is present, resulting in no measurable current signal [19]. But if the sensor is biased (visualised as "+" and "-" at the electrodes), the electric field pulls the e^-/h^+ pair apart to one of the electrodes (visualised as arrows).

The movement of these charges leads to a voltage drop at the electrodes and a current, described by the Shockley–Ramo theorem [20], which can be amplified and measured. The measured current is therefore a product of the hole and electron movement, which can be seen very clearly in sCVD detector signal in [21]. In total, the charge Q can be measured, which is determined by the ionisation energy of the bulk material and the deposited energy of the incoming particle.

For multiple particle interactions, either a Gaussian or Landau distribution [22] will emerge from the data. First if the incoming particle is stopped in the sensor and latter when the particle is traversing the sensor, depositing only part of its ki-

Die approbierte gedruckte Originalversion dieser Diplomarbeit ist an der TU Wien Bibliothek verfügbar
The approved original version of this thesis is available in print at TU Wien Bibliothek.

netic energy. For the presented detector investigation, the interaction mechanisms for neutrons and gammas are of interest, which are discussed in greater detail in the following.

1.2.1 Neutron interaction with a solid-state detector

Neutrons do not carry an electrical charge, therefore there is no interaction and subsequent ionisation via the electromagnetic force in the sensor. Nevertheless, they can be detected because neutrons can interact with the nuclei of the bulk material atoms either via elastic or inelastic scattering. The former is always present while the latter requires a neutron energy above a reaction specific threshold E_{th}. Both mechanism are point-like ionisation processes.

Elastic neutron scattering

Elastic scattering is always present, as it has no E_{th}. It follows the classical collision principle, because the neutron is scattered from the nucleus like a billiard ball. Therefore, the transferred energy only depends on energy and momentum conservation. The process is visualised in Figure 1.2.

Elastic neutron scattering results in a scattered neutron and a recoil nucleus, which ionises the surrounding material. The kinetic energy of the recoil nucleus corresponds to the lost kinetic energy of the neutron (E_k), which depends on the angle β of the recoil nucleus to the incoming neutron. The formula for the transferred energy is

$$E_k = \frac{4Mm_n}{(M+m_n)^2}\cos^2\beta \tag{1.1}$$

The maximum energy transfer occurs during a head-on collision between the neutron and the nucleus at $\beta = 0°$, resulting in $\cos^2\beta = 1$. The maximum transferred energy then depends solely on the mass of the interacting nucleus. The maximum energy transfer ($E_{k,max}$) for ^{12}C is a fraction of 28.6 % and 13.3 % for ^{28}Si of the incoming neutron energy. Therefore a maximum elastic energy cut-off exists in any measured neutron spectrum, depending on the incoming neutron energy.

In contrast to elastic scattering in classical physics, the probability of a certain angle depends on the neutron energy and the differential cross section $\frac{d\sigma}{d\Omega}$ for the bulk material atoms. This results in a characteristic shape of the neutron response function of a material, which is the distribution of deposited neutron energies due to $\frac{d\sigma}{d\Omega}$.

Die approbierte gedruckte Originalversion dieser Diplomarbeit ist an der TU Wien Bibliothek verfügbar
The approved original version of this thesis is available in print at TU Wien Bibliothek.
TU Bibliothek Your knowledge hub WIEN

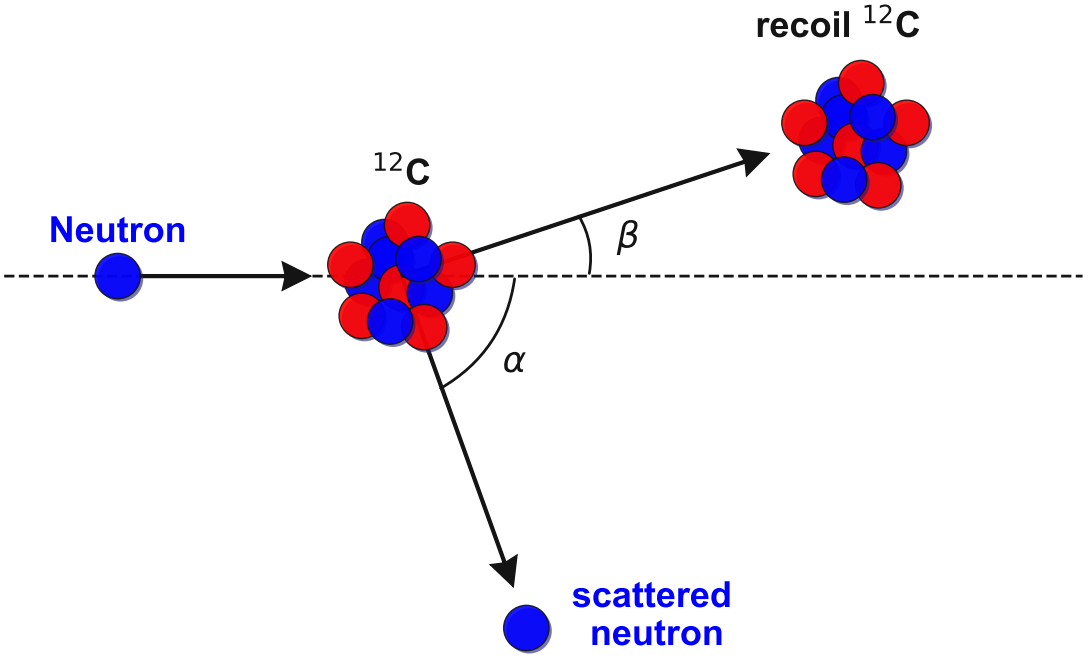

Figure 1.2: Schematics of neutron elastic scattering on ^{12}C.

Inelastic nuclear reactions

An inelastic nuclear reactions causes the neutron to be absorbed by the nucleus and thus causes the nucleus to become metastable due to the additional kinetic energy. The nucleus subsequently relaxes to a stable state via the release of gamma radiation or splitting up into reaction products. It is visualised in figure 1.3 for the ^{12}C(n,α)^{9}Be process.

For an inelastic nuclear process to happen, the neutron energy E_n must exceed the process specific threshold energy E_{th}. If this is the case, the inelastic process is called an open channel. The open channels therefore depend on the neutron energy and also on the interacting nucleus. Each channel has a E_{th} and a Q-value. The Q-value determines whether the interaction is endothermic or exothermic. An endothermic interaction results in a negative Q-value, indicating that kinetic energy is lost during the split-up. Conversely, an exothermic interaction results in a positive Q-value, indicating that kinetic energy is gained during the split-up. The reaction products subsequently ionise the surrounding sensor material, generating a measurable signal. The resulting measured energy from the detector is

$$E_{inelastic} = E_n + Q \tag{1.2}$$

Die approbierte gedruckte Originalversion dieser Diplomarbeit ist an der TU Wien Bibliothek verfügbar
The approved original version of this thesis is available in print at TU Wien Bibliothek.

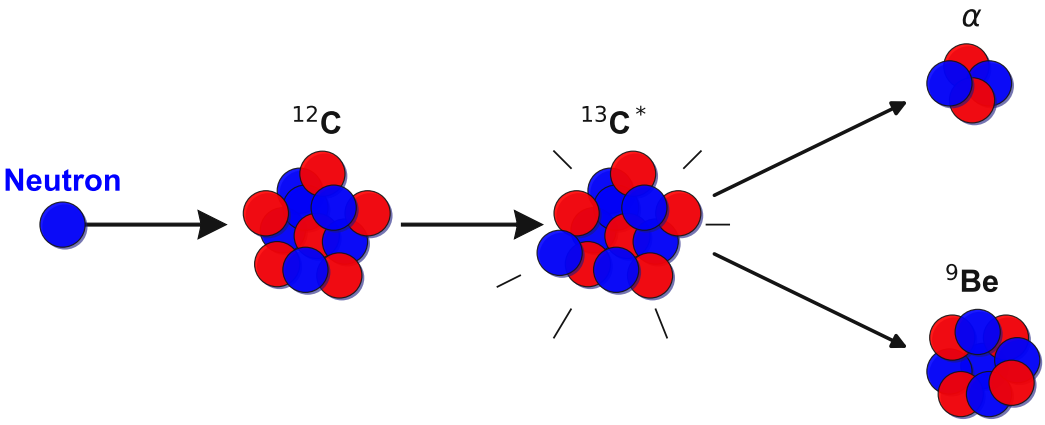

Figure 1.3: Schematics of the ^{12}C(n,α)^{9}Be reaction.

As for elastic neutron scattering, the neutron response function depends on the neuron energy and the cross-section for all available inelastic processes. Table 1.1 lists all inelastic nuclear processes for ^{12}C with their respective E_{th} and Q-value. Table 1.2 lists all inelastic nuclear processes for ^{28}Si with their respective E_{th} and Q-value [23, 24]. Both tables summarise the inelastic processes for neutron energies $E_n < 14.1\,\text{MeV}$.

Nuclear reaction	Q [MeV]	E_{th} [MeV]
^{12}C(n,γ)^{13}C	4.946	0
^{12}C(n,α)^{9}Be	-5.702	6.181
^{12}C(n,3α)	-7.274	7.886
^{12}C(n,n+α)^{8}Be	-7.366	7.986
^{12}C(n,2α)^{5}He	-8.010	8.684
^{12}C(n,p)^{12}B	-12.587	13.646
^{13}C(n,α)^{10}	-3.836	4.133

Table 1.1: Neutron-induced inelastic nuclear process channels for ^{12}C, with their respective threshold energies and Q-values [23, 24].

Die approbierte gedruckte Originalversion dieser Diplomarbeit ist an der TU Wien Bibliothek verfügbar
The approved original version of this thesis is available in print at TU Wien Bibliothek.

Nuclear reaction	Q [MeV]	E_{th} [MeV]
^{28}Si(n,γ)^{29}Si	8.474	0
^{28}Si(n,α)^{25}Mg	-2.654	2.750
^{28}Si(n,p)^{28}Al	-3.860	4.000
^{28}Si(n,d)^{27}Al	-9.360	9.698
^{28}Si(n,n+α)^{24}Mg	-9.984	10.344
^{28}Si(n,n+p)^{27}Al	-11.585	12.003
^{28}Si(n,^{3}He)^{26}Mg	-12.138	12.576
^{28}Si(n,2α)^{21}Ne	-12.540	12.992
^{28}Si(n,2p)^{27}Mg	-13.413	13.897

Table 1.2: Neutron-induced inelastic nuclear process channels for ^{28}Si, with their respective threshold energies and Q-values [23, 24].

The investigated neutron energies

The investigated neutron energies do not exceed E_{th} for the inelastic reactions of ^{12}C. The inelastic nuclear reaction ^{28}Si(n,α)^{25}Mg is open, but its cross section is three orders of magnitude smaller than the elastic cross section for all neutron energies investigated. Therefore, only elastic scattering needs to be taken into account, which has a highest possible energy transfer. The shape of the neutron response function depends on the differential cross-section, while the interaction probability depends on the total cross-section. Figure 1.4 shows the total cross-section for ^{12}C and ^{28}Si in the neutron energy range from 2.2 MeV to 4.2 MeV, covering the neutron energies for the presented investigation [25].

The cross-sections have the same order of magnitude at the investigated neutron energies. Therefore, neither is favoured over the other with respect to the neutron interaction probability. However, there is a clear distinction in the shape of the cross-section. ^{28}Si has resonances at numerous neutron energies, while ^{12}C has a lower number of such resonances. This makes the ^{28}Si neutron interaction probability more sensitive to the precise neutron energy.

Die approbierte gedruckte Originalversion dieser Diplomarbeit ist an der TU Wien Bibliothek verfügbar
The approved original version of this thesis is available in print at TU Wien Bibliothek.

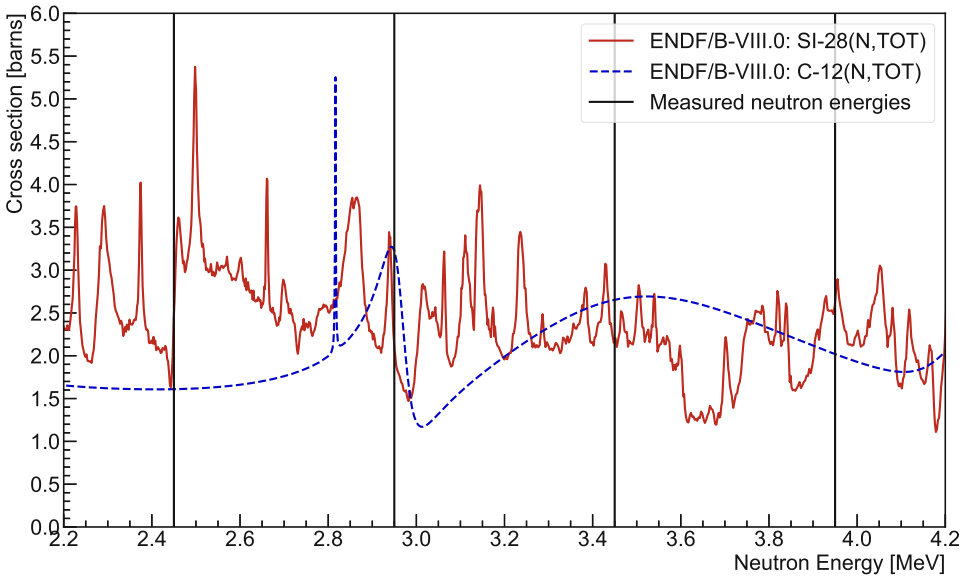

Figure 1.4: The total neutron cross-section for ^{12}C (blue dashed line) and ^{28}Si (red line). Black vertical lines indicate the investigated neutron energies.

1.2.2 Gamma interaction with a solid-state detector

Similar to neutrons, photons have no electric charge and therefore do not generate an electric signal in the detector. The photon must interact with the electrons in the shell of an atom in the sensor or surrounding material to transfer some of its initial energy to the electron. Supposing the transferred energy is greater than the binding energy of the atom, the secondary electron can traverse through the detector material and create e^-/h^+ pairs as described previously. Three main mechanisms for the transfer of energy from a photon to an electron are [26]:

1. **Photoelectric effect:** The photon is absorbed by an electron, transferring its energy to the electron and ejecting it from its atom. This effect is dominant at lower X-ray energies [27].

2. **Compton scattering:** The photon scatters off an electron, transferring part of its energy and momentum to the electron. This scattering process is significant in gamma-ray interactions, especially in medium to high-energy regimes [28].

3. **Pair production:** At high energies, a gamma-ray photon can transform into an electron-positron pair near a nucleus. This mechanism is only possible at

Die approbierte gedruckte Originalversion dieser Diplomarbeit ist an der TU Wien Bibliothek verfügbar
The approved original version of this thesis is available in print at TU Wien Bibliothek.

a photon energy above two times the electron rest mass of 511 keV [29].

Figure 1.5 visualises the three photon interaction mechanism.

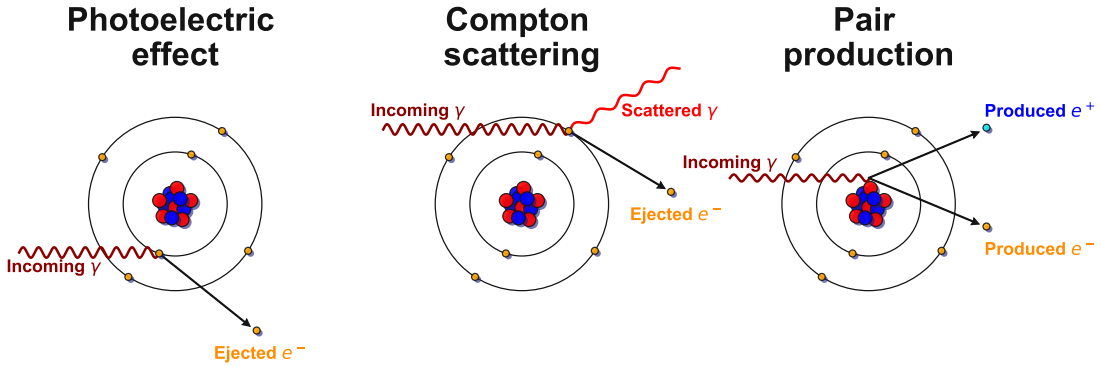

Figure 1.5: Visualisation of the photoelectric effect, Compton scattering and pair production for photons.

All three mechanisms produce a secondary electron in the sensor material, which continuously ionises surrounding atoms along its path, generating a signal. If the kinetic energy of the secondary electron is sufficient, it will pass through the sensor, leaving it and depositing only a fraction of its kinetic energy, which is usually only a fraction of the initial photon energy.

Figure 1.6 shows the cross-section for photon interactions with ^{12}C for each of the three interaction mechanisms and the resulting total cross-section. Figure 1.7 shows the cross-section composition for ^{28}Si. The two cross-sections were collected by using the software XCOM from NIST [30].

The cross-section for ^{12}C and ^{28}Si show the same photon energy dependency for the three interaction mechanisms, with the photoelectric absorption dominating at low energies up to around 30 keV for ^{12}C and 60 keV for ^{28}Si. At higher energies Compton scattering dominates up to a photon energy of 30 MeV for ^{12}C and 15 MeV for ^{28}Si, at which point pair production starts to dominate the photon cross-section.

The expected photon energies for neutron experiments are in the photon energy range dominated by Compton scattering. As a γ-background is unavoidable in any neutron experiments it impacts the measured detector response function. Therefore a low interaction probability with gammas is preferable. Figure 1.8 compares the total photon cross-section for ^{12}C and ^{28}Si.

Die approbierte gedruckte Originalversion dieser Diplomarbeit ist an der TU Wien Bibliothek verfügbar
The approved original version of this thesis is available in print at TU Wien Bibliothek.

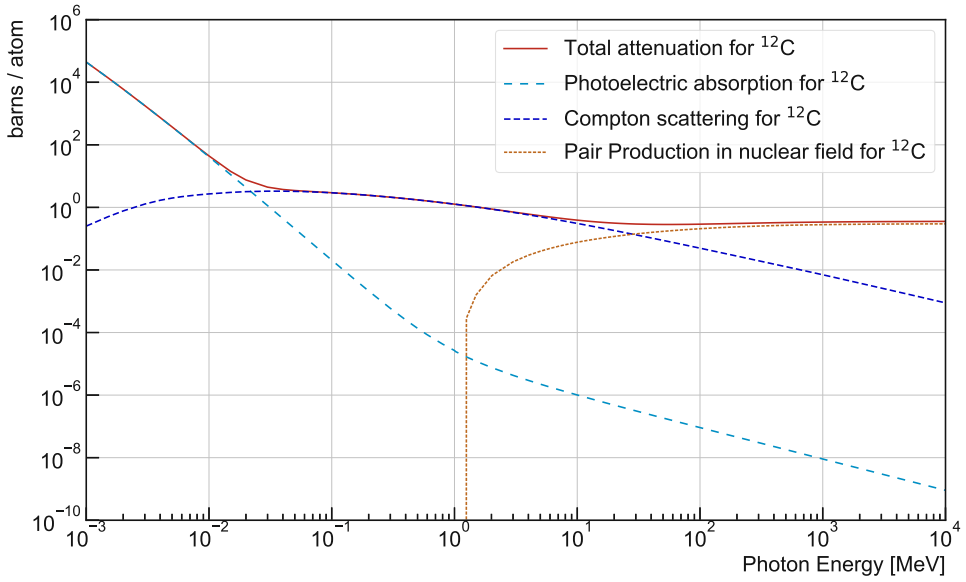

Figure 1.6: The cross-section for the different photon interaction mechanisms and their sum for ^{12}C as function of the photon energy in MeV.

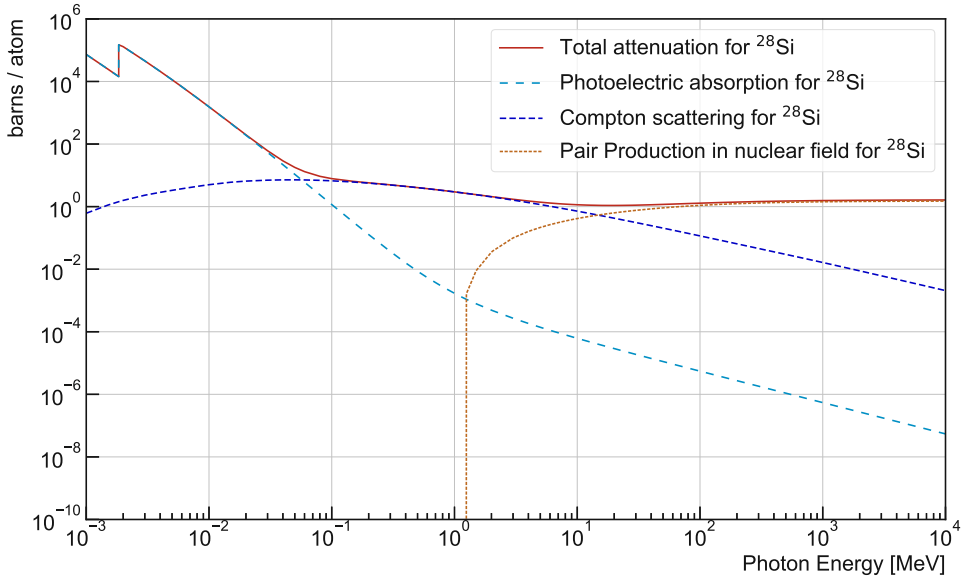

Figure 1.7: The cross-section for the different photon interaction mechanisms and their sum for ^{28}Si as function of the photon energy in MeV.

Die approbierte gedruckte Originalversion dieser Diplomarbeit ist an der TU Wien Bibliothek verfügbar
The approved original version of this thesis is available in print at TU Wien Bibliothek.

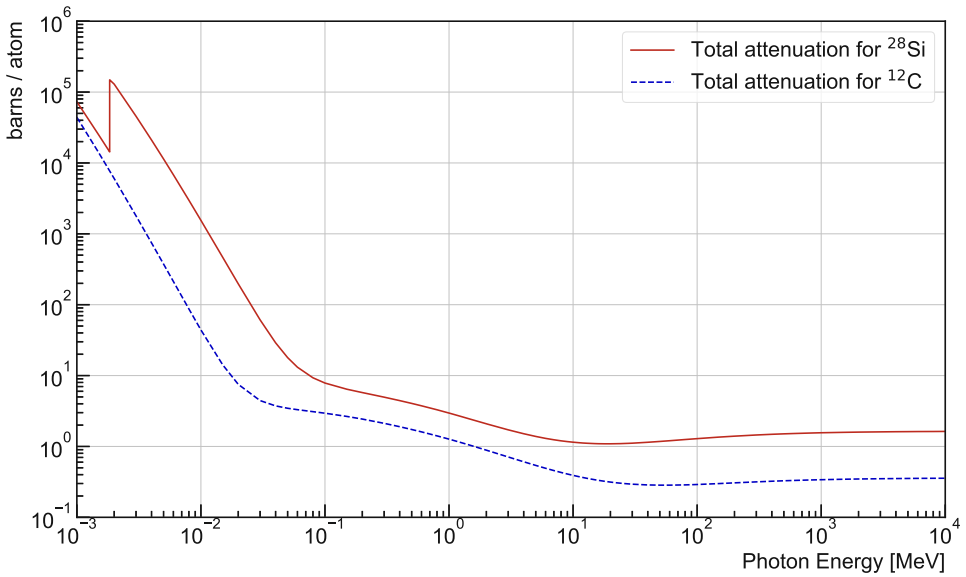

Figure 1.8: Comparison of the total photon cross-section for ^{12}C and ^{28}Si as function of the photon energy in MeV.

It is evident that the cross-section for ^{28}Si is higher than for ^{12}C at all photon energies. The exact factor between the cross-section for ^{28}Si (σ_{Si}) and the cross-section for ^{12}C (σ_C) is shown in figure 1.9.

The cross-section for silicon is at least a factor two higher than for carbon, favouring a sCVD detector over a Si detector in regards to γ-background rejection in theory. The factor between the cross-sections is relatively constant at photon energies from 0.1 MeV up to 3 MeV. As a SiC detector is composed of ^{12}C and ^{28}Si, the resulting photon cross-section is a mixture of both elements.

A sufficient γ-background rejection is essential for an accurate neutron response function measurement. Furthermore does the thickness of the sensor increase the probability of an interaction, making the exact thickness of the sensor material an important parameter for any future neutron diagnostics, as depending on the thickness of the sensor and its material, γ background can mask the neutron counts altogether, making a measurement impossible.

Die approbierte gedruckte Originalversion dieser Diplomarbeit ist an der TU Wien Bibliothek verfügbar
The approved original version of this thesis is available in print at TU Wien Bibliothek.

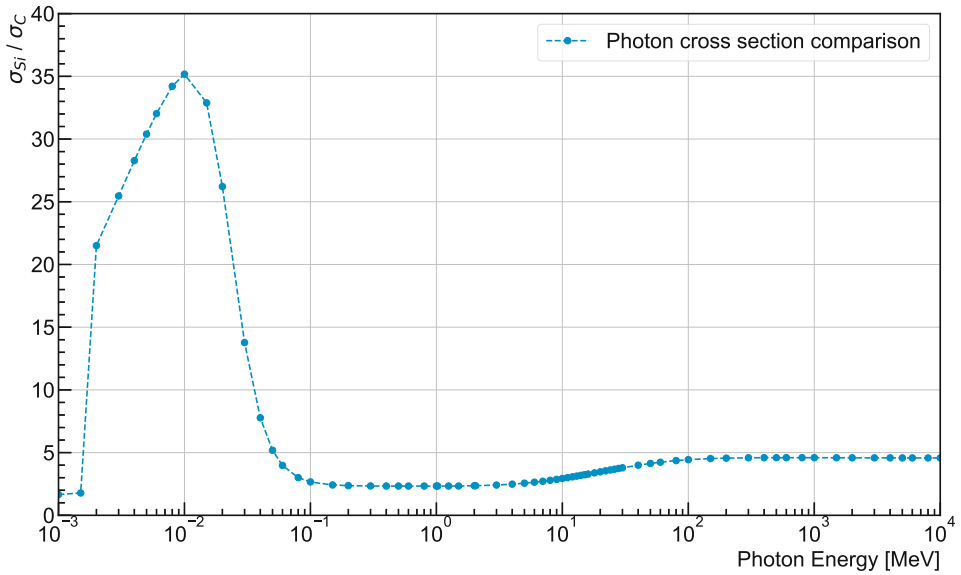

Figure 1.9: The factor between the cross-section for ^{28}Si compared to ^{12}C as function of the photon energy in MeV.

1.3 Detector comparison

To compare the three detector contestants, it is necessary to understand the differences in their characteristics. This includes some standard properties like the ionisation energy, but also the neutron and photon cross-section discussed in the previous section. Some additional sensor material characteristics are also relevant for the determination of the most suitable detector in future large scale nuclear fusion reactors, like the thermal conductivity.

Table 1.3 compares some characteristics of the three sensor materials. The most relevant value for measuring neutrons is the ionisation energy, the energy required to create an electron-hole pair, and the band gap, the energy required to excite an electron from the conduction band to the valence band.

The ionisation energy, i.e. the e^-/h^+ pair creation energy, determines the deposited charge and therefore the amplitude of the measured signal. The energy gap determines the sensitivity to photons, since the photon needs to have at least this energy to excite an electron and generate a signal. Various literature sources provide marginally different values, but the overall comparison for material properties is still applicable [33, 34].

Apart from the material characteristics, the intrinsic structure of the detectors

Die approbierte gedruckte Originalversion dieser Diplomarbeit ist an der TU Wien Bibliothek verfügbar
The approved original version of this thesis is available in print at TU Wien Bibliothek.

Property	Si	SiC	Diamond
Atomic Number (Z)	14	14/6	6
Density (g/cm^3)	2.33	3.21	3.51
Energy Gap (eV)	1.12	3.23	5.5
e^-/h^+ Pair Creation Energy (eV)	3.6	7.6	13
Displacement Energy (eV)	25	30	43
Electron Mobility (cm^2/Vs)	1450	800	1714
Hole Mobility (cm^2/Vs)	450	115	2064
Saturated Electron Drift Velocity (cm/s)	0.8 x 10^7	2 x 10^7	2.2 x 10^7
Thermal Conductivity (W/Kcm)	1.5	4.9	24-25

Table 1.3: Comparison of Material Properties: Silicon, SiC, and sCVD [31, 32].

is slightly different. All three detector contestants were biased from one sensor side and read-out via the opposite electrode. The sCVD sensor consists of a uniform crystal which works like a capacity, whereas the Si and SiC detector are doped to create a p/n junction, like a PIN diode. The bias voltage creates a reversed p/n junction, resulting in a depletion zone inside the detector, which can be utilised for measuring particles. Therefore, a correct bias voltage is essential to obtain the best possible detector response function [34]. The sensor is then either glued and bonded to a PCB structure or has a dedicated way of making proper electrical contact with the PCB. From the PCB, the read-out and bias voltage lines are then connected to the voltage supply and an external amplifier.

1.4 Readout electronics

The particle detector signal needs to be amplified and converted to a voltage in order to be measured and analysed. This happens in the amplifier, which is con-

Die approbierte gedruckte Originalversion dieser Diplomarbeit ist an der TU Wien Bibliothek verfügbar
The approved original version of this thesis is available in print at TU Wien Bibliothek.

nected to the detector at its input and to a digitizer at its output. The presented measurements used a CIVIDEC Cx-L Spectroscopic Amplifier [3], a charge amplifier with a secondary shaping stage, generating a Gaussian-like output pulse. The amplifier is inverting resulting in a positive output signal for an incoming negative charge and vice-versa. It is tailored for precise spectroscopic measurements with its output pulse height h, in mV, proportional to the collected input charge Q, in fC, or equivalently to the number of electrons n_e. The deposited energy in MeV from the pulse height is calculated by using the gain of the amplifier A, in mV/fC, and the ionisation energy of the detector E_{ion} in eV, following equations (1.3) - (1.5).

$$Q = \frac{h}{A} \tag{1.3}$$

$$n_e = \frac{Q}{e} \tag{1.4}$$

$$E_{dep} = \frac{n_e \cdot E_{ion}}{10^6} \tag{1.5}$$

The amplifier was developed to be as versatile as possible, meaning it was made bipolar, enabling measurements of positive and negative charges. Additionally the full width at half maximum (FWHM) of the output pulse was changed from 180 ns to 1.2 µs. This lowers the intrinsic noise and increases the accuracy with the trade-off of decreasing double-pulse resolution. An exemplary averaged output pulse, showing the response to a deposited energy of 5.5 MeV in diamond is shown in figure 1.10.

The pulse has a FWHM of 1.2 µs, a peaking time (from 10 % to the peak) of 830 ns, a rise time (from 10 % to 90 %) of 579 ns and a fall time (from 90 % to 10 %) of 1.25 µs. These characteristics are independent from the input charge and the amplitude, respectively. To ensure a constant conversion factor from the pulse amplitude to the energy deposited in the detector, the linearity of the amplifier was measured. For this purpose, a calibrated capacitor of 0.71 pF as capacity C was used in combination with a variable input voltage V, resulting in an input charge according to equation (1.6).

$$Q = C \cdot V \tag{1.6}$$

For each input charge, the amplitude of 100 consecutive pulses is recorded, averaged and stored with the input charge for offline analysis. The result of the linearity measurement is shown in figure 1.11.

Die approbierte gedruckte Originalversion dieser Diplomarbeit ist an der TU Wien Bibliothek verfügbar
The approved original version of this thesis is available in print at TU Wien Bibliothek.
TU Bibliothek Your knowledge hub WIEN

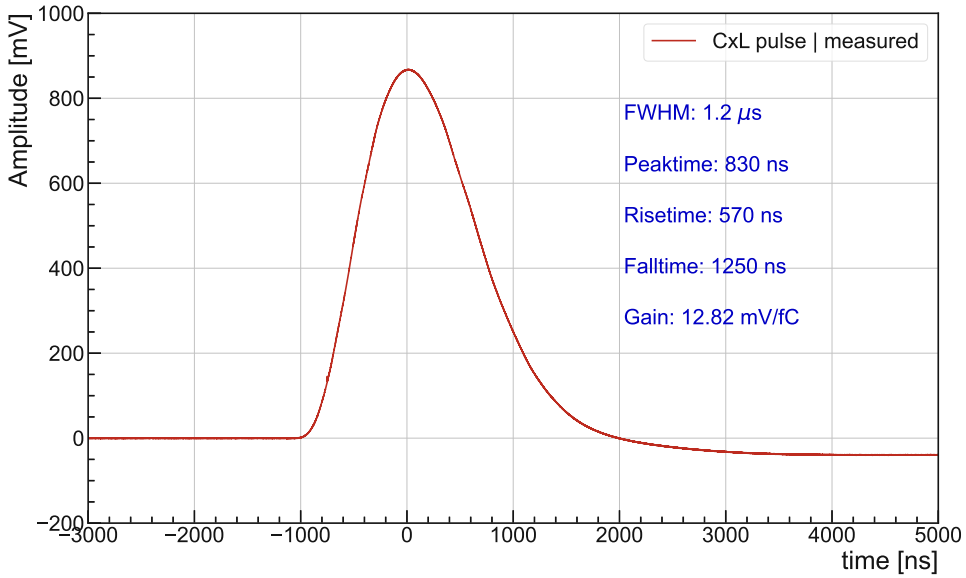

Figure 1.10: The CxL amplifier response to an input charge of 67.7 fC, corresponding to an energy deposition of 5.5 MeV in diamond.

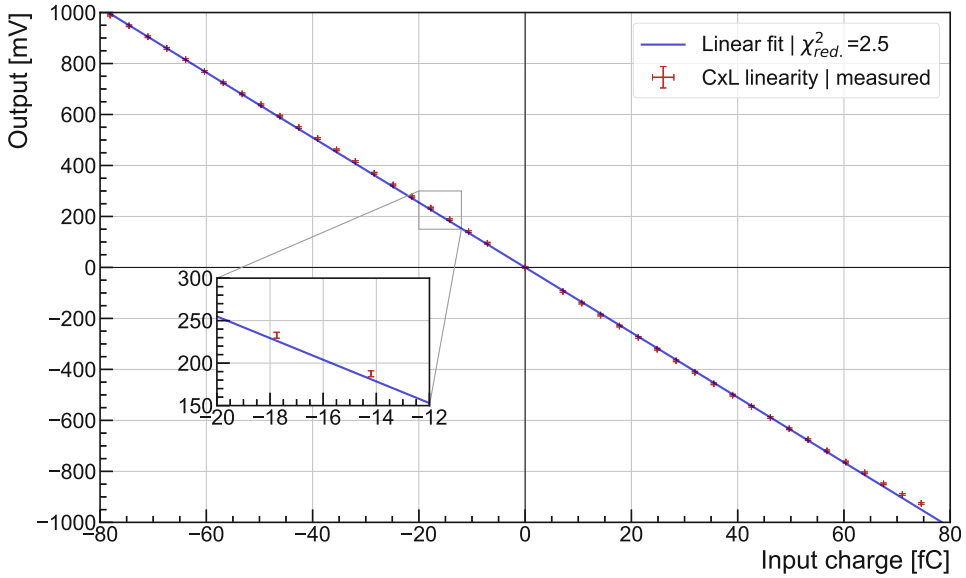

Figure 1.11: The linearity of the CxL amplifier is shown in red and a linear fit is shown in blue with $\chi^2_{red.}$=2.5.

Die approbierte gedruckte Originalversion dieser Diplomarbeit ist an der TU Wien Bibliothek verfügbar
The approved original version of this thesis is available in print at TU Wien Bibliothek.

The linear range of the CxL amplifier is ±1 V with a gain of 12.82 mV/fC. For each input charge, the standard deviation of the output pulses was 3.5 mV, above the nominal amplifier noise due to the setup. As the CxL amplifier is sensitive to its capacitive input load, the linearity measurement was conducted with various input capacitance. The procedure remained unchanged with the addition of a parallel capacitor between the calibrated 0.71 pF capacitor and the input of the CxL amplifier. The result of these measurements is shown in figure 1.12.

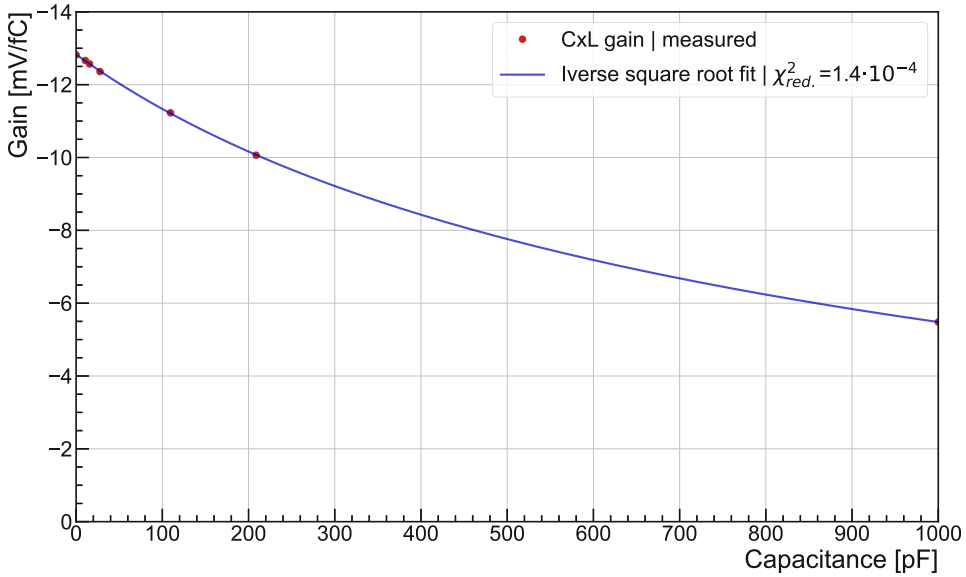

Figure 1.12: The measured gain of the CxL amplifier as function of the input capacitance is shown in red and an inverse square root fit is shown in blue with $\chi^2_{red.}$=1.4×10^{-4}.

The gain of the CxL amplifier decreases as the input capacitance increases, following the fit denoted by the formula (1.7).

$$A = \frac{-22.45}{\sqrt{3.14 \cdot 10^{-3} \times pF + 1.62}} + 4.80 \tag{1.7}$$

The validity of the fit is limited to this particular amplifier. However, it demonstrates the gain behaviour with different capacitive loads at the input for CxL amplifiers built with the same parameters. This is of importance in experiments because the detector has an intrinsic capacitance and the detector cable between the detector and the amplifier has a capacitance of about 100 pF m^{-1}.

Die approbierte gedruckte Originalversion dieser Diplomarbeit ist an der TU Wien Bibliothek verfügbar
The approved original version of this thesis is available in print at TU Wien Bibliothek.

An amplifier has always an intrinsic noise, which is also affected by the attached capacitive load at the input in case of a charge sensitive amplifier. To determine the CxL noise performance, the signal of the CxL was recorded with different capacitive loads attached to its input. The standard deviation of the recorded signal was then measured. The average noise in mV over the input capacitance is shown in figure 1.13.

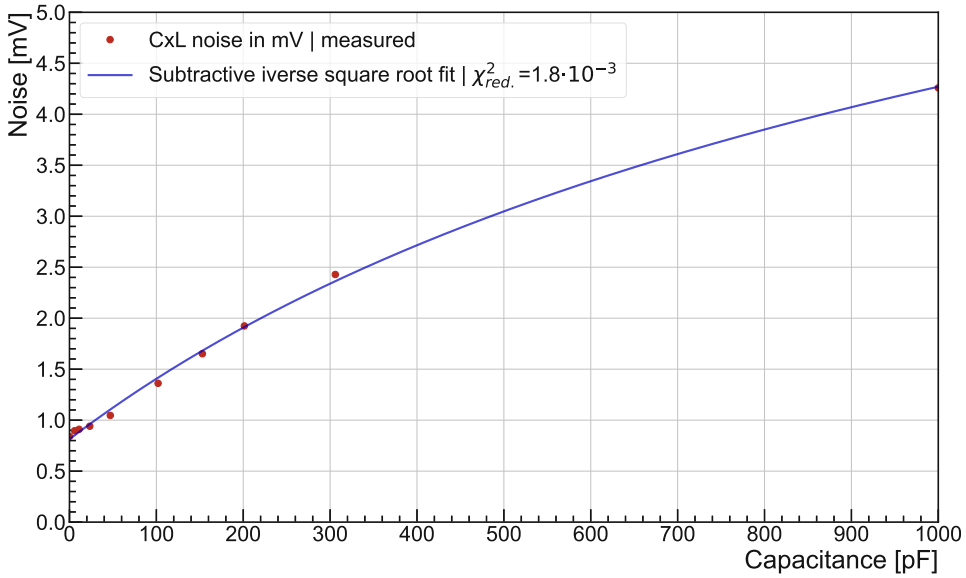

Figure 1.13: The noise of the CxL amplifier as function of the input capacity is shown in red and a subtractive inverse square root fit is shown in blue with $\chi^2_{red.}$=1.8×10^{-3}.

The fit of the noise in mV is denoted in formula (1.8).

$$Noise \;=\; 11.26 - \frac{2.41}{\sqrt{6.67 \cdot 10^{-5} \times pF + 0.05}} \tag{1.8}$$

The noise measurement in mV is then converted to an equivalent noise charge, using the fit of the noise and the fit of the gain A with equation (1.3). This is then converted to an equivalent number of electrons, using equation (1.4), resulting in a linear fitted electron noise of $(385 + 4/pF)$ electrons. Using this fit and the ionisation energy of the different detectors (E_{ion}), the energy equivalent noise can be calculated, shown in figure 1.14.

The energy equivalent noise is increasing linearly with increasing input capacitance. The variation between the detectors is caused by their different ionisation

Die approbierte gedruckte Originalversion dieser Diplomarbeit ist an der TU Wien Bibliothek verfügbar
The approved original version of this thesis is available in print at TU Wien Bibliothek.

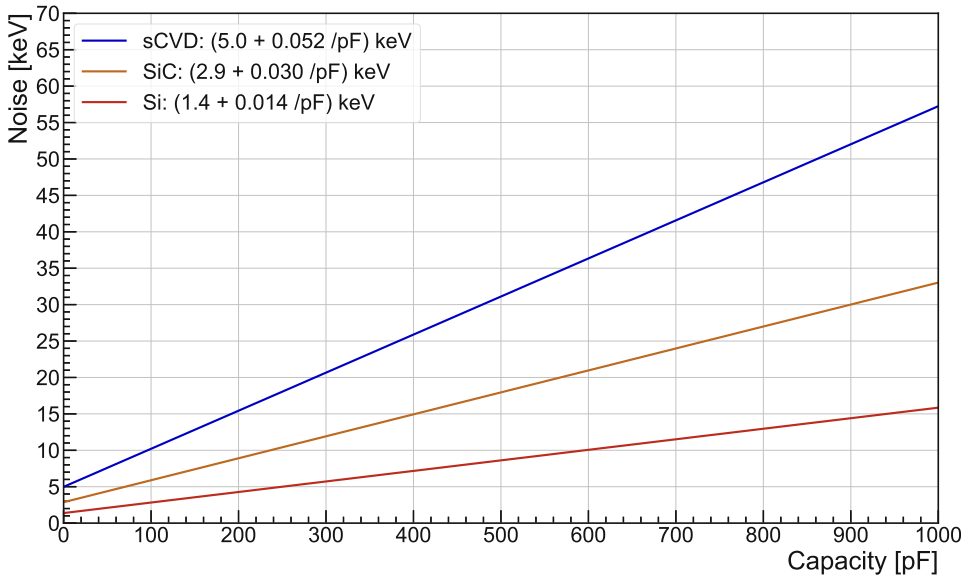

Figure 1.14: The noise of the CxL amplifier converted to energy using the noise and gain measurements in combination with the ionisation energy for each detector.

energies. This corresponds to the best possible energy resolution from the amplifier, assuming no additional noise sources or disturbances.

1.5 Digitizer development

The measurements in this work provide first results from a newly developed data acquisition system. This was developed to enhance the vertical resolution from the existing CIVIDEC ROSY® AX106 Real-Time Data Acquisition and Processing System [35] to the new CIVIDEC ROSY® Neutron Spectroscopy System. The new system has 14-bit vertical resolution at a sampling rate of up to 62.5 MS/s. It was developed to use CxL Spectroscopic Amplifiers for precise neutron spectroscopy applications and is using a standalone USB digitizer for converting the analog amplifier signal to a digital value, which is analysed on a separate small form factor Linux single board computer. The following section gives an introduction to the backend data processing of the system and the visualisation of it in a front-end web-based graphical user interface (GUI).

Die approbierte gedruckte Originalversion dieser Diplomarbeit ist an der TU Wien Bibliothek verfügbar
The approved original version of this thesis is available in print at TU Wien Bibliothek.

Backend data processing

To be as flexible as possible for future developments, the live data analysis is implemented in Python. On one hand, this provides a lot of freedom and ease of use, but on the other hand, Python's lack of speed had to be overcome. To use multicore processing, sharing data between the cores was of utmost importance. To do so, the class SharedMemory from the multiprocessing.shared_memory module was used [36]. To fill these shared memory segments, a ndarray from the numpy library was used [37]. An example of the shared memory array for a 13-bit histogram is shown in the following:

```
1 import numpy as np
2 from multiprocessing import shared_memory
3
4 Channel_A_Hist_shm = shared_memory.SharedMemory(create = True,
5                                                 size = np.int64().itemsize * 8192)
6 Channel_A_Hist = np.ndarray(shape = (8192,),
7                              dtype = np.int64,
8                              buffer = Channel_A_Hist_shm.buf)
```

Sharing the "Channel_A_Hist_shm" variable to different CPU cores allows for accessing the same data array from different processor cores. An additional benefit is the added speed of calculations using numpy arrays over standard Python lists. This allows for a first major performance boost, but still not enough for 62.5×10^6 16-bit data points per second. Using a CxL amplifier means the amplitude of each peak has to be detected and filled into a histogram. Furthermore, to calculate a count rate, it is necessary to determine the precise timestamp of each pulse. This requires iterating over each data point. New data is sent from the digitiser to the Python code in data packets, representing 8.3 ms of data on average. Therefore, there is a strict upper limit for the processing time of the data contained therein, which must be less than the time to which the data correspond. Otherwise the live data analysis is not possible and data queues up for processing. The setup is designed to never lose any data, so the worst case scenario is queuing up of data.

To ensure speed for data processing, a compiled programming language (such as C or C++) was needed rather than an interpreted language (such as Python). As it was important to avoid compromising flexibility by combining Python and C, the Python package NUMBA [38] was used to pre-compile Python functions into faster C-like functions. In one-to-one comparisons with similar C++ functions, the

Die approbierte gedruckte Originalversion dieser Diplomarbeit ist an der TU Wien Bibliothek verfügbar
The approved original version of this thesis is available in print at TU Wien Bibliothek.

compiled NUMBA functions were superior in speed, when called from a Python project. The most basic peak search and analysing algorithm implementation needs the new input data, a trigger level, the peak window and the previous histogram array and count rate array. As output, the NUMBA function returns the updated histogram and count rate. The interpolated timestamp at 50 % of the peak amplitude is used for the most accurate time measurements as the effect of noise is minimal. A simplistic but performant implementation is shown in the following:

```
#@cc.export('DATA_processing', '(i2[:], i2, i2, i2, i8[:], i4[:], i8)')
def DATA_processing(DATA, Trigger, pre_window, Window, HIST, RATE, RATE_RES):
    pos = pre_window    # Start position at least pre_window
    data_length = len(DATA)    # Length of the data
    length_peak = Window + pre_window    # Total peak window for searching the peak

    # If Trigegr is negative the Data is inverted
    if Trigger < 0:
        DATA = -DATA
        Trigger = -Trigger

    # Until which data point hte search should continue
    max_length = data_length - 2*Window

    while pos < max_length:
        # Trigger level has been exceeded
        if DATA[pos] > Trigger:
            # Get the peak amplitude -> Initial the trigger value
            Peak_amplitude = DATA[pos]
            # Position of the trigger
            peak_pos = pos

            # Looking for the maximum value in the peak window
            for i in range(1, Window):
                data_value = DATA[pos + i]
                if data_value > Peak_amplitude:
                    Peak_amplitude = data_value
                    peak_pos = pos + i
```


Die approbierte gedruckte Originalversion dieser Diplomarbeit ist an der TU Wien Bibliothek verfügbar
The approved original version of this thesis is available in print at TU Wien Bibliothek.
TU Bibliothek Your knowledge hub WIEN

```
29
30              # Calculating 50 % of the detected peak
31              Half_Amplitude = Peak_amplitude / 2
32
33              # Now find the exact time of 50% Amplitude
34              look_for_Half_Amplitude = True
35
36              # Go back from the peak
37              deducted_points = 0
38
39              while look_for_Half_Amplitude:
40                  if DATA[peak_pos - deducted_points] <= Half_Amplitude:
41
42                      # First datapoint above the half peak amplitude
43                      above_Half_Amplitude = peak_pos - deducted_points + 1
44
45                      # Last datapoint below the half peak amplitude
46                      below_Half_Amplitude = peak_pos - deducted_points
47
48                      # Stop looking for the timestamp
49                      look_for_Half_Amplitude = False
50
51                      # Calculating the vertical difference between the two datapoints
52                      DIFF = (DATA[above_Half_Amplitude]) - (DATA[below_Half_Amplitude])
53
54                  deducted_points += 1
55
56              # Calculate the precise peaking time
57              Peak_Time = ((Half_Amplitude - (DATA[below_Half_Amplitude]))/DIFF)
58              Peak_Time = Peak_Time + below_Half_Amplitude
59
60              # Fill in the found peak amplitude into the histogram
61              HIST[Peak_amplitude // 4] += 1
62
63              # Increase the count rate
64              rate_pos = int(Peak_Time // RATE_RES)
```


Die approbierte gedruckte Originalversion dieser Diplomarbeit ist an der TU Wien Bibliothek verfügbar
The approved original version of this thesis is available in print at TU Wien Bibliothek.
TU Bibliothek Your knowledge hub WIEN

```
            RATE[rate_pos] += 1

            # Increase the position for looking for the peak
            pos += Window
        else:
            pos += 1

    # Not used data is returned
    reamining_DATA = DATA[-(data_length - pos):]

    return HIST, RATE, reamining_DATA
```

This function updates the histogram and count rate with the new data within the time that the data corresponds to. It can be used in the following manner:

```
HIST = np.zeros(int(2**13)).astype("i8")
COUNTRATE = np.zeros(10000).astype("i4")
RATE_RES = np.int64(100000)
TRIGGER = 5000
PRE_WINDOW = 10
WINDOW = 90

HIST, COUNTRATE, REMAIN = NORA_processing(DATA = NEW_DATA,
                                          Trigger = TRIGGER,
                                          pre_window = PRE_WINDOW,
                                          Window = WINDOW,
                                          HIST = HIST,
                                          RATE = COUNTRATE,
                                          RATE_RES = RATE_RES)
```

The use of multiprocessing in combination with pre-compiled NUMBA functions leads to a significant increase in performance, making Python suitable for continuous data acquisition and live data analysis of up to four simultaneous channels. Therefore, the Python data acquisition system was implemented and used for the following measurements.

Die approbierte gedruckte Originalversion dieser Diplomarbeit ist an der TU Wien Bibliothek verfügbar
The approved original version of this thesis is available in print at TU Wien Bibliothek.
TU Bibliothek Your knowledge hub WIEN

Frontend data visualisation

To control the newly developed data acquisition system, a graphical user interface GUI was needed. As simplicity and ease of use was the top priority, a web-based GUI was developed. Additionally, an API (application programming interface) was introduced to allow for control and data retrieving independent of the GUI. To decrease the development time, a pure python approach was taken by using the dash library [39]. This allowed to create a responsive interface with multiple graphs, updating with 10 Hz. In addition, a scope with different modes was implemented to help diagnosing any problems during a measurement campaign. The appearance of the GUI when opening the corresponding IP-address in a browser is shown in figure 1.15.

The presented approach enables a plug-and-play measurement, as the connection can be interrupted at any moment without interfering with the actual measurement. Multiple connections are also possible, which in combination with the web-based GUI, enables the use of the new system in a large network with multiple users looking after the measurement. Furthermore, updating the data acquisition system can be done by uploading a small data package to the system via the interface, enabling continuous development and support.

Data storage

A number of data formats for storing the recorded data were discussed, ultimately leading to the implementation of HDF5® [40]. It was chosen for its support for complex data structures with the added bonus of allowing metadata to be stored alongside. It was developed for research application and allows the storage of large datasets in comparatively small file sizes. Multiple open source software packages can be used to open the resulting files and visualising the incorporated data. A notable example is 'silx view' [41]. Additionally, almost any programming language can be used to open and manipulate the data format, for example the h5py package for python [42]. This allows all data for all active channels to be stored in a single file with all relevant metadata.

Die approbierte gedruckte Originalversion dieser Diplomarbeit ist an der TU Wien Bibliothek verfügbar
The approved original version of this thesis is available in print at TU Wien Bibliothek.

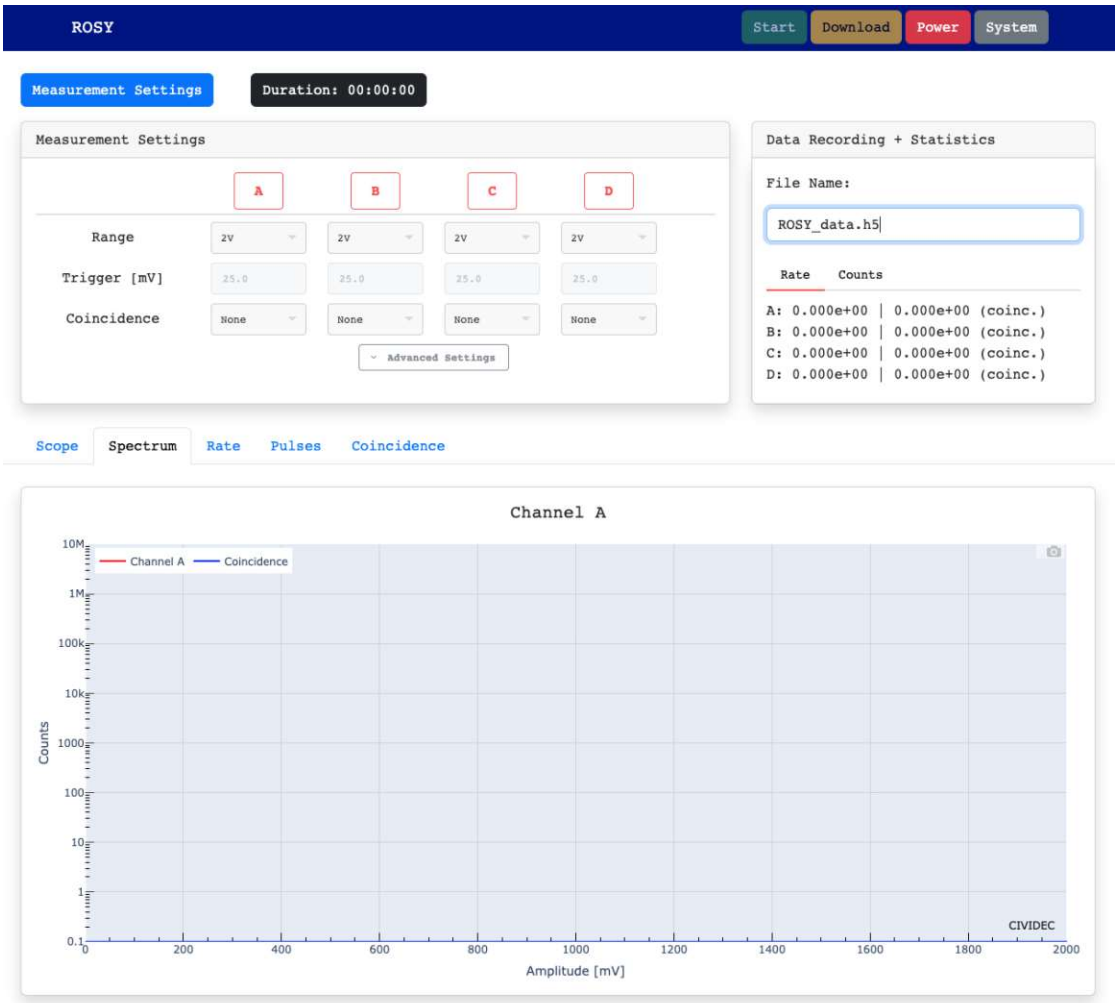

Figure 1.15: The GUI of the newly developed ROSY® Neutron Spectroscopy System when opening the corresponding IP-address in a browser. The Spectrum interface is shown.

Die approbierte gedruckte Originalversion dieser Diplomarbeit ist an der TU Wien Bibliothek verfügbar
The approved original version of this thesis is available in print at TU Wien Bibliothek.

Chapter 2

Measurement setup

The following chapter presents the facility in which the measurements were taken and a detailed description of the measurement setup. Additionally, neutron energy spectra from previous simulations of the source are presented, which are used in the following to compare the measurement result to GEANT4 simulations [43–45].

2.1 The NCSR Demokritos facility

The measurements were conducted at the 5.5 MV Tandem T11/25 Accelerator Laboratory of NCSR "Demokritos" in Athens [2]. The Tandem accelerator is capable of using different particles and target materials to produce neutrons in the energy range from 120 keV to 21 MeV [46]. For all presented measurements the ^{3}H(p,n)^{3}He reaction was used, capable of producing neutrons in the energy range from 2.0 MeV to 5.3 MeV [46]. The settings for the proton beam were chosen using NeuSDesc [47] and GEANT4 simulations. Table 2.1 denotes the proton energies and resulting neutron energies.

The measurement setup consists of the detector and the directly attached CxL amplifier. The detector was positioned 13 mm downstream of the flange, which encapsulates the tritium target. An overview of the beamline and the measurement setup is shown in figure 2.1. A close-up picture of the detector and the flange, showing the distance of 13 mm is shown in figure 2.2.

Die approbierte gedruckte Originalversion dieser Diplomarbeit ist an der TU Wien Bibliothek verfügbar
The approved original version of this thesis is available in print at TU Wien Bibliothek.

Neutron energy [MeV]	Proton energy [MeV]
2.45 MeV	3.804 MeV
2.95 MeV	4.256 MeV
3.45 MeV	4.716 MeV
3.95 MeV	5.182 MeV

Table 2.1: The neutron energies and the required proton energies to produce the neutrons using the $^{3}H(p,n)^{3}He$ reaction.

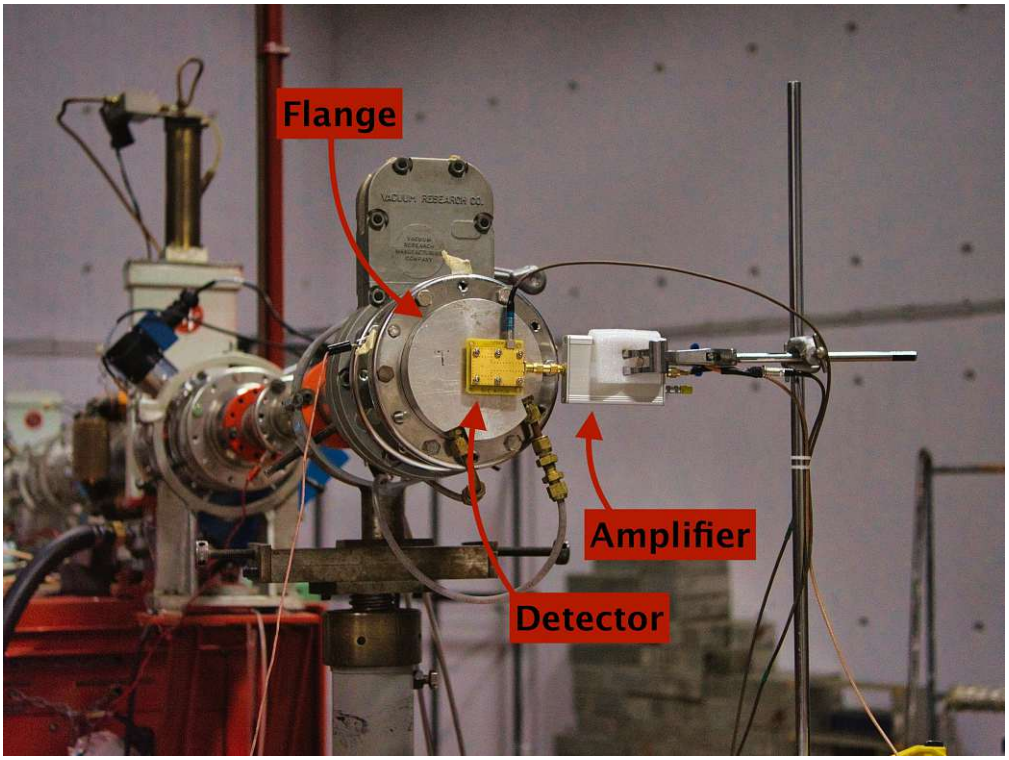

Figure 2.1: The experimental setup with the beamline in the background and the detector with an CxL amplifier in the foreground.

Die approbierte gedruckte Originalversion dieser Diplomarbeit ist an der TU Wien Bibliothek verfügbar
The approved original version of this thesis is available in print at TU Wien Bibliothek.

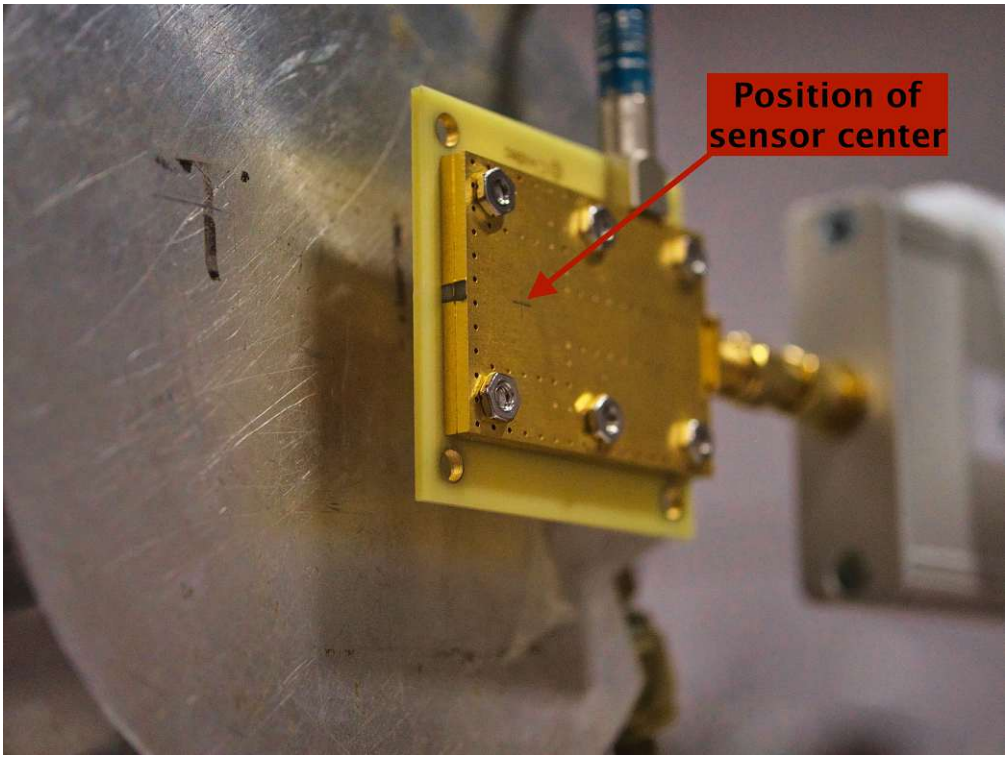

Figure 2.2: Close-up of the setup with the gap of 13 mm between flange and the detector.

The detector center was aligned with respect to the flange using a permanently installed telescope of the facility. These steps were performed whenever the detector was changed or touched, to guarantee the same conditions for each detector.

2.1.1 Neutron energies

Four different neutron energies were used for the detector comparison. The neutron spectra used to produce GEANT4 simulations are presented in the following. These were provided from the Demokritos facility and are used for all GEANT4 simulations and comparisons to the neutron response functions of the detectors. The neutron energy distribution for each nominal neutron energy is approximately monoenergetic with a maximum FWHM of 160 keV. The neutron distributions are a result of GEANT4 simulations of the complete Demokritos accelerator facility.

The 2.45 MeV neutron spectrum

The neutron energy distribution for the 2.45 MeV measurements is shown in log scale in figure 2.3 and in linear scale in figure 2.4. The mean value of the applied

Die approbierte gedruckte Originalversion dieser Diplomarbeit ist an der TU Wien Bibliothek verfügbar
The approved original version of this thesis is available in print at TU Wien Bibliothek.

Gaussian fit and its standard deviation is denoted.

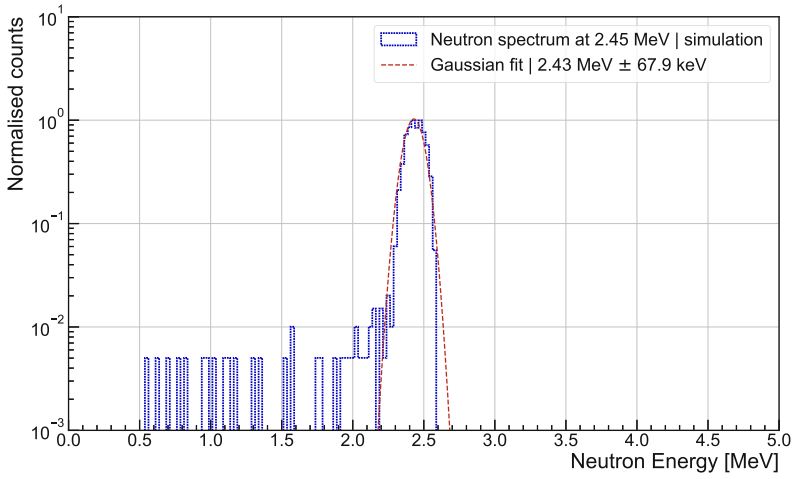

Figure 2.3: The neutron spectrum for the 2.45 MeV measurements in log scale

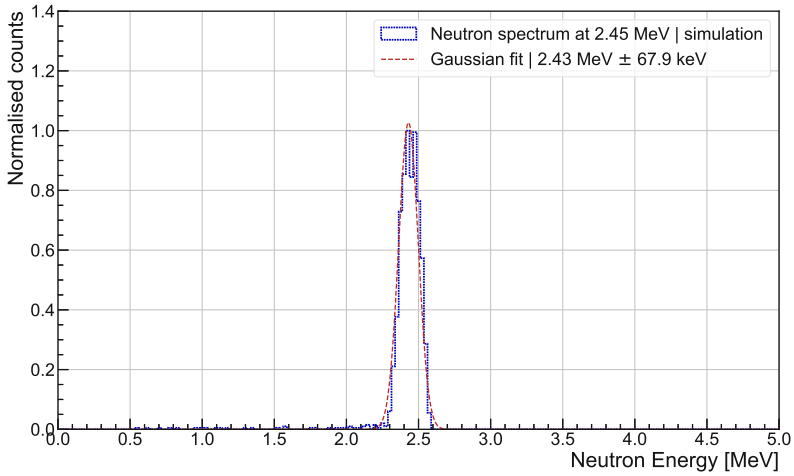

Figure 2.4: The neutron spectrum for the 2.45 MeV measurements in linear scale.

The neutron spectrum at 2.45 MeV shows a Gaussian like neutron energy distribution with its mean energy at 2.43 MeV and a FWHM of 160 keV. The energy spread corresponds to 6.58 % of the neutron mean energy, resulting in a quasi monoenergetic beam. It was used for all GEANT4 simulations of the detector neutron response at this neutron energy.

Die approbierte gedruckte Originalversion dieser Diplomarbeit ist an der TU Wien Bibliothek verfügbar
The approved original version of this thesis is available in print at TU Wien Bibliothek.

The 2.95 MeV neutron spectrum

The neutron energy distribution for the 2.95 MeV measurements is shown in log scale in figure 2.5 and in linear scale in figure 2.6. The mean value of the applied Gaussian fit and its standard deviation is denoted.

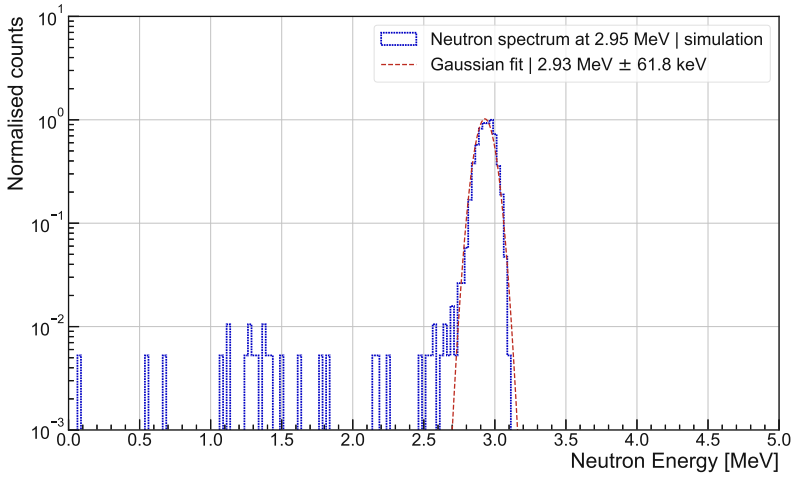

Figure 2.5: The neutron spectrum for the 2.95 MeV measurements in log scale.

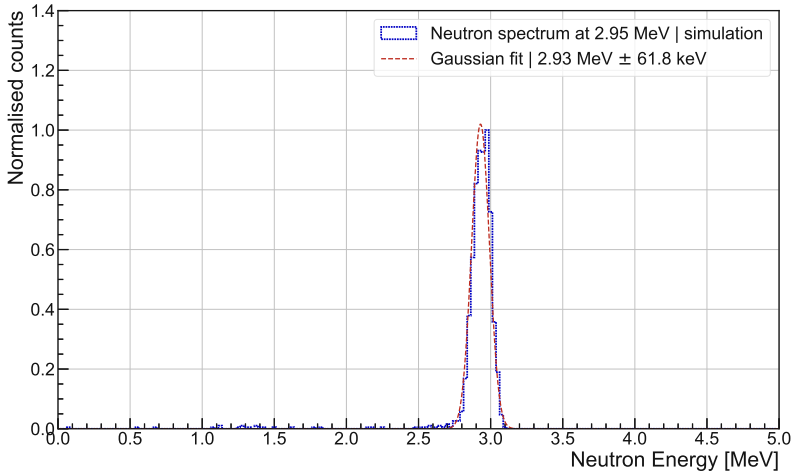

Figure 2.6: The neutron spectrum for the 2.95 MeV measurements in linear scale.

The neutron spectrum at 2.95 MeV shows a Gaussian like neutron energy distribution with its mean energy at 2.93 MeV and a FWHM of 146 keV. The energy spread corresponds to 4.97 % of the neutron mean energy, resulting in a quasi monoenergetic beam. It was used for all GEANT4 simulation of the detector neutron response at this neutron energy.

Die approbierte gedruckte Originalversion dieser Diplomarbeit ist an der TU Wien Bibliothek verfügbar
The approved original version of this thesis is available in print at TU Wien Bibliothek.

The 3.45 MeV neutron spectrum

The neutron energy distribution for the 3.45 MeV measurements is shown in log scale in figure 2.7 and in linear scale in figure 2.8. The mean value of the applied Gaussian fit and its standard deviation is denoted.

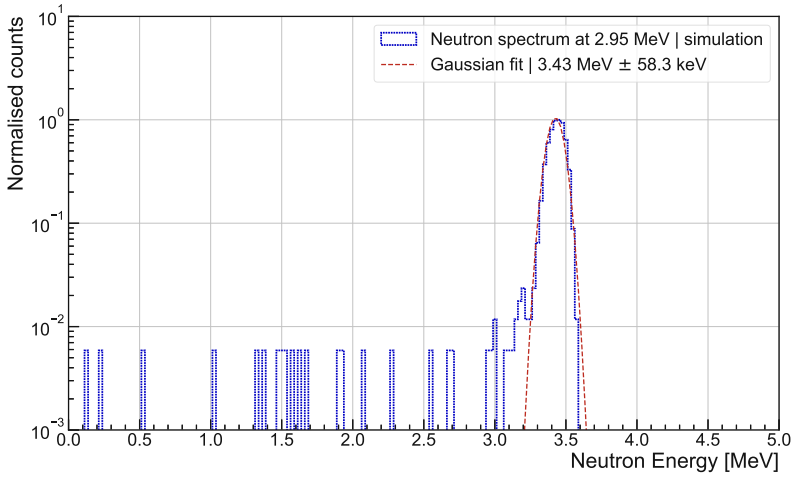

Figure 2.7: The neutron spectrum for the 3.45 MeV measurements in log scale.

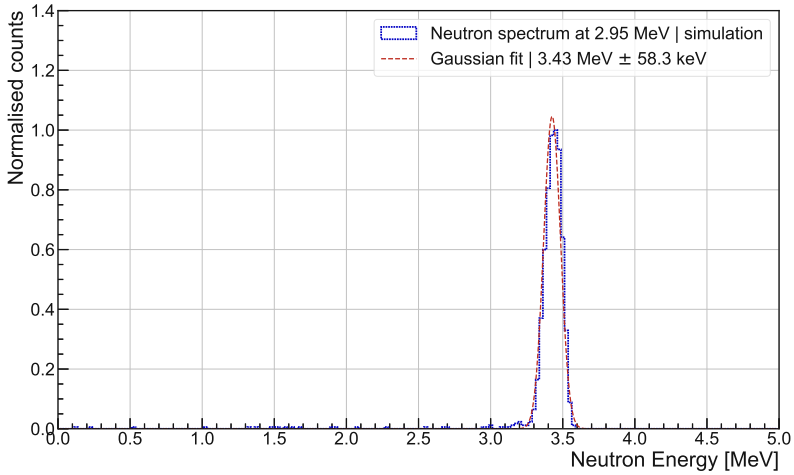

Figure 2.8: The neutron spectrum for the 3.45 MeV measurements in linear scale.

The neutron spectrum at 2.95 MeV shows a Gaussian like neutron energy distribution with its mean energy at 3.43 MeV and a FWHM of 137 keV. The energy spread corresponds to 4.01 % of the neutron mean energy, resulting in a quasi monoenergetic beam. It was used for all GEANT4 simulation of the detector neutron response at this neutron energy.

Die approbierte gedruckte Originalversion dieser Diplomarbeit ist an der TU Wien Bibliothek verfügbar
The approved original version of this thesis is available in print at TU Wien Bibliothek.

The 3.95 MeV neutron spectrum

The neutron energy distribution for the 3.95 MeV measurements is shown in log scale in figure 2.9 and in linear scale in figure 2.10. The mean value of the applied Gaussian fit and its standard deviation is denoted.

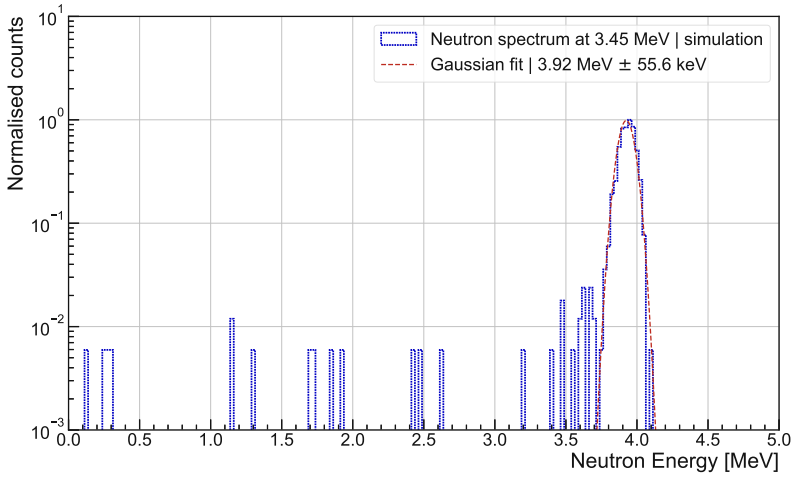

Figure 2.9: The neutron spectrum for the 3.95 MeV measurements in log scale.

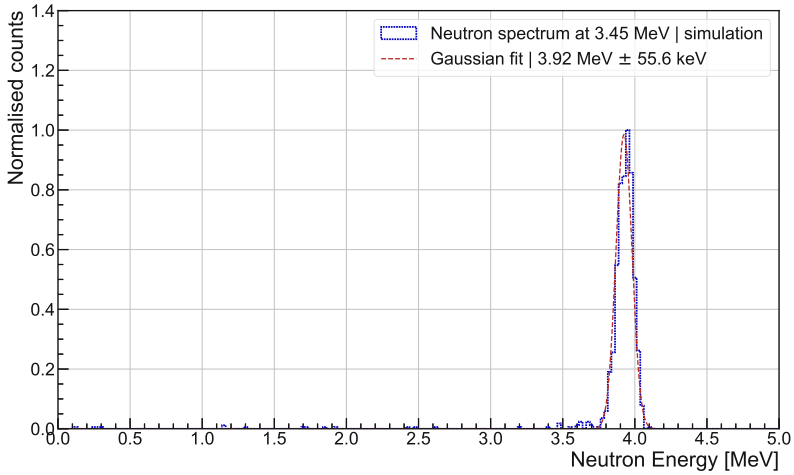

Figure 2.10: The neutron spectrum for the 3.95 MeV measurements in linear scale.

The neutron spectrum at 3.95 MeV shows a Gaussian like neutron energy distribution with its mean energy at 3.92 MeV and a FWHM of 131 keV. The energy spread corresponds to 3.34 % of the neutron mean energy, resulting in a quasi monoenergetic beam. It was used for all GEANT4 simulation of the detector neutron response at this neutron energy.

Die approbierte gedruckte Originalversion dieser Diplomarbeit ist an der TU Wien Bibliothek verfügbar
The approved original version of this thesis is available in print at TU Wien Bibliothek.

2.1.2 Neutron energies summary

The width of the energy distribution for all four neutron energies is less than 7 %, resulting in monoenergetic neutron beams. Table 2.2 contains the key parameters of the Gaussian fits to the simulated GEANT4 neutron energies.

Measurement	E_{mean} [MeV]	σ_{E_n} [keV]	FWHM_{E_n} [keV]
2.45 MeV	2.43 MeV	67.9 keV	160 keV
2.95 MeV	2.93 MeV	61.8 keV	146 keV
3.45 MeV	3.43 MeV	58.3 keV	137 keV
3.95 MeV	3.93 MeV	55.6 keV	131 keV

Table 2.2: The neutron energies from the GEANT4 simulation summarised with their standard deviations and FWHM.

The low energy spread allows for precise measurements at all neutron energies and enables a comprehensive comparison between the three detectors. Additionally, the relative energy spread decreases with increasing neutron energy, enhancing the neutron energy resolution even further.

2.1.3 The BF_3 reference detector

A BF_3 reference detector was utilised to monitor the neutron rate during the measurements and also to obtain a quantifiable comparison factor between the detectors. The data of the detector is saved automatically every 5 min. The detector is encapsulated in paraffin, which moderates the incoming neutrons to grant a constant conversion efficiency at all investigated neutron energies. The detector works due to the two possible neutron interactions with the ${}^{10}_{5}B$ inside the detector tube. The interaction produces a ${}^{7}_{3}Li$ and an ${}^{4}_{2}\alpha$ particle. Depending on whether the ${}^{7}_{3}Li$ is in its ground state or not, the deposited energy inside the detector varies due to the extra γ-ray produced in the excited state. The two possible branches are denoted in 2.1.

$$ {}^{10}_{5}B + {}^{1}_{0}n \rightarrow \begin{cases} {}^{7}_{3}Li + {}^{4}_{2}\alpha & \text{Q= 2.790 MeV (ground state)} \\ {}^{7}_{3}Li^{*} + {}^{4}_{2}\alpha + \gamma & \text{Q= 2.312 MeV (excited state)} \end{cases} \tag{2.1} $$

The ground state has Q=2.790 MeV, according to references [23, 24] with a branching ratio of 6.308 % [48]. The excited state of ${}^{10}_{5}B$ produces an additional

Die approbierte gedruckte Originalversion dieser Diplomarbeit ist an der TU Wien Bibliothek verfügbar
The approved original version of this thesis is available in print at TU Wien Bibliothek.

γ with an energy of 478 keV [49] which leaves the detector without any deposited energy, resulting in Q=2.312 MeV. The BF_3 reference detector spectrum is not used in the data analysis, but a reference amplitude spectrum for 2.45 MeV neutrons is shown in figure 2.11.

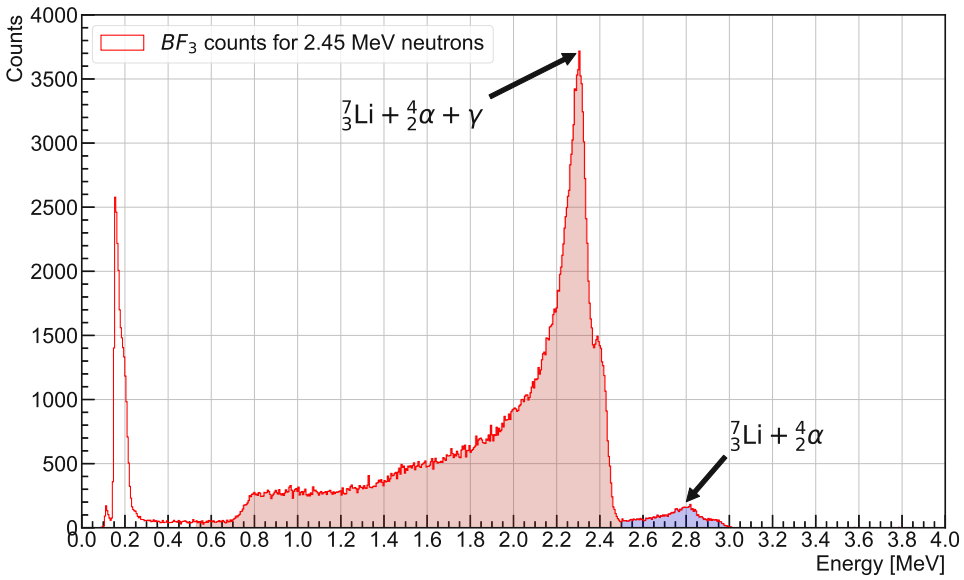

Figure 2.11: The spectrum of the used BF_3 reference detector at a run with 2.45 MeV neutrons.

The two peaks for the two possible branches are clearly visible with their respective energies in the BF_3 spectrum. The branching ratio during all measurements was stable at 3.19 % for the ground state and 96.81 % for the excited state of ^7_3Li. In the following, the sum of all counts above 0.53 MeV was divided by the acquisition time to get an average BF_3 neutron count rate (Γ_{BF_3}) as reference for the sCVD, SiC and Si detector. All counts below this threshold are counted as noise events and are therefore eliminated from all calculations.

2.2 Current Integrator

As an additional reference, the integrated proton beam current was recorded during all measurement runs. This results in an integrated beam current I_{beam}, from which the number of protons can be estimated with the help of the beam scale S_{beam}, following equation (2.2) and (2.3).

Die approbierte gedruckte Originalversion dieser Diplomarbeit ist an der TU Wien Bibliothek verfügbar
The approved original version of this thesis is available in print at TU Wien Bibliothek.

$$Q_{proton} = \frac{I_{beam}}{100} \times S_{beam} \tag{2.2}$$

$$N_{proton} = \frac{Q_{proton}}{e} \tag{2.3}$$

Dividing the number of protons (N_{proton}) by the acquisition time provides an average proton count rate (Γ_{proton}), which can be used to make comprehensive comparisons between the detectors investigated. The current integrator has a comparably big uncertainty compared to the BF_3 counter discussed previously, which is a disadvantage when used as a reference detector. However, when used in conjunction with a simulated conversion probability from protons to neutrons in the ^{3}H target, it could enable the calculation of a neutron detection efficiency.

The calculated proton flux Γ_{proton} for each detector measurement run is denoted in their respective chapter. The average Γ_{proton} of all investigated measurements was in the order of 2×10^{13} protons/s with S_{beam}=20 µA for all runs.

2.3 Measurement setup

The measurement setup was identical for all three detectors. As described previously and shown in figure 2.1, each detector was positioned in the center of the target and was directly connected to the CxL Spectroscopic Amplifier using a standard SMA male-male connector. The amplifier output was connected to the digitizer via a 50 Ω built-in coaxial cable with a length of approximately 50 m. The cable length attenuated the amplifier signal by 20 %, resulting in a lower perceived gain of the amplifier. This attenuation is visualised in figure 2.12 for a normalised CxL pulse and an estimated attenuation of 20 % over 50 m of coaxial cable.

Each sensor was built into the same detector PCB structure, equipped with the read-out line, previously mentioned, going to the CxL amplifier, and a separate bias voltage LEMO connector. All three detectors were biased using this dedicated bias input. The bias voltage depends on the detector thickness, the material and the desired polarity of the output pulse. Table 2.3 contains the bias voltage for all detectors used during the measurement campaign.

Each measurement was manually started and stopped to account for differences in count rate caused by beam settings, detector thickness, or interaction probabilities. No predefined count threshold was used to determine the end of a measurement, but rather a visual inspection of the recorded detector response function.

Die approbierte gedruckte Originalversion dieser Diplomarbeit ist an der TU Wien Bibliothek verfügbar
The approved original version of this thesis is available in print at TU Wien Bibliothek.
TU Bibliothek Your knowledge hub WIEN

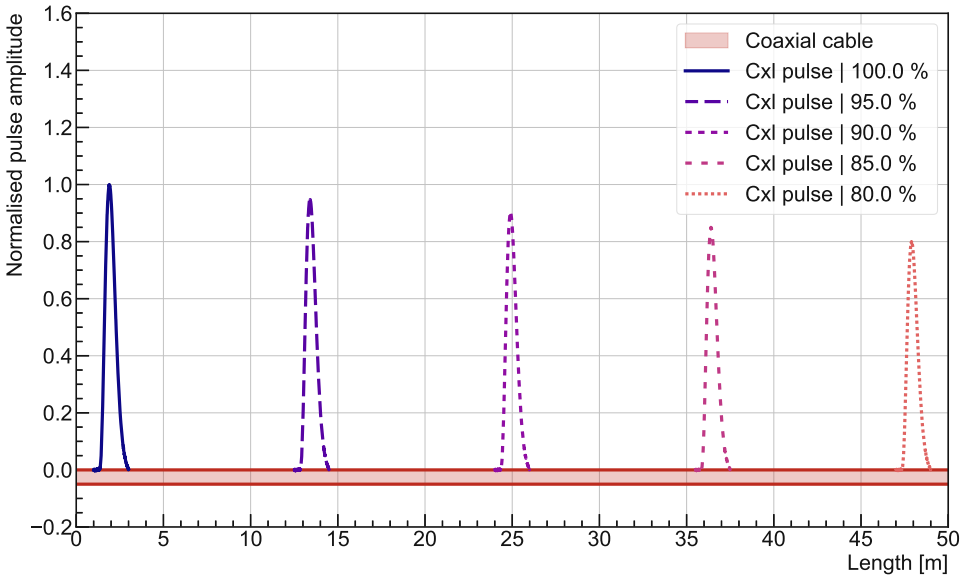

Figure 2.12: Visualisation of the pulse attenuation in a 50 m coaxial cable for a CxL pulse.

Detector	Bias voltage
sCVD detector	+50 V
SiC detector	-150 V
Si detector	+80 V

Table 2.3: Bias voltage for each detector.

2.4 Expected detector neutron response function

GEANT4 Monte-Carlo simulations [43–45] were conducted and compared to the measurement result. First, the neutron response function at 2.45 MeV for all detectors was simulated. A perfect monoenergetic neutron beam without any spatial or energy distribution was simulated to interact with 50 µm of the sensor material. No metallization or PCB structure was taken into account. This leads to the pure neutron response function without any additional interactions which need to be taken into account. In each simulation, the energy deposited in the detector is recorded for each interacting neutron. The resulting neutron response functions for all three detector contestants are shown in figure 2.13.

Die approbierte gedruckte Originalversion dieser Diplomarbeit ist an der TU Wien Bibliothek verfügbar
The approved original version of this thesis is available in print at TU Wien Bibliothek.

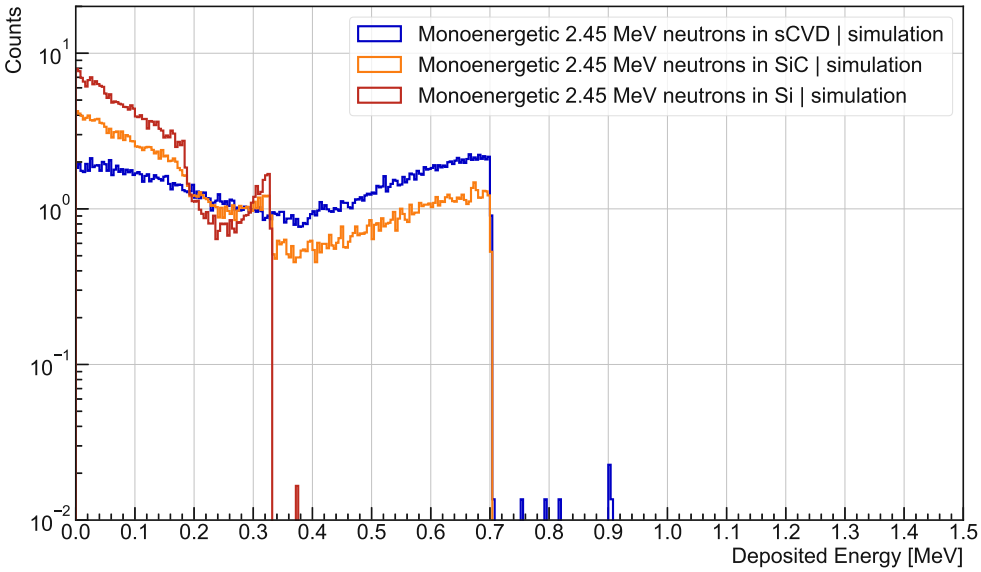

Figure 2.13: The neutron response function for a sCVD, SiC and Si detector to a monoenergetic beam of 2.45 MeV neutrons.

The maximum energy transfer due to elastic scattering is 0.696 MeV for ^{12}C and 0.326 MeV for ^{28}Si. Both cut-offs are clearly visible in the respective neutron response functions. The neutron response function of the SiC detector is a combination of the sCVD and Si detector response. The simulated response for each detector is discussed in detail below.

2.4.1 sCVD neutron response function

The sCVD neutron response function to a purely monoenergetic 2.45 MeV neutron beam is the idealised situation, which is a good estimation to a real experiment, but lacks the details of it. The neutron response function is influenced by two major factors:

1. The neutron energy distribution.
2. The electronic noise of the setup.

Accounting for the Demokritos energy distribution was done by using the simulated energy spectrum discussed in section 2.1.1 to distribute 50 mio simulated neutrons to follow the same energy distribution. This results in a slightly different

Die approbierte gedruckte Originalversion dieser Diplomarbeit ist an der TU Wien Bibliothek verfügbar
The approved original version of this thesis is available in print at TU Wien Bibliothek.

neutron response function in the sCVD detector due to the not monoenergetic neutron beam. Going a step further, the deposited energy spectrum from the real-world neutron energy distribution was convoluted with a Gaussian noise distribution with a standard deviation of 23 keV to account for the noise from the electronic read-out chain. Figure 2.14 compares the simulation results using different normalisations to highlight variations in the neutron response function.

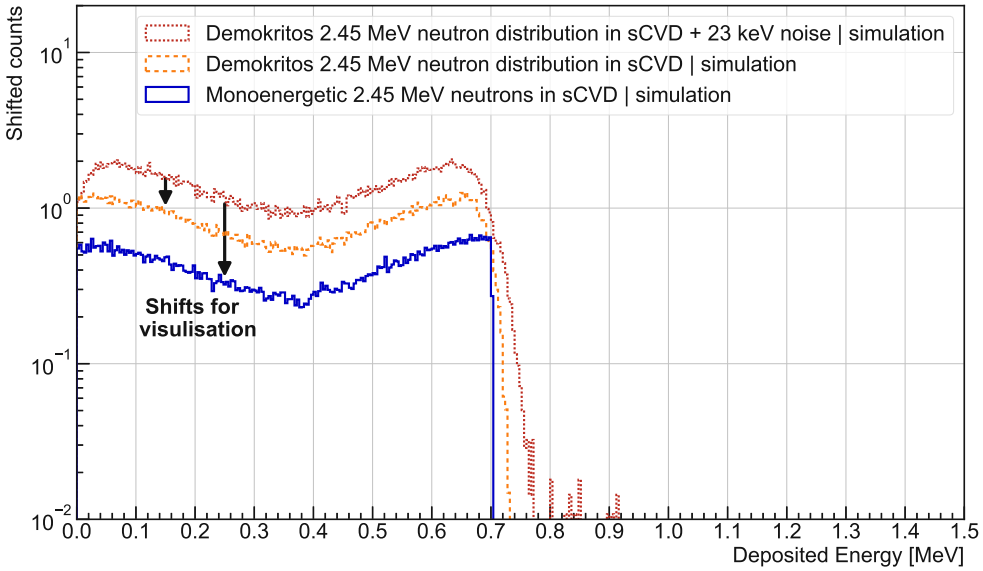

Figure 2.14: Comparison between the sCVD neutron response function to a monoenergetic 2.45 MeV neutron beam, the simulated neutron energy distribution shown in Fig. 2.3 and the latter convoluted with Gaussian noise with a standard deviation of 23 keV.

The impact of the neutron energy distribution from Demokritos is evident in the overall rounding and broadening of the spectrum and specifically at the maximum recoil cut-off. Additionally, the slope at the end of the spectrum, due to the maximum energy transfer in elastic scattering, is flattened. The effect of the added Gaussian noise is also evident in the same regions, as the effect is very similar. The maximum recoil edge gets blurred out even more and the minimum energy transfer, close to 0 MeV deposited energy, is decreased due to the noise. This is caused by the noise shifting some of the counts to negative energy values, i.e. the noise obscures some of the neutron interactions.

Die approbierte gedruckte Originalversion dieser Diplomarbeit ist an der TU Wien Bibliothek verfügbar
The approved original version of this thesis is available in print at TU Wien Bibliothek.

The latter of these three simulated neutron response functions is used for comparison with the measured response function as it is closest to reality in terms of neutron energy distribution and electronic noise. The same procedure was conducted for every neutron energy with the help of their respective energy distribution. The simulated response functions at all four neutron energies are shown in figure 2.15.

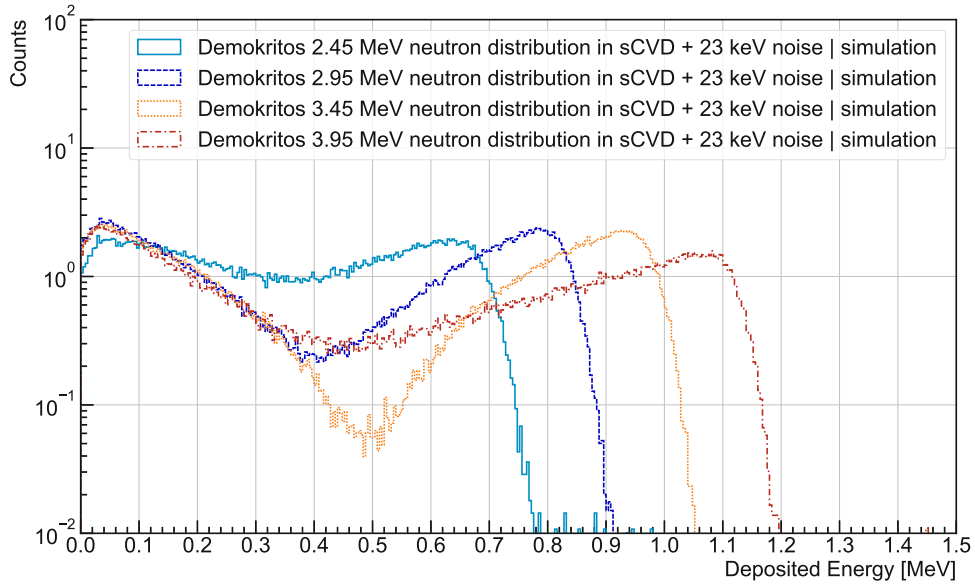

Figure 2.15: Comparison of the sCVD neutron response functions at each of the four different neutron energies using the simulated neutron spectra from Demokritos, each convoluted with a Gaussian noise distribution with a standard deviation of 23 keV.

The simulations show the broadening of the spectra due to the energy distribution and electronic noise. The deposited energy is related to the incoming neutron energy via the equation (1.1) with the probability for each angle determined by the angular cross section. As monoenergetic neutron beams were used for all measurements, the neutron energy is constant and the deposited energy spectrum is the result of the angular cross section. Therefore the maximum recoil energy corresponds to an angle of 180°. Furthermore, the simulations provide an interaction probability for a 50 µm sCVD sensor at the four investigated energies, denoted in table 2.4.

Die approbierte gedruckte Originalversion dieser Diplomarbeit ist an der TU Wien Bibliothek verfügbar
The approved original version of this thesis is available in print at TU Wien Bibliothek.

Neutron energy	GEANT4 interaction probability
2.45 MeV	0.142 %
2.95 MeV	0.205 %
3.45 MeV	0.221 %
3.95 MeV	0.186 %

Table 2.4: Neutron interaction probability from GEANT4 simulations for a 50 µm sCVD sensor.

2.4.2 Si neutron response function

As for the sCVD detector, the neutron response function of a Si detector was simulated using a purely monoenergetic beam of 2.45 MeV neutrons, the simulated neutron energy distribution from Demokritos and convolving the latter with a Gaussian noise of 45 keV. Figure 2.16 compares the simulation results using different normalisations to highlight variations in the neutron response function.

The cut-off energy broadens slightly due to the neutron energy distribution and even more because of the electronic noise. Noteworthy is, that almost all of the structure in the spectrum, in the monoenergetic spectrum quite distinctly visible, is covered by the noise. The angular distribution is visible but shows anisotropicity with a shift to lower angles, i.e. lower energies. Figure 2.17 shows the simulated neutron response function to the Demokritos neutron energy distribution convoluted with Gaussian noise for ^{28}Si at all four neutron energies.

The impact of the neutron energy distribution and especially the analogue noise is evident, as almost no structure is visible in the neutron response function. The angular distribution is anisotropic at all neutron energies, showing only a slight increase before the cut-off recoil energy. The interaction probability in the GEANT4 simulation for a 50 µm Si sensor are denoted in table 2.5.

2.4.3 SiC neutron response function

The neutron response function of a SiC detector is the combination of the sCVD and Si response function, as it consists of 50 % ^{12}C and 50 % ^{28}Si. It was simulated using a purely monoenergetic beam of 2.45 MeV neutrons, using the simulated neutron energy distribution from Demokritos and convolving the latter with a Gaussian noise of 35 keV. Figure 2.18 compares the simulation results using dif-

Die approbierte gedruckte Originalversion dieser Diplomarbeit ist an der TU Wien Bibliothek verfügbar
The approved original version of this thesis is available in print at TU Wien Bibliothek.

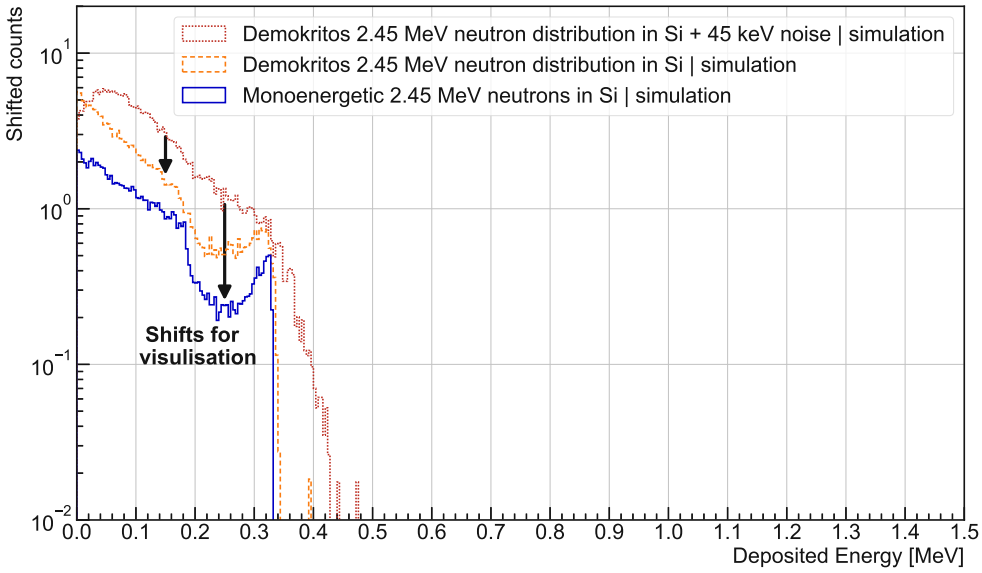

Figure 2.16: Comparison between the Si neutron response function to a monoenergetic 2.45 MeV neutron beam, the simulated neutron energy distribution shown in Fig. 2.3 and the latter convoluted with Gaussian noise with a standard deviation of 45 keV.

Neutron energy	GEANT4 interaction probability
2.45 MeV	0.066 %
2.95 MeV	0.062 %
3.45 MeV	0.058 %
3.95 MeV	0.054 %

Table 2.5: Neutron interaction probability from GEANT4 simulations for a 50 µm Si sensor.

ferent normalisations to highlight variations in the neutron response function.

In the monoenergetic simulation both the ^{28}Si recoil cut-off and the ^{12}C recoil cut-off can be identified. However, the Demokritos neutron distribution broadens the spectrum and partially obscures the ^{28}Si cut-off structure. With the additional noise of 35 keV the ^{28}Si cut-off practically disappears. This results in a neutron response function similar to that obtained with the sCVD detector. Figure 2.19

Die approbierte gedruckte Originalversion dieser Diplomarbeit ist an der TU Wien Bibliothek verfügbar
The approved original version of this thesis is available in print at TU Wien Bibliothek.

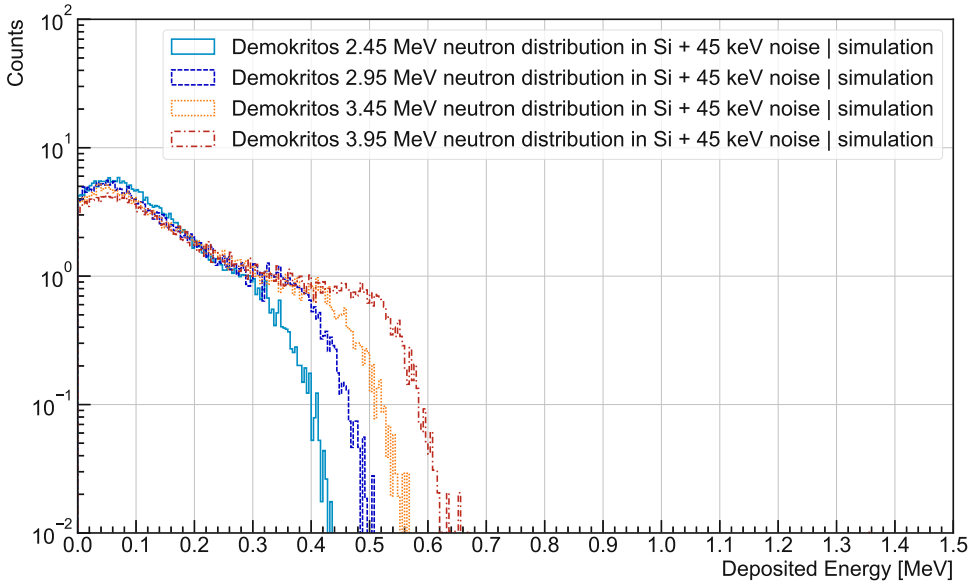

Figure 2.17: Comparison of the Si neutron response functions at each of the four different neutron energies using the simulated neutron spectra from Demokritos, each convoluted with a Gaussian noise distribution with a standard deviation of 45 keV.

shows the simulated neutron response function to the Demokritos neutron energy distribution convoluted with Gaussian noise for SiC at all four neutron energies.

The resulting neutron response functions look quiet similar to the sCVD simulations, as the broadening due to the neutron distribution and additional noise, masks the ^{28}Si recoil cut-off structure in the spectrum. The angular distributions are dominated by the angular distribution originating from 50 % ^{12}C. The interaction probability from the GEANT4 simulations for a 50 µm SiC sensor are denoted in table 2.6.

Die approbierte gedruckte Originalversion dieser Diplomarbeit ist an der TU Wien Bibliothek verfügbar
The approved original version of this thesis is available in print at TU Wien Bibliothek.

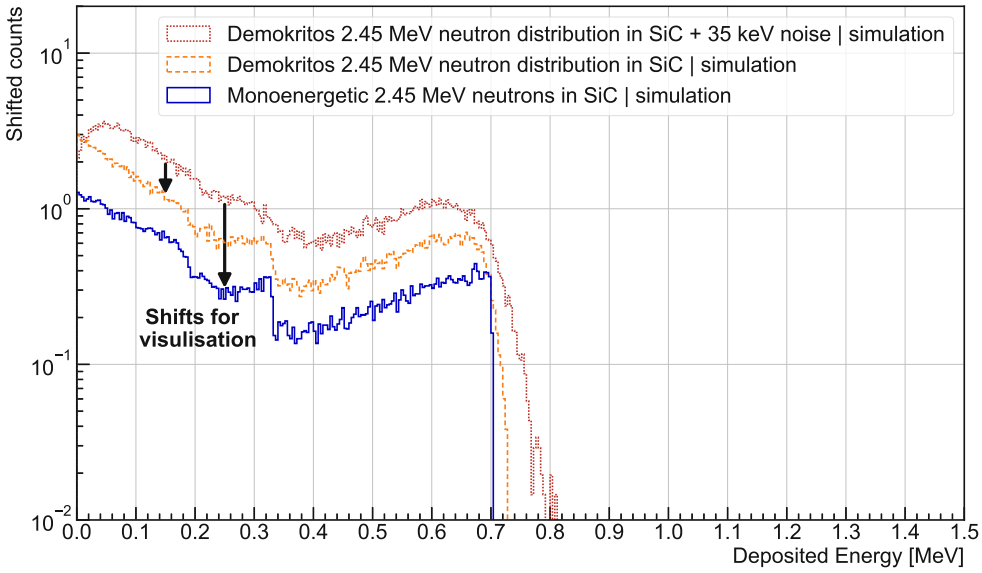

Figure 2.18: Comparison between the SiC neutron response function to a monoenergetic 2.45 MeV neutron beam, the simulated neutron energy distribution shown in Fig. 2.3 and the latter convoluted with Gaussian noise with a standard deviation of 35 keV.

Neutron energy	GEANT4 interaction probability
2.45 MeV	0.110 %
2.95 MeV	0.137 %
3.45 MeV	0.142 %
3.95 MeV	0.122 %

Table 2.6: Neutron interaction probability from GEANT4 simulations for a 50 µm SiC sensor.

2.4.4 Noise distribution differences

As described previously, each contestant detector was convoluted with a different Gaussian noise distribution. This is a result of the sensor material and its capacity. The noise level was determined by convoluting the respective Geant4 simulations with different noise distributions and determining the best match. This resulted

Die approbierte gedruckte Originalversion dieser Diplomarbeit ist an der TU Wien Bibliothek verfügbar
The approved original version of this thesis is available in print at TU Wien Bibliothek.

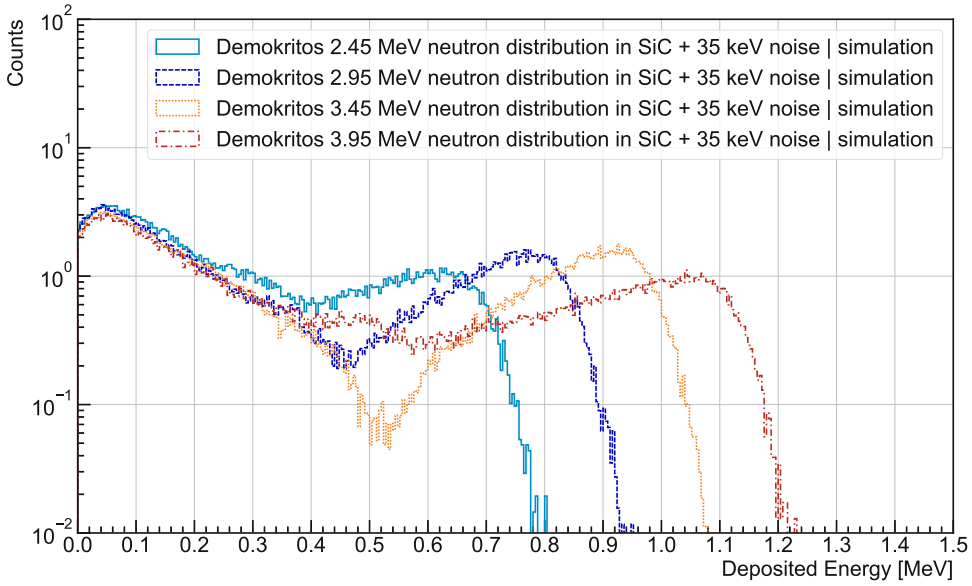

Figure 2.19: Comparison of the SiC neutron response functions at each of the four different neutron energies using the simulated neutron spectra from Demokritos, each convoluted with a Gaussian noise distribution with a standard deviation of 35 keV.

in a Gaussian distribution with a standard deviation of 23 keV for sCVD, 34 keV for SiC and 45 keV for Si. The impact of increased noise level can be seen in the resulting neutron response functions and its loss of distinct features in it.

Die approbierte gedruckte Originalversion dieser Diplomarbeit ist an der TU Wien Bibliothek verfügbar
The approved original version of this thesis is available in print at TU Wien Bibliothek.

Chapter 3

sCVD diamond detector response

The following chapter presents the measurement results obtained with the sCVD detector with 2.45 MeV, 2.95 MeV, 3.45 MeV and 3.95 MeV neutrons. The data processing follows the same steps at each measurement. The raw data is presented as the measured sCVD detector response function. After removing proton recoils coming from the PCB structure of the detector with the help of a linear fit and cutting off any remaining higher energy entries with a second linear fit, the measured neutron response function is shown. Due to the γ-background, only counts above the threshold at the angular distribution valley are counted as identifiable neutrons, resulting in an measured identifiable neutron response function. At higher energies the γ-background extends into the identifiable neutron domain but is still treated as a pure neutron signal to allow for a practical comparison in future measurements as precise simulations of the γ-background are not always available.

To allow a comprehensive comparison of the identifiable neutron response function, it is normalised to the counts from the BF_3 neutron counter. This is done by dividing the number of sCVD entries above the threshold by the acquisition time, giving an average sCVD neutron count rate (Γ_{sCVD}), and comparing this with Γ_{BF_3} for the same measurement period, resulting in the conversion factor ϵ_{sCVD} for sCVD neutron counts per BF_3 count.

A second comparison is done with the calculated number of protons, giving a conversion factor from protons to identifiable neutrons in the sCVD detector. This is done by comparing Γ_{sCVD} to Γ_{proton}.

Die approbierte gedruckte Originalversion dieser Diplomarbeit ist an der TU Wien Bibliothek verfügbar
The approved original version of this thesis is available in print at TU Wien Bibliothek.
TU Bibliothek Your knowledge hub WIEN

3.1 2.45 MeV sCVD response function

The sCVD detector response function at a neutron energy of 2.45 MeV normalised to the acquisition time is shown in figure 3.1 in 13-bit resolution. The trigger was set to 81.6 keV for the measurement. To deduct the correct neutron response function, a linear fit is used to remove the proton recoils coming from the detector PCB structure. To remove any higher energy entries, a linear fit to the maximum recoil cut-off energy slope was used. Using both fits, the neutron response function can be obtained. In the energy range of the neutron response function, 106 695 ± 10 % counts were removed due to the proton fit, accounting for the majority of the statistical neutron count error.

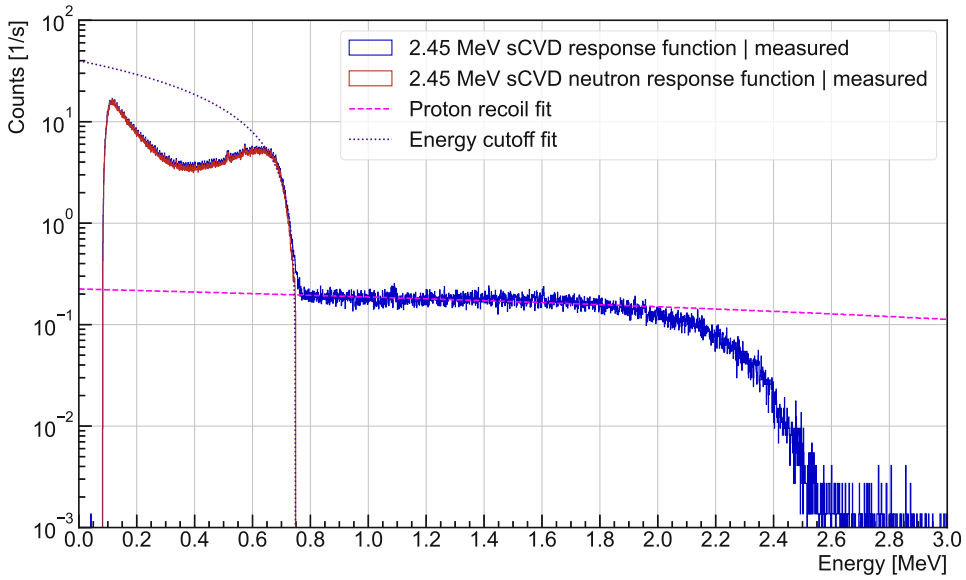

Figure 3.1: The measured sCVD neutron response function with a linear proton recoil and maximum cut-off energy fit for the 2.45 MeV sCVD measurement.

A comparison between the measured neutron response function and the GEANT4 simulation using the Demokritos neutron energy distribution convoluted with Gaussian noise with a standard deviation of 23 keV is shown in the top plot of figure 3.2. The bottom plot shows the relative difference between the measurement result and the simulation. The difference was used to estimate the noise level of all following sCVD measurement by convoluting the simulation with different Gaussian noise distributions and minimising the difference. This leads to a Gaussian noise distribution with a standard deviation of 23 keV.

Die approbierte gedruckte Originalversion dieser Diplomarbeit ist an der TU Wien Bibliothek verfügbar
The approved original version of this thesis is available in print at TU Wien Bibliothek.

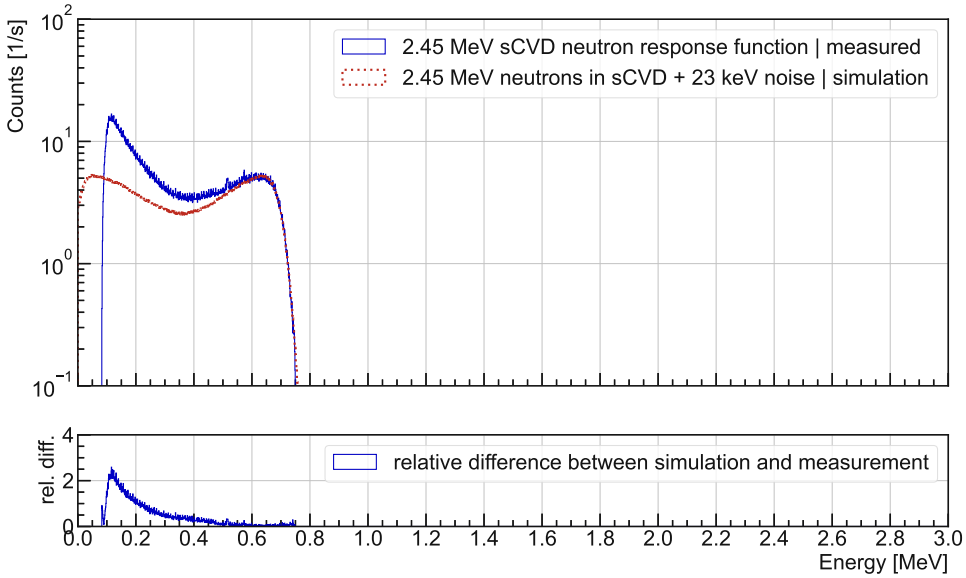

Figure 3.2: Comparison between the sCVD neutron response function at 2.45 MeV and the GEANT4 simulation.

By comparing the simulation and the measured neutron response function, two domains can be identified, separated by the threshold located at the valley of the angular distribution. Below the threshold, the difference between simulation and measurement is significant. This can best be explained by the γ-background inherent to neutron experiments. Above the threshold, the measurement is in good agreement with the simulation. It should be noted that the measurement and simulation are in good agreement at the cut-off above 0.7 MeV. The threshold is determined to be at 0.395 MeV. Figure 3.3 shows the measured sCVD neutron response function illustrating the two domains.

The number of identifiable neutrons above the threshold is 971 952 and the number of counts below the threshold is 1 570 777, accounting for a combination of neutrons and γ. This leads to 38.2 % of counts being identifiable neutrons. Comparing Γ_{sCVD} to Γ_{BF_3}, the factor $\epsilon_{sCVD_{2.45}}$ was determined to be 1.509 ± 0.017 identifiable neutron counts per BF_3 count, assuming the proton recoil number to be in the range of ± 10 % of the fit.

Using the integrated current measurement, the number of identifiable neutrons per proton was calculated to be $(6.5 \pm 2.0) \times 10^{-11}$. To obtain the interaction probability predicted by the GEANT4 simulation (0.142 %), the conversion from

Die approbierte gedruckte Originalversion dieser Diplomarbeit ist an der TU Wien Bibliothek verfügbar
The approved original version of this thesis is available in print at TU Wien Bibliothek.

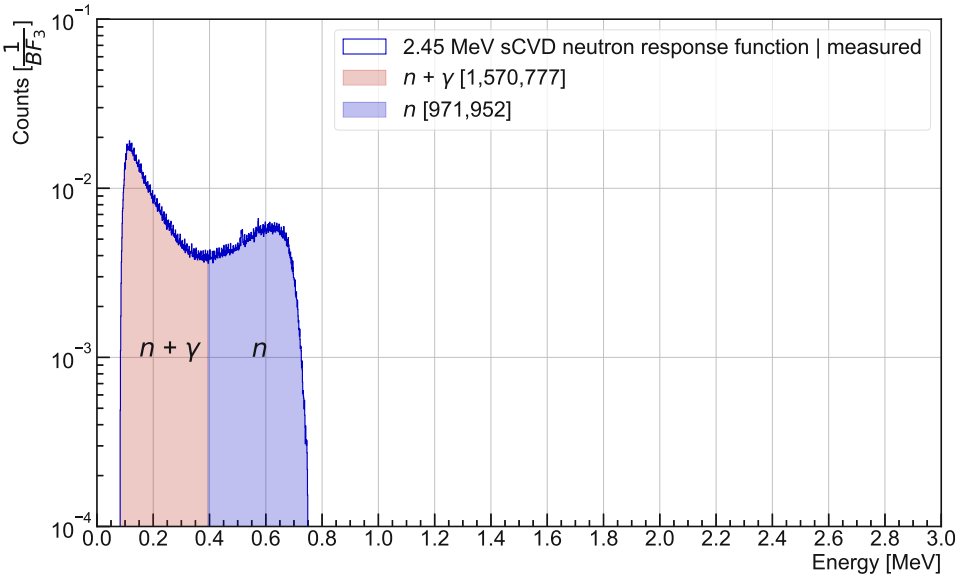

Figure 3.3: The sCVD measured neutron response function to 2.45 MeV neutrons, normalised to the BF_3 reference detector counts, illustrating the two different domains.

protons to neutrons should be 4.61×10^{-8} n/p in the ^{3}H target.

3.2 2.95 MeV sCVD response function

The sCVD detector response function at a neutron energy of 2.95 MeV normalised to the acquisition time is shown in figure 3.4. The trigger was set to 82.9 keV for the measurement. To deduct the correct neutron response function a linear fit is used to remove the proton recoils coming from the detector PCB structure. To remove any higher energy entries, a linear fit to the maximum recoil cut-off energy slope was used. Using both fits, the neutron response function can be obtained. In the energy range of the neutron response function, 171 152 ± 10 % counts were removed due to the proton fit, accounting for the majority of the statistical neutron count error.

A comparison between the measured neutron response function and the GEANT4 simulation using the Demokritos neutron energy distribution convoluted with Gaussian noise with a standard deviation of 23 keV is shown in the top plot of figure 3.5. The bottom plot shows the relative difference between the measurement result and the simulation.

Die approbierte gedruckte Originalversion dieser Diplomarbeit ist an der TU Wien Bibliothek verfügbar
The approved original version of this thesis is available in print at TU Wien Bibliothek.

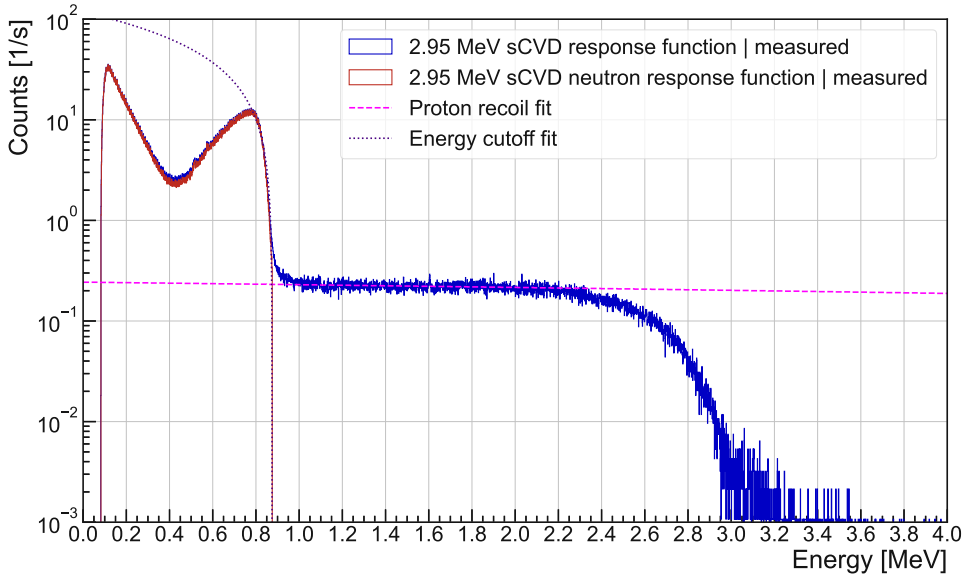

Figure 3.4: The measured sCVD response function with a linear proton recoil and maximum cut-off energy fit for the 2.95 MeV sCVD measurement.

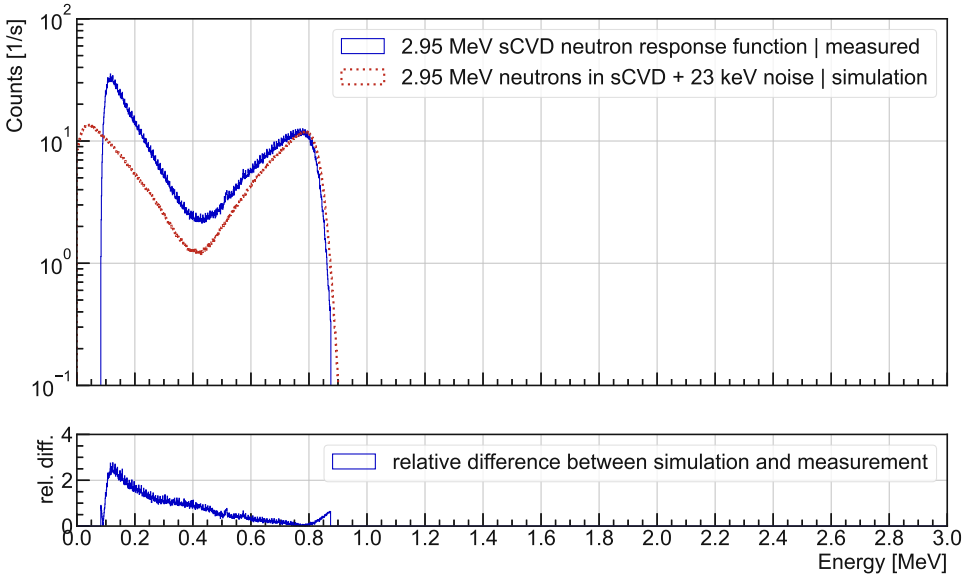

Figure 3.5: Comparison between the sCVD neutron response function at 2.95 MeV and the GEANT4 simulation.

Die approbierte gedruckte Originalversion dieser Diplomarbeit ist an der TU Wien Bibliothek verfügbar
The approved original version of this thesis is available in print at TU Wien Bibliothek.

The two domains below and above the valley are clearly distinguishable, with the former having a greater discrepancy between simulation and measurement due to the γ-background. The threshold is determined to be 0.438 MeV. Figure 3.6 shows the measured sCVD neutron response function illustrating the two domains.

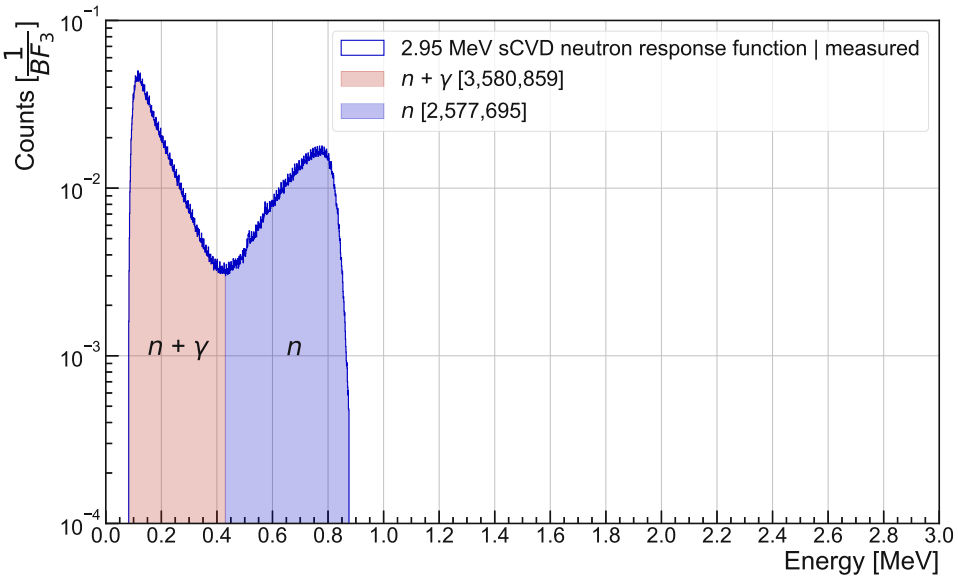

Figure 3.6: The sCVD measured neutron response function to 2.95 MeV neutrons, normalised to the BF_3 reference detector counts, illustrating the two different domains.

The number of identifiable neutrons above the threshold is 2 577 695 and the number of counts below the threshold is 3 580 859, accounting for a combination of neutrons and γ. This leads to 41.9 % of counts being identifiable neutrons. Comparing Γ_{sCVD} to Γ_{BF_3}, the factor $\epsilon_{sCVD_{2.95}}$ was determined to be 3.904 ± 0.026 identifiable neutron counts per BF_3 count, assuming the proton recoil number to be in the range of ± 10 % of the fit.

Using the integrated current measurement, the number of identifiable neutrons per proton was calculated to be $(1.3 \pm 0.4) \times 10^{-10}$. To obtain the interaction probability predicted by the GEANT4 simulation (0.205 %), the conversion from protons to neutrons should be 6.24×10^{-8} n/p in the ^{3}H target.

Die approbierte gedruckte Originalversion dieser Diplomarbeit ist an der TU Wien Bibliothek verfügbar
The approved original version of this thesis is available in print at TU Wien Bibliothek.

3.3 3.45 MeV sCVD response function

The sCVD detector response function at a neutron energy of 3.45 MeV normalised to the acquisition time is shown in figure 3.7. The trigger was set to 82.5 keV for the measurement. To deduct the correct neutron response function a linear fit is used to remove the proton recoils coming from the detector PCB structure. To remove any higher energy entries, a linear fit to the maximum recoil cut-off energy slope was used. Using both fits, the neutron response function can be obtained. In the energy range of the neutron response function, 208 550 ± 10 % counts were removed due to the proton fit, accounting for the majority of the statistical neutron count error.

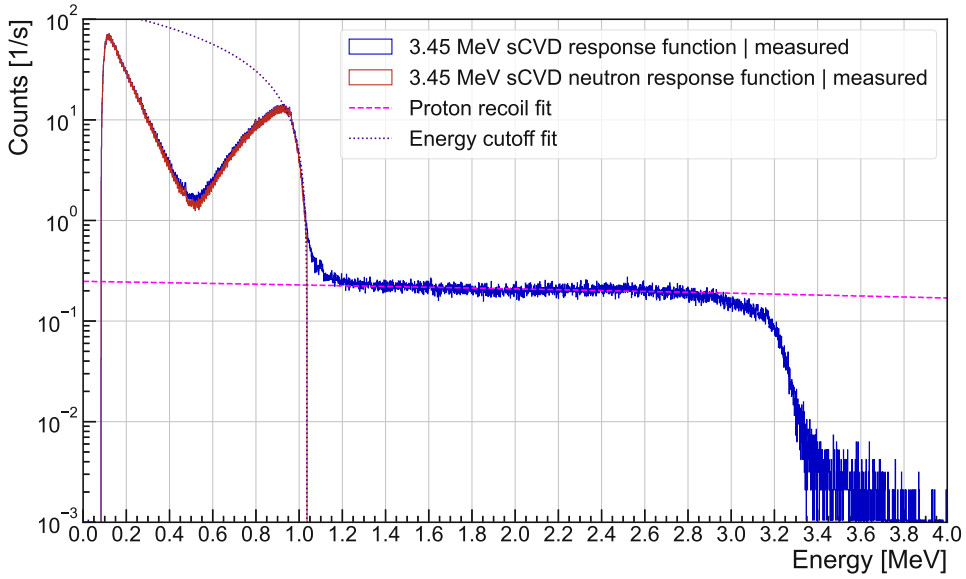

Figure 3.7: The measured sCVD response function with a linear proton recoil and maximum cut-off energy fit for the 3.45 MeV sCVD measurement.

The highest deposited energy in the raw data is at around 3.4 MeV, confirming that recoil protons with kinetic energies above that cannot deposit their full energy inside the sCVD detector. Instead, only a fraction can be deposited. Therefore a upper limit for the thickness of the sCVD sensor can be calculated as protons with the full neutron energy cannot be stopped inside the bulk material. A comparison between the measured neutron response function and the GEANT4 simulation using the Demokritos neutron energy distribution convoluted with Gaussian noise with a standard deviation of 23 keV is shown in the top plot of figure 3.8. The

Die approbierte gedruckte Originalversion dieser Diplomarbeit ist an der TU Wien Bibliothek verfügbar
The approved original version of this thesis is available in print at TU Wien Bibliothek.

bottom plot shows the relative difference between the measurement result and the simulation using the Demokritos neutron energy distribution and Gaussian noise with a standard deviation of 23 keV.

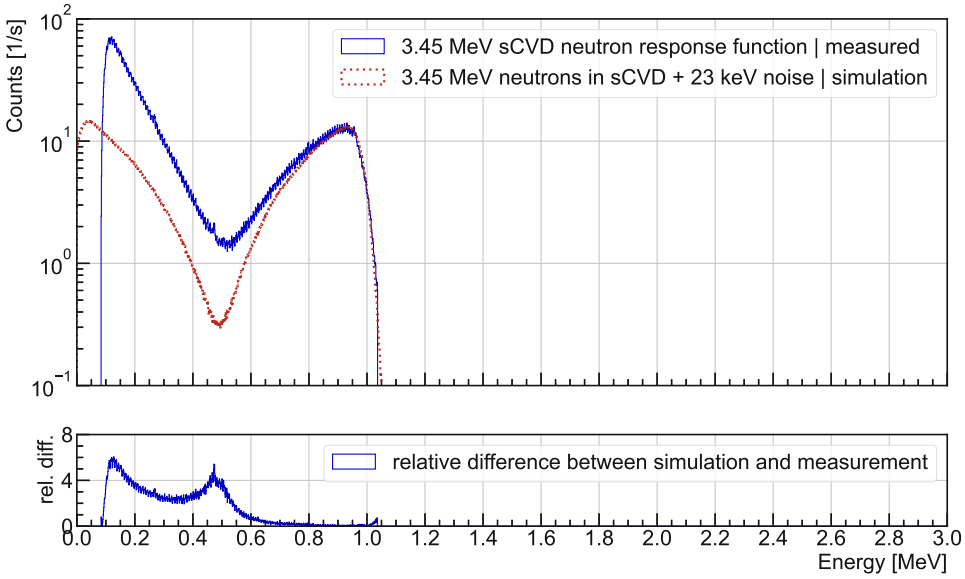

Figure 3.8: Comparison between the sCVD neutron response function at 3.45 MeV and the GEANT4 simulation.

The two domains are separated by the the valley at 0.518 MeV. The γ-background starts extending into the identifiable neutron domain. The relative difference shows two peaks at lower neutron energies, contrary to previous presented measurements. Figure 3.9 shows the measured sCVD neutron response function illustrating the two domains.

The number of identifiable neutrons above the threshold is 3 022 720 and the number of counts below the threshold is 7 443 437, accounting for a combination of neutrons and γ. This leads to 28.9 % of counts being identifiable neutrons. Comparing Γ_{sCVD} to Γ_{BF_3}, the factor $\epsilon_{sCVD_{3.45}}$ was determined to be 2.962 ± 0.021 identifiable neutron counts per BF_3 count, assuming the proton recoil number to be in the range of ± 10 % of the fit.

Using the integrated current measurement, the number of identifiable neutrons per proton was calculated to be $(1.8 \pm 0.5) \times 10^{-10}$. To obtain the interaction probability predicted by the GEANT4 simulation (0.221 %), the conversion from

Die approbierte gedruckte Originalversion dieser Diplomarbeit ist an der TU Wien Bibliothek verfügbar
The approved original version of this thesis is available in print at TU Wien Bibliothek.

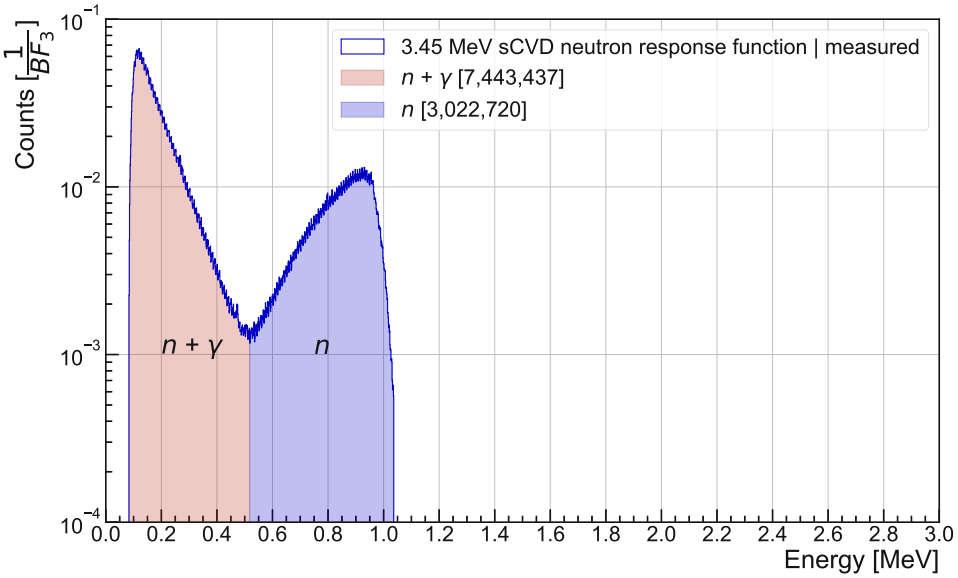

Figure 3.9: The sCVD measured neutron response function to 3.45 MeV neutrons, normalised to the BF_3 reference detector counts, illustrating the two different domains.

protons to neutrons should be 8.11×10^{-8} n/p in the ^{3}H target.

3.4 3.95 MeV sCVD response function

The sCVD detector response function at a neutron energy of 3.95 MeV normalised to the acquisition time is shown in figure 3.10. The trigger was set to 81.6 keV for the measurement. To deduct the correct neutron response function a linear fit is used to remove the proton recoils coming from the detector PCB structure. To remove any higher energy entries, a linear fit to the maximum recoil cut-off energy slope was used. Using both fits, the neutron response function can be obtained. In the energy range of the neutron response function, 90 754 ± 10 % counts were removed due to the proton fit, accounting for the majority of the statistical neutron count error.

The highest deposited energy in the raw data is at around 3.4 MeV, confirming that recoil protons with kinetic energies above that cannot deposit their full energy inside the sCVD detector. A comparison between the measured neutron response function and the GEANT4 simulation using the Demokritos neutron energy distribution convoluted with Gaussian noise with a standard deviation of 23 keV is

Die approbierte gedruckte Originalversion dieser Diplomarbeit ist an der TU Wien Bibliothek verfügbar
The approved original version of this thesis is available in print at TU Wien Bibliothek.

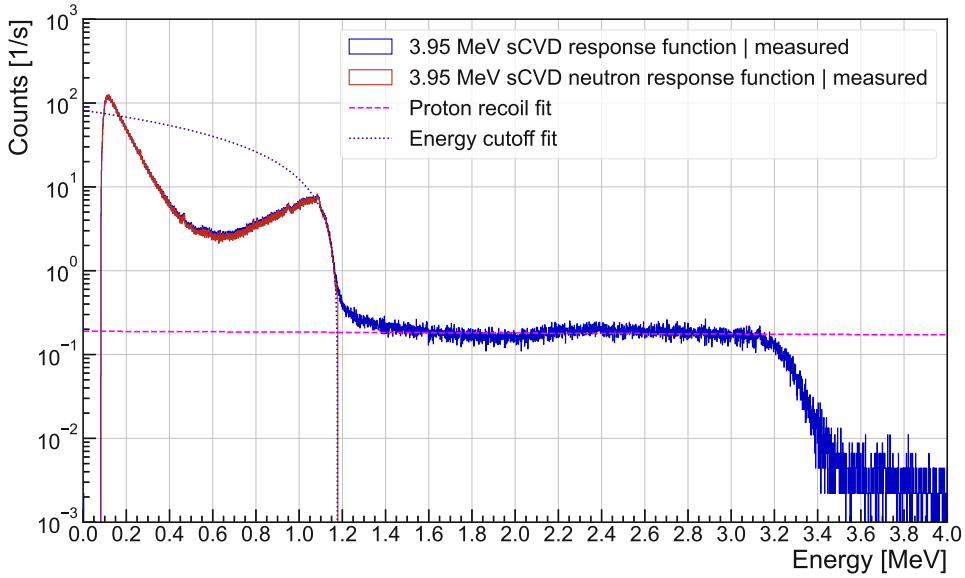

Figure 3.10: The measured sCVD response function with a linear proton recoil and maximum cut-off energy fit for the 3.95 MeV sCVD measurement.

shown in the top plot of figure 3.11. The bottom plot shows the relative difference between the measurement result and the simulation.

The valley between the two domains is determined to be at 0.628 MeV. In sharp contrast to the relative difference at 3.45 MeV the agreement of simulation and measurement improved. The γ-background shifts the angular distribution valley to a higher then expected value, leading to a pure neutron signal above the threshold. Figure 3.12 shows the measured sCVD neutron response function illustrating the two domains.

The number of identifiable neutrons above the threshold is 1 011 931 and the number of counts below the threshold is 6 282 591, accounting for a combination of neutrons and γ. This leads to 13.9 % of counts being identifiable neutrons. Comparing Γ_{sCVD} to Γ_{BF_3}, the factor $\epsilon_{sCVD_{3.95}}$ was determined to be 1.246 ± 0.011 identifiable neutron counts per BF_3 count, assuming the proton recoil number to be in the range of ± 10 % of the fit.

Using the integrated current measurement, the number of identifiable neutrons per proton was calculated to be $(1.2 \pm 0.4) \times 10^{-10}$. To obtain the interaction probability predicted by the GEANT4 simulation (0.186 %), the conversion from

Die approbierte gedruckte Originalversion dieser Diplomarbeit ist an der TU Wien Bibliothek verfügbar
The approved original version of this thesis is available in print at TU Wien Bibliothek.

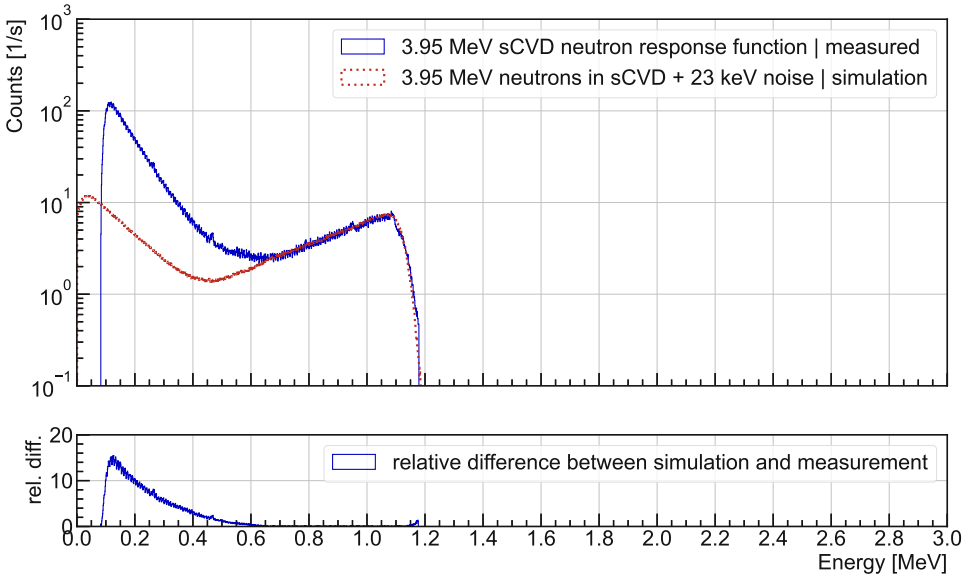

Figure 3.11: Comparison between the sCVD neutron response function at 3.95 MeV and the GEANT4 simulation.

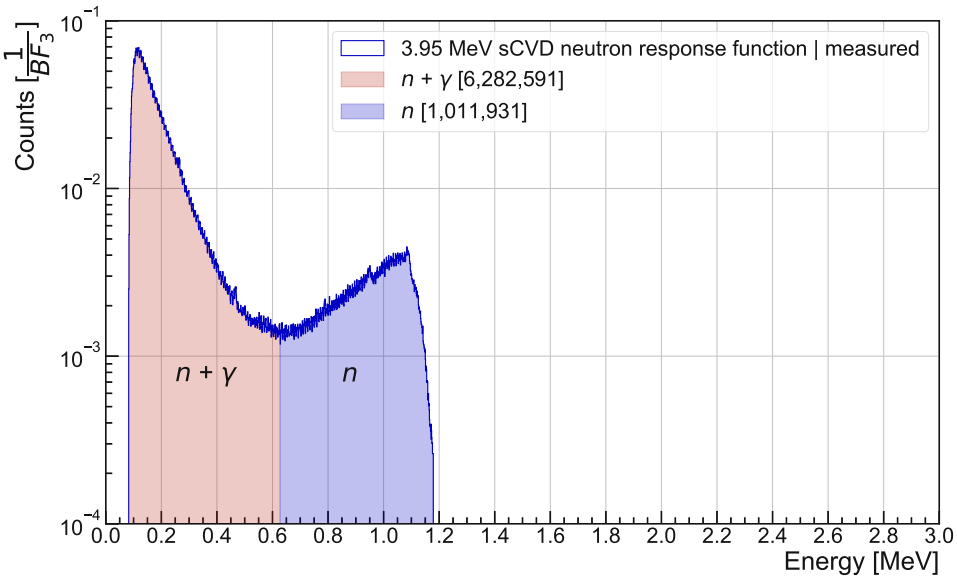

Figure 3.12: The sCVD measured neutron response function to 3.95 MeV neutrons, normalised to the BF_3 reference detector counts, illustrating the two different domains.

Die approbierte gedruckte Originalversion dieser Diplomarbeit ist an der TU Wien Bibliothek verfügbar
The approved original version of this thesis is available in print at TU Wien Bibliothek.

protons to neutrons should be 6.36×10^{-8} n/p in the ^{3}H target.

3.5 sCVD neutron response function comparison

The previous chapter presented the sCVD measured neutron response function at four different neutron energies. For all energies, the neutron response function was in good agreement with the simulations above a certain threshold. The main limitation to neutron identification is the γ-background, which increases with increasing neutron energy. This interferes with all comparisons, but is unavoidable in all fusion devices, making the comparison valid for practical use.

Therefore a comparison between the energies is valid and shows the changing deposited energy and angular distribution of the sCVD detector. Figures 3.13 shows the direct comparison of all measured sCVD neutron response functions, normalised to their respective BF_3 count rate.

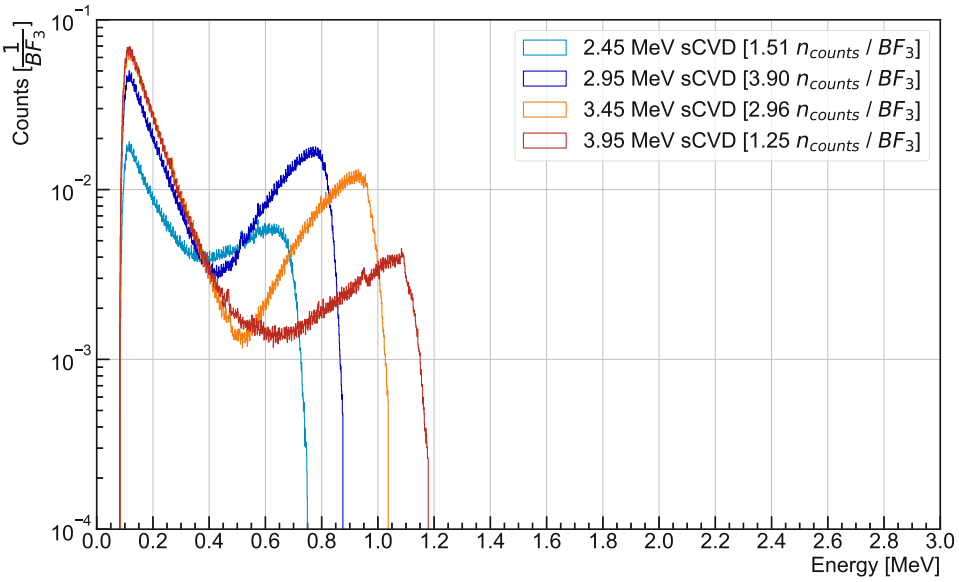

Figure 3.13: The measured sCVD neutron response function at the four neutron energies investigated, normalised to their respective BF_3 counts.

The similarity at low energies between the neutron response function at 2.95 MeV, 3.45 MeV and 3.95 MeV points to a γ-background which is increasing at neutron energies between 2.45 MeV and 2.95 MeV and then staying relatively constant.

Die approbierte gedruckte Originalversion dieser Diplomarbeit ist an der TU Wien Bibliothek verfügbar
The approved original version of this thesis is available in print at TU Wien Bibliothek.
TU Bibliothek Your knowledge hub WIEN

Using the identifiable neutron counts above their respective thresholds, the conversion factor ϵ_{sCVD} with their uncertainties, mainly due to the proton recoil fit, are shown in figure 3.14. The ^{12}C cross-section, normalised to $\epsilon_{sCVD_{2.45}}$, is shown as comparison.

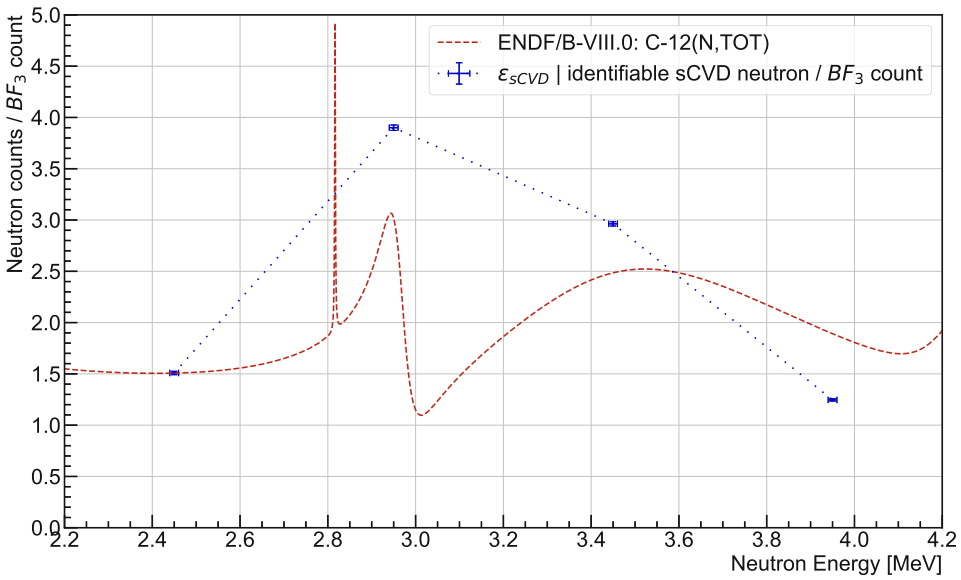

Figure 3.14: The identifiable neutron counts per BF_3 count, ϵ_{sCVD} at all neutron energies. The cross-section for ^{12}C, normalised to $\epsilon_{sCVD_{2.45}}$ at 2.1 MeV, is shown as comparison [25].

It is assumed that the BF_3 detector response is constant for all neutron energies, as it uses a neutron moderator. The deviation from the expected cross-section is therefore best explained by the γ-background. This results in all counts below the threshold being discarded, causing the deviation from the expected cross-section.

As additional comparison, figure 3.15 shows the comparison factor Γ_{sCVD} / Γ_{proton}. The normalised ^{12}C cross-section is added as comparison.

The current integrator agrees very well with the cross-section at neutron energies of 2.45 MeV and 2.95 MeV. The current integrator uncertainty of $\pm 30\,\%$ combined with the uncertain proton/neutron conversion percentage in the target prevents a comprehensive comparison between the different sCVD neutron response function at the investigated neutron energies. All key factors for the sCVD detector are summarised in table 3.1.

Die approbierte gedruckte Originalversion dieser Diplomarbeit ist an der TU Wien Bibliothek verfügbar
The approved original version of this thesis is available in print at TU Wien Bibliothek.

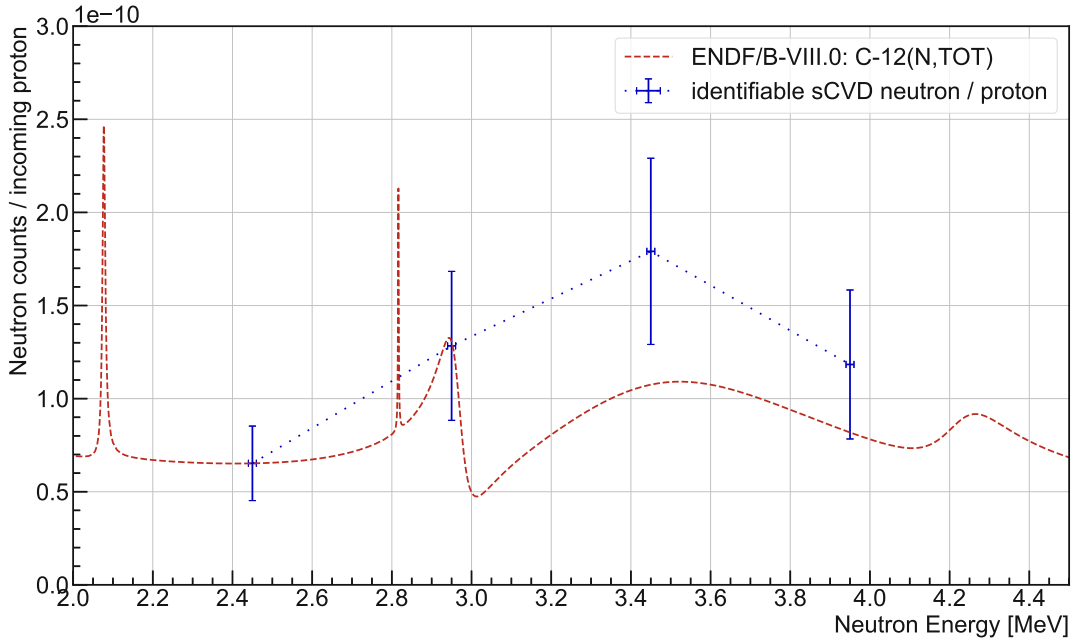

Figure 3.15: Number of identifiable sCVD neutron counts per proton using the current integrator. The ^{12}C cross-section, normalised to Γ_{sCVD} / Γ_{proton} at 2.1 MeV, is shown as comparison

$E_{neutron}$ [MeV]	$N_{neutrons}$ [%]	ϵ_{sCVD}	Γ_{sCVD} / Γ_{proton}
2.45 MeV	38.2 %	1.509 ± 0.017	$(6.5 \pm 2.0) \times 10^{-11}$
2.95 MeV	41.9 %	3.904 ± 0.026	$(1.3 \pm 0.4) \times 10^{-10}$
3.45 MeV	28.9 %	2.962 ± 0.021	$(1.8 \pm 0.5) \times 10^{-10}$
3.95 MeV	13.9 %	1.246 ± 0.011	$(1.2 \pm 0.4) \times 10^{-10}$

Table 3.1: Key results from the measured sCVD neutron response functions including the percentage of all counts being identifiable neutrons, the ϵ_{sCVD}-factor and the conversion from protons to identifiable neutrons.

Die approbierte gedruckte Originalversion dieser Diplomarbeit ist an der TU Wien Bibliothek verfügbar
The approved original version of this thesis is available in print at TU Wien Bibliothek.

Chapter 4

Silicon-Carbide detector response

The following chapter presents the measurement results obtained with the SiC detector with 2.45 MeV, 2.95 MeV, 3.45 MeV and 3.95 MeV neutrons. The data processing follows the same steps at each measurement and are identical to the sCVD data processing steps presented in chapter 3. The SiC detector is composed of 50 % carbon and 50 % silicon. Therefore, its detector response function will resemble that of the sCVD detector, particularly at the cut-off energy. The maximum cut-off energy is determined by the mass of the atom that interacts with the neutron, with ^{12}C being responsible for the highest possible energy transfer.

The SiC detector has a nominal thickness of 50 µm as the previous sCVD detector. Since the detector technology is still quite new, the exact depleted volume for the detector under investigation is not known in advance. With the comparison of count rate Γ_{SiC} and ϵ_{SiC} the thickness can be calculated with respect to the sCVD detector thickness of 50 µm.

A second comparison is done with the calculated number of protons, giving a conversion factor from protons to identifiable neutrons in the SiC detector. This is done by comparing Γ_{SiC} to Γ_{proton} to get a relative conversion factor.

4.1 2.45 MeV SiC response function

The SiC detector response function at a neutron energy of 2.45 MeV normalised to the acquisition time is shown in figure 4.1 with its full 13-bit resolution. The trigger was set to 102.1 keV for the measurement. To deduct the correct neutron response function a linear fit is used to remove the proton recoils coming from the detector PCB structure. To remove any higher energy entries, a linear fit to the maximum recoil cut-off energy slope was used. Using both fits, the neutron

Die approbierte gedruckte Originalversion dieser Diplomarbeit ist an der TU Wien Bibliothek verfügbar
The approved original version of this thesis is available in print at TU Wien Bibliothek.

response function can be obtained. In the energy range of the neutron response function, 67 193 ± 10 % counts were removed due to the proton fit, accounting for the majority of the statistical neutron count error.

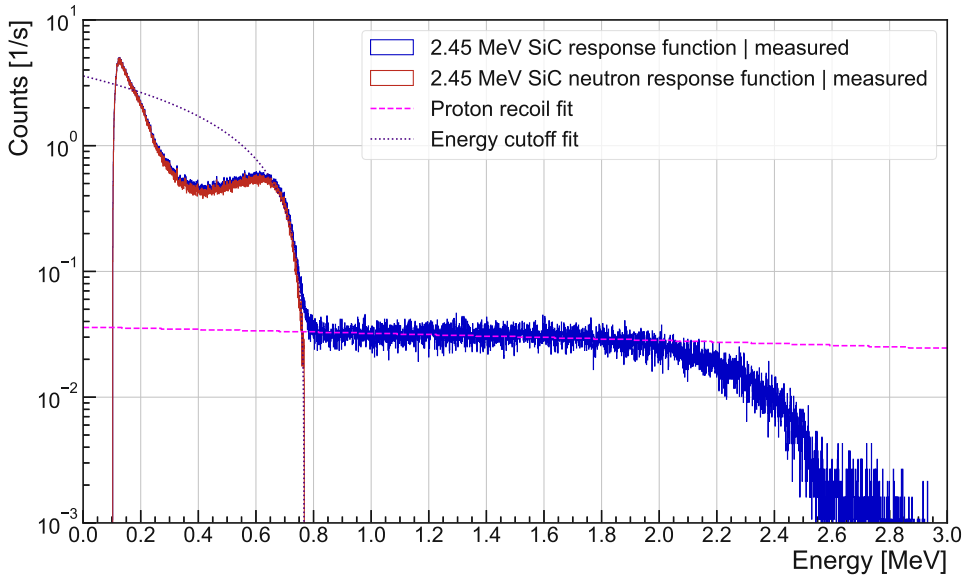

Figure 4.1: The measured SiC neutron response function with a linear proton recoil and maximum cut-off energy fit for the 2.45 MeV SiC measurement.

The highest deposited energy in the raw data is at around 2.45 MeV, confirming that recoil protons can deposit their full energy inside the SiC detector. A comparison between the measured neutron response function and the GEANT4 simulation using the Demokritos neutron energy distribution convoluted with Gaussian noise with a standard deviation of 35 keV is shown in the top plot of figure 4.2. The bottom plot shows the relative difference between the measurement result and the simulation.

Similar to the sCVD measurements, two domains can be identified, separated by the threshold located at the valley of the angular distribution. The threshold is determined to be at 0.415 MeV. Measurement and simulation agree well at the cut-off energy, but deviate from each other already above the threshold energy. Below the threshold the ^{28}Si cut-off can be seen in the simulation, which is absent in the measurement data. This and the strong deviation from the simulation can best be explained by the γ-background inherent to neutron experiments. Due to the energy distribution and maximum energy transfer for ^{28}Si, no neutron inter-

Die approbierte gedruckte Originalversion dieser Diplomarbeit ist an der TU Wien Bibliothek verfügbar
The approved original version of this thesis is available in print at TU Wien Bibliothek.

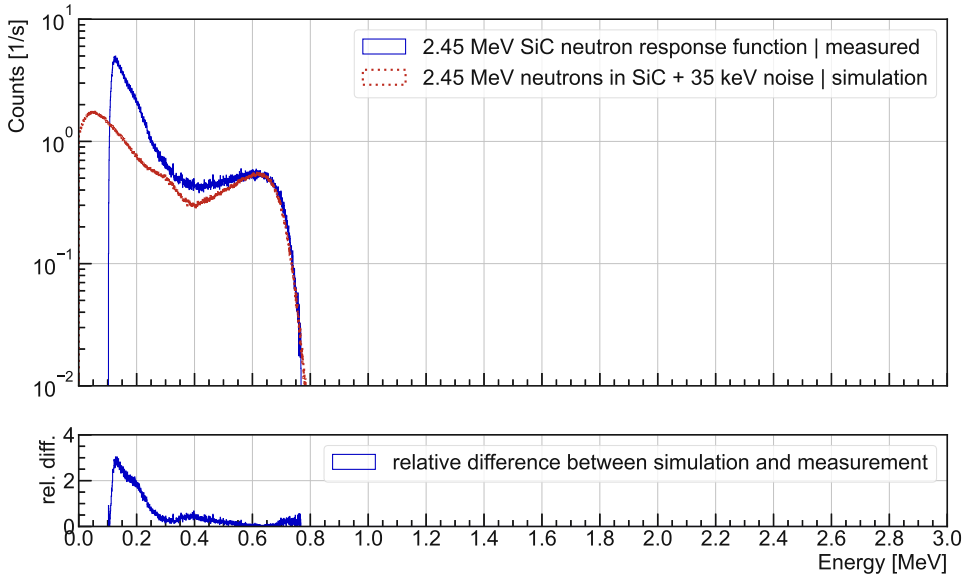

Figure 4.2: Comparison between the SiC neutron response function at 2.45 MeV and the GEANT4 simulation.

actions with ^{28}Si contribute to the identifiable neutron counts. This results in a 50 % reduction in neutron sensitivity due to the 50 % percentage of ^{28}Si in the bulk material of SiC and the similar neutron cross-section compared to ^{12}C . Figure 4.3 shows the measured SiC neutron response function illustrating the two domains.

The number of identifiable neutrons above the threshold is 429 494 and the number of counts below the threshold is 1 428 816, accounting for a combination of neutrons and γ. This leads to 23.1 % of counts being identifiable neutrons. Comparing Γ_{SiC} to Γ_{BF_3}, the factor $\epsilon_{SiC_{2.45}}$ was determined to be 0.280 ± 0.004 identifiable neutron counts per BF_3 count, assuming the proton recoil number to be in the range of ± 10 % of the fit.

Using the integrated current measurement, the number of identifiable neutrons per proton was calculated to be $(1.2 \pm 0.4) \times 10^{-11}$. To obtain the interaction probability predicted by the GEANT4 simulation (0.110 %), the conversion from protons to neutrons should be 1.06×10^{-8} n/p in the ^{3}H target.

Die approbierte gedruckte Originalversion dieser Diplomarbeit ist an der TU Wien Bibliothek verfügbar
The approved original version of this thesis is available in print at TU Wien Bibliothek.

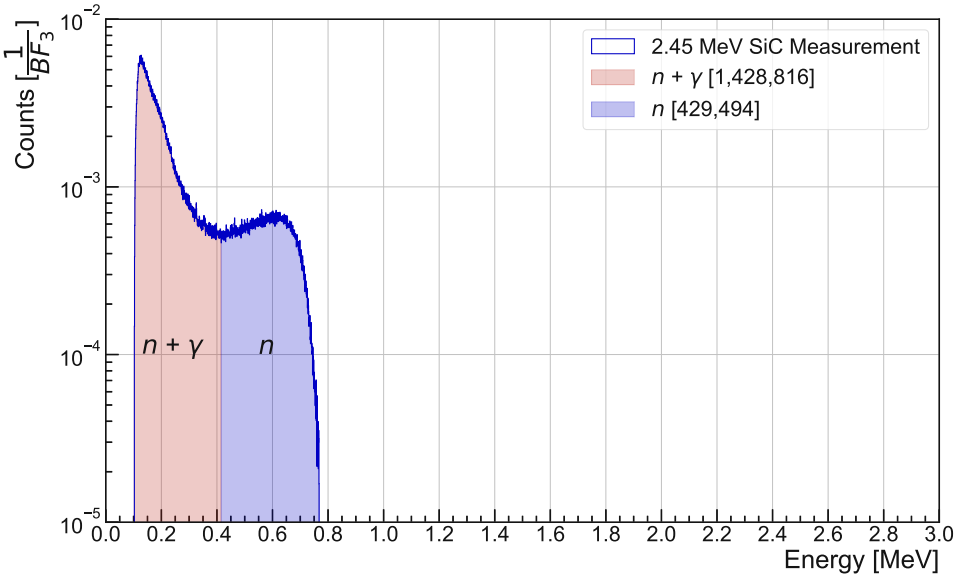

Figure 4.3: The SiC measured neutron response function to 2.45 MeV neutrons, normalised to the BF_3 reference detector counts, illustrating the two different domains.

4.2 2.95 MeV SiC response function

The SiC detector response function at a neutron energy of 2.95 MeV normalised to the acquisition time is shown in figure 4.4 with its full 13-bit resolution. The trigger was set to 100.1 keV for the measurement. To deduct the correct neutron response function a linear fit is used to remove the proton recoils coming from the detector PCB structure. To remove any higher energy entries, a linear fit to the maximum recoil cut-off energy slope was used. Using both fits, the neutron response function can be obtained. In the energy range of the neutron response function, 61 777 ± 10 % counts were removed due to the proton fit, accounting for the majority of the statistical neutron count error.

The highest deposited energy in the raw data is at around 2.70 MeV, confirming that recoil protons with kinetic energies above that cannot deposit their full energy inside the SiC detector. As for the sCVD detector, this sets an upper limit of the bulk material thickness. A comparison between the measured neutron response function and the GEANT4 simulation using the Demokritos neutron energy distribution convoluted with Gaussian noise with a standard deviation of 35 keV is shown in the top plot of figure 4.5. The bottom plot shows the relative difference between the measurement result and the simulation.

Die approbierte gedruckte Originalversion dieser Diplomarbeit ist an der TU Wien Bibliothek verfügbar
The approved original version of this thesis is available in print at TU Wien Bibliothek.

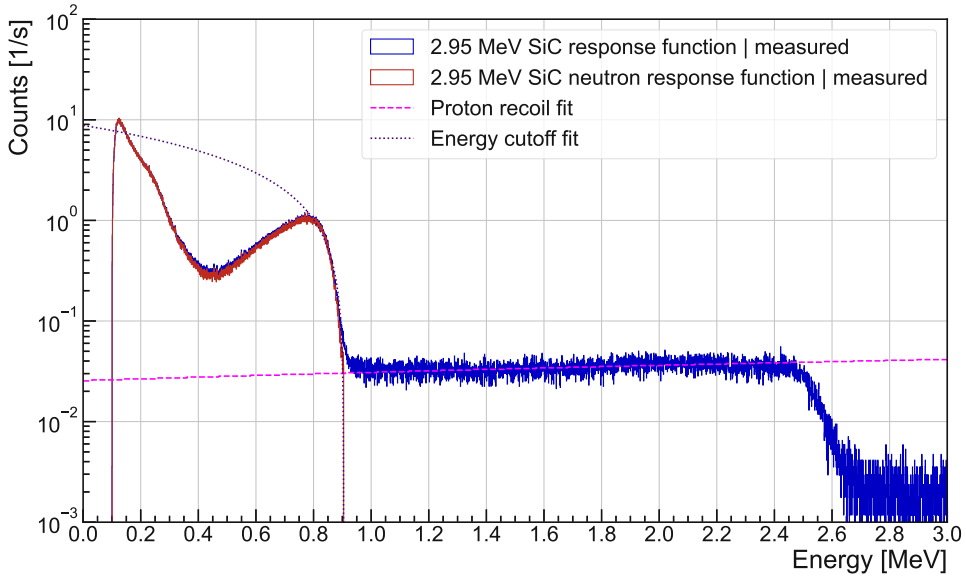

Figure 4.4: The measured SiC neutron response function with a linear proton recoil and maximum cut-off energy fit for the 2.95 MeV SiC measurement.

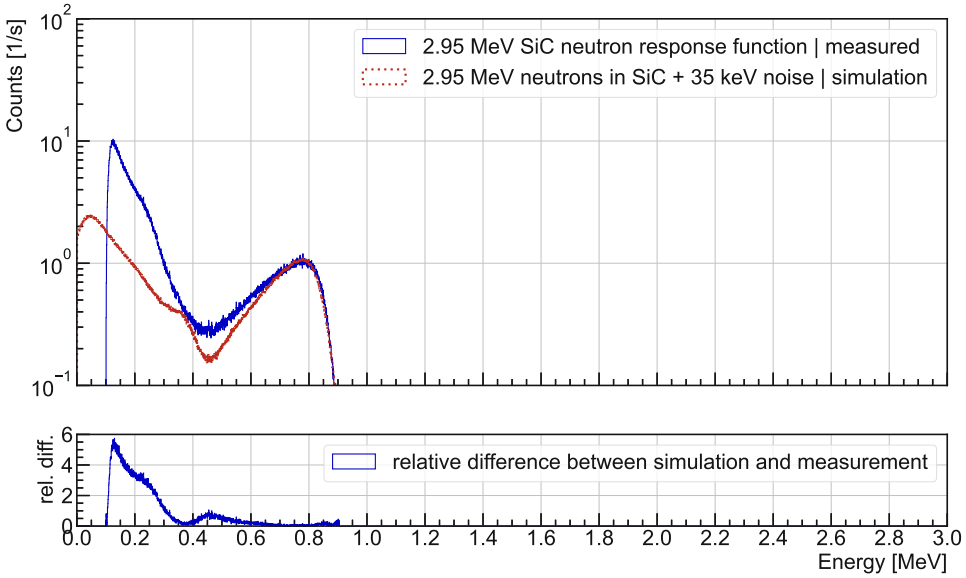

Figure 4.5: Comparison between the SiC neutron response function at 2.95 MeV and the GEANT4 simulation.

Die approbierte gedruckte Originalversion dieser Diplomarbeit ist an der TU Wien Bibliothek verfügbar
The approved original version of this thesis is available in print at TU Wien Bibliothek.

The two domains are separated by the threshold located at the valley of the angular distribution at 0.462 MeV. Measurement and simulation are in good agreement at the cut-off energy, but deviate already above the threshold energy. Below the threshold the ^{28}Si cut-off can be seen in the simulation, which is absent in the measurement data. Below the ^{28}Si cut-off, the strong deviation can be best explained by the strong γ-background. Figure 4.6 shows the measured SiC neutron response function illustrating the two domains.

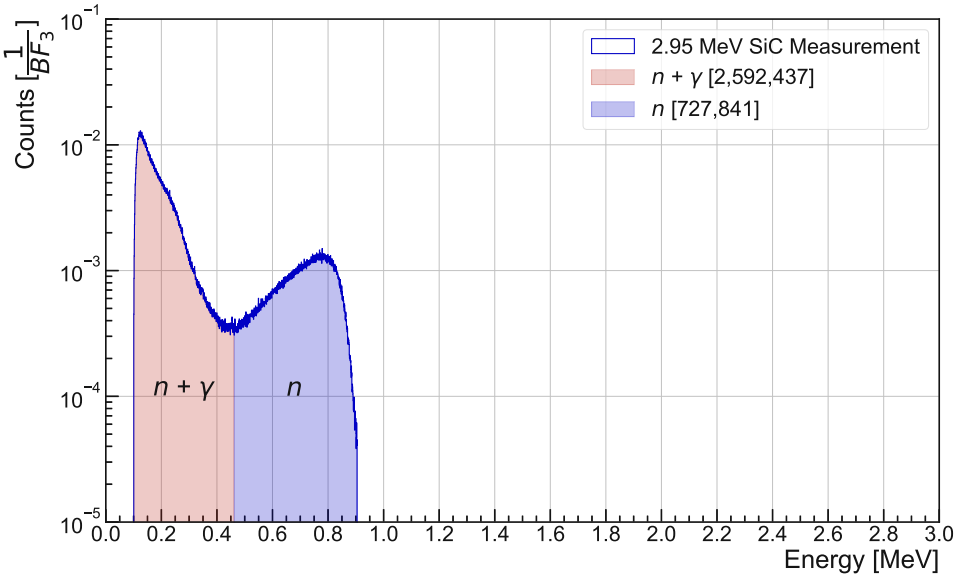

Figure 4.6: The SiC measured neutron response function to 2.95 MeV neutrons, normalised to the BF_3 reference detector counts, illustrating the two different domains.

The number of identifiable neutrons above the threshold is 727 841 and the number of counts below the threshold is 2 592 437, accounting for a combination of neutrons and γ. This leads to 21.9 % of counts being identifiable neutrons. Comparing Γ_{SiC} to Γ_{BF_3}, the factor $\epsilon_{SiC_{2.95}}$ was determined to be 0.538 ± 0.005 identifiable neutron counts per BF_3 count, assuming the proton recoil number to be in the range of ± 10 % of the fit.

Using the integrated current measurement, the number of identifiable neutrons per proton was calculated to be $(1.9 \pm 0.6) \times 10^{-11}$. To obtain the interaction probability predicted by the GEANT4 simulation (0.136 %), the conversion from protons to neutrons should be 1.40×10^{-8} n/p in the ^{3}H target.

Die approbierte gedruckte Originalversion dieser Diplomarbeit ist an der TU Wien Bibliothek verfügbar
The approved original version of this thesis is available in print at TU Wien Bibliothek.
TU Bibliothek Your knowledge hub WIEN

4.3 3.45 MeV SiC response function

The SiC detector response function at a neutron energy of 3.45 MeV normalised to the acquisition time is shown in figure 4.7 with its full 13-bit resolution. The trigger was set to 100.6 keV for the measurement. To deduct the correct neutron response function a linear fit is used to remove the proton recoils coming from the detector PCB structure. To remove any higher energy entries, a linear fit to the maximum recoil cut-off energy slope was used. Using both fits, the neutron response function can be obtained. In the energy range of the neutron response function, 69 830 ± 10 % counts were removed due to the proton fit, accounting for the majority of the statistical neutron count error.

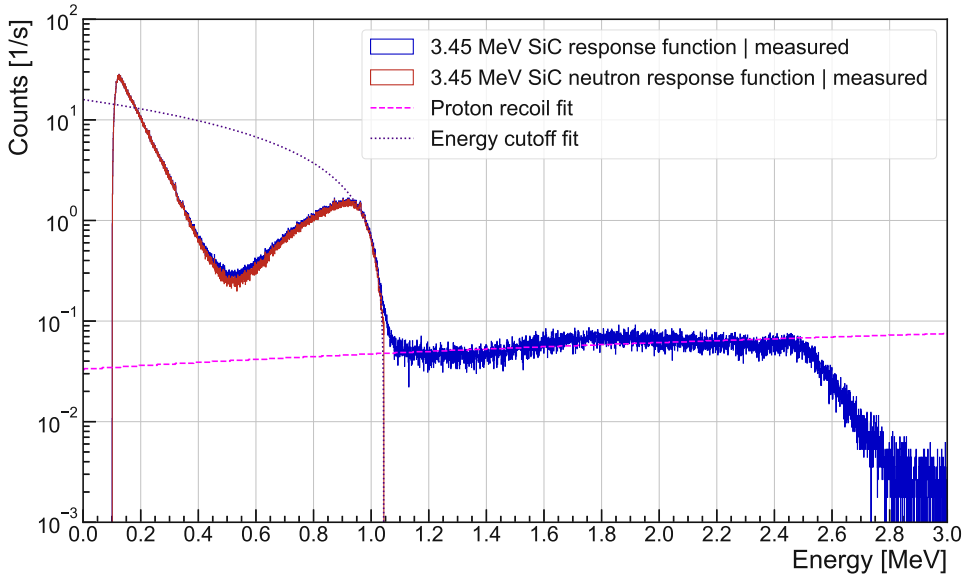

Figure 4.7: The measured SiC neutron response function with a linear proton recoil and maximum cut-off energy fit for the 3.45 MeV SiC measurement.

The highest deposited energy in the raw data is at around 2.70 MeV, confirming that recoil protons with kinetic energies above that cannot deposit their full energy inside the SiC detector. Additionally a non linear proton recoil energy distribution can be seen. This is due to the partial energy deposition, leading to a convoluted landau distribution. A comparison between the measured neutron response function and the GEANT4 simulation using the Demokritos neutron energy distribution convoluted with Gaussian noise with a standard deviation of 35 keV is shown in the top plot of figure 4.8. The bottom plot shows the relative difference

Die approbierte gedruckte Originalversion dieser Diplomarbeit ist an der TU Wien Bibliothek verfügbar
The approved original version of this thesis is available in print at TU Wien Bibliothek.

between the measurement result and the simulation.

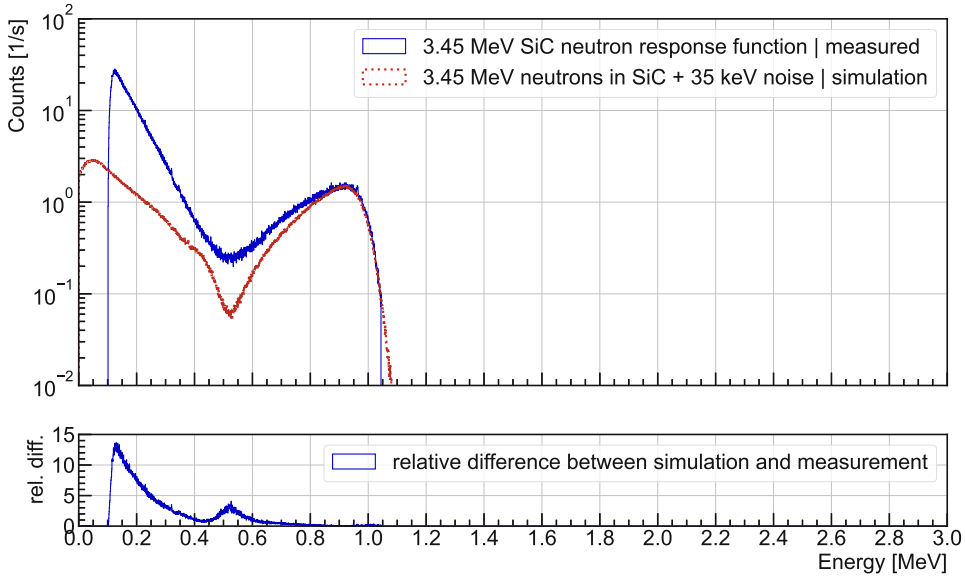

Figure 4.8: Comparison between the SiC neutron response function at 3.45 MeV and the GEANT4 simulation.

By comparing the simulation and the measured neutron response function, two domains can be identified, separated by the threshold located at the valley of the angular distribution. The threshold is determined to be at 0.534 MeV. Measurement and simulation almost perfectly agree at the cut-off energy, but deviate above the threshold energy. Below the threshold the ^{28}Si cut-off can be seen in the simulation, which is absent in the measurement data. Below the ^{28}Si cut-off the strong deviation can be best explained by the strong γ-background.Figure 4.9 shows the measured SiC neutron response function illustrating the two domains.

The number of identifiable neutrons above the threshold is 748 859 and the number of counts below the threshold is 4 456 436, accounting for a combination of neutrons and γ. This leads to 14.4 % of counts being identifiable neutrons. Comparing Γ_{SiC} to Γ_{BF_3}, the factor $\epsilon_{SiC_{3.45}}$ was determined to be 0.532 ± 0.005 identifiable neutron counts per BF_3 count, assuming the proton recoil number to be in the range of ± 10 % of the fit.

Using the integrated current measurement, the number of identifiable neutrons per proton was calculated to be $(3.5 \pm 1.1) \times 10^{-11}$. To obtain the interaction

Die approbierte gedruckte Originalversion dieser Diplomarbeit ist an der TU Wien Bibliothek verfügbar
The approved original version of this thesis is available in print at TU Wien Bibliothek.

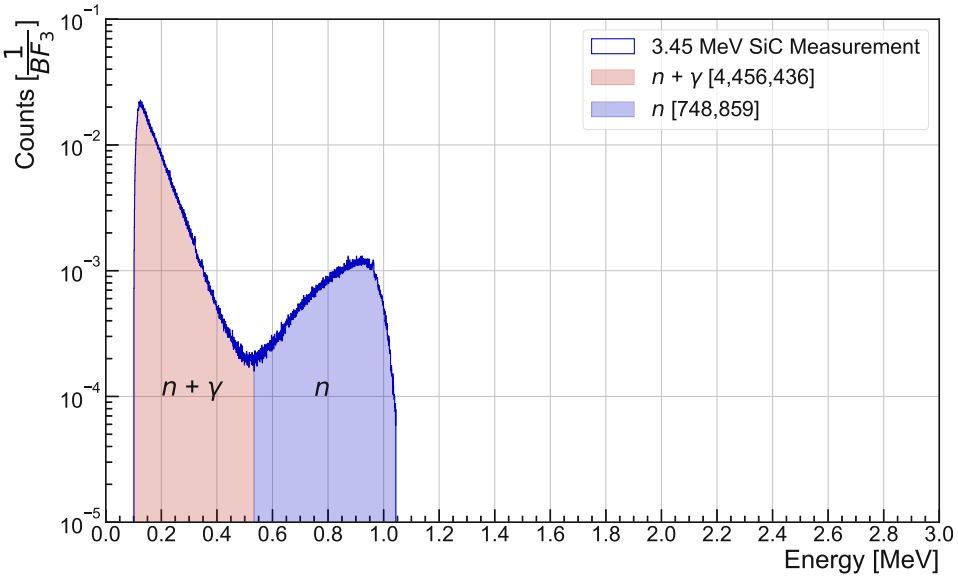

Figure 4.9: The SiC measured neutron response function to 3.45 MeV neutrons, normalised to the BF_3 reference detector counts, illustrating the two different domains.

probability predicted by the GEANT4 simulation (0.141 %), the conversion from protons to neutrons should be 2.48×10^{-8} n/p in the ^{3}H target.

4.4 3.95 MeV SiC response function

The SiC detector response function at a neutron energy of 3.95 MeV normalised to the acquisition time is shown in figure 4.10 with its full 13-bit resolution. The trigger was set to 100.6 keV for the measurement. To deduct the correct neutron response function a linear fit is used to remove the proton recoils coming from the detector PCB structure. To remove any higher energy entries, a linear fit to the maximum recoil cut-off energy slope was used. Using both fits, the neutron response function can be obtained. In the energy range of the neutron response function, 69 830 ± 10 % counts were removed due to the proton fit, accounting for the majority of the statistical neutron count error.

The highest deposited energy in the raw data is at around 2.70 MeV, confirming that recoil protons with kinetic energies above that cannot deposit their full energy inside the SiC detector. Additionally a non linear proton recoil energy distribution can be seen. This is due to the partial energy deposition, leading to a

Die approbierte gedruckte Originalversion dieser Diplomarbeit ist an der TU Wien Bibliothek verfügbar
The approved original version of this thesis is available in print at TU Wien Bibliothek.

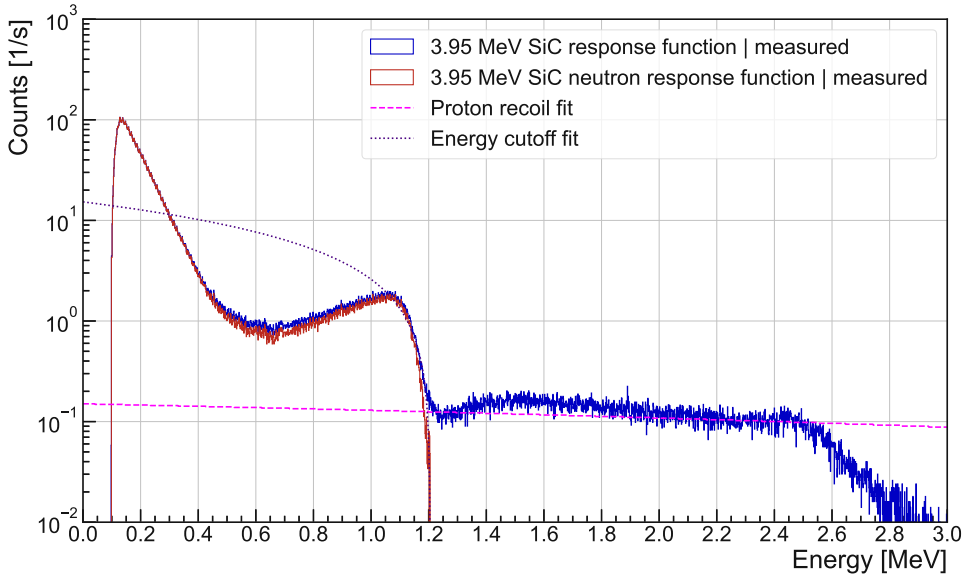

Figure 4.10: The measured SiC neutron response function with a linear proton recoil and maximum cut-off energy fit for the 3.95 MeV SiC measurement.

convoluted landau distribution. A comparison between the measured neutron response function and the GEANT4 simulation using the Demokritos neutron energy distribution convoluted with Gaussian noise with a standard deviation of 35 keV is shown in the top plot of figure 4.11. The bottom plot shows the relative difference between the measurement result and the simulation.

The valley at 0.637 MeV separates the two domains. Measurement and simulation almost perfectly agree from the threshold up to the cut-off energy. Below the threshold the ^{28}Si cut-off can be seen in the simulation, which is absent in the measurement data. Below the ^{28}Si cut-off the strong deviation can be best explained by the strong γ-background.Figure 4.12 shows the measured SiC neutron response function illustrating the two domains.

The number of identifiable neutrons above the threshold is 245 510 and the number of counts below the threshold is 4 186 431, accounting for a combination of neutrons and γ. This leads to 5.5 % of counts being identifiable neutrons. Comparing Γ_{SiC} to Γ_{BF_3}, the factor $\epsilon_{SiC_{3.95}}$ was determined to be 0.222 ± 0.006 identifiable neutron counts per BF_3 count, assuming the proton recoil number to be in the range of ± 10 % of the fit.

Using the integrated current measurement, the number of identifiable neutrons

Die approbierte gedruckte Originalversion dieser Diplomarbeit ist an der TU Wien Bibliothek verfügbar
The approved original version of this thesis is available in print at TU Wien Bibliothek.

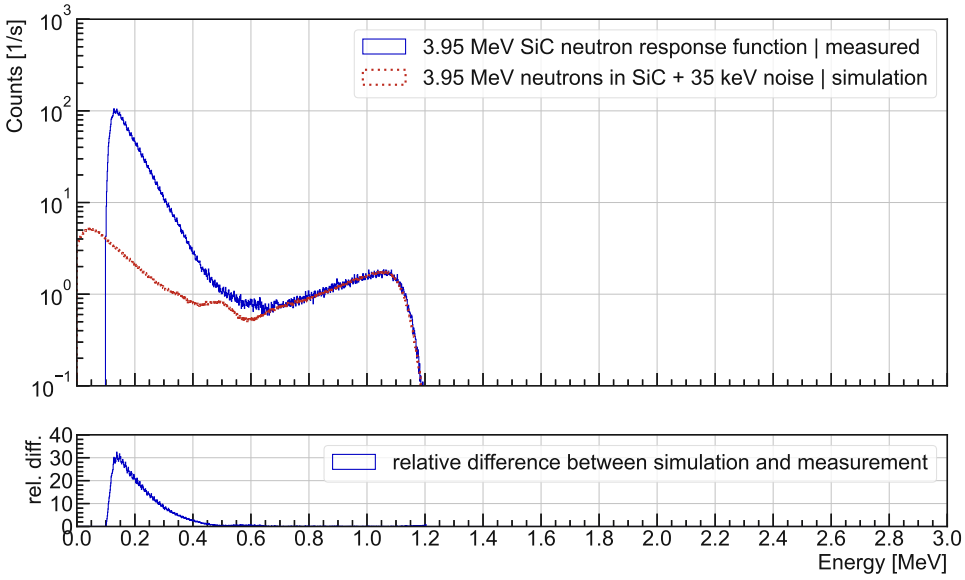

Figure 4.11: Comparison between the SiC neutron response function at 3.95 MeV and the GEANT4 simulation.

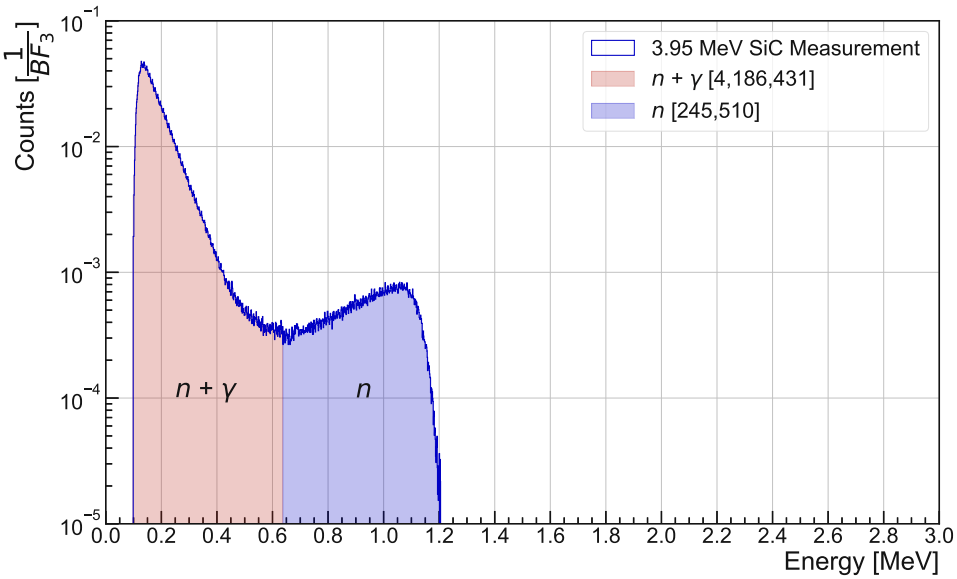

Figure 4.12: The SiC measured neutron response function to 3.95 MeV neutrons, normalised to the BF_3 reference detector counts, illustrating the two different domains.

Die approbierte gedruckte Originalversion dieser Diplomarbeit ist an der TU Wien Bibliothek verfügbar
The approved original version of this thesis is available in print at TU Wien Bibliothek.

per proton was calculated to be $(2.3 \pm 0.7) \times 10^{-11}$. To obtain the interaction probability predicted by the GEANT4 simulation (0.122 %), the conversion from protons to neutrons should be 1.83×10^{-8} n/p in the ^{3}H target.

4.5 SiC neutron response function comparison

The previous chapter discussed the SiC measured neutron response functions at four different neutron energies. The detector response is comparable to the sCVD detector response but some notable differences are evident. The measurement agrees with the simulation at each neutron energy at the ^{12}C cut-off but deviates from it above the respective threshold. In contrast to that, the sCVD deviations were lower above their respective thresholds. In addition, the ^{28}Si cut-off is below the threshold at all neutron energies, making a distinction between neutron and γ counts impossible. Using a threshold at all, which will be necessary for every measurement, therefore reduces the neutron sensitivity by the percentage of silicon in the SiC detector. This is worsened by the γ sensitivity of silicon compared to carbon, which shifts the energy distribution of the γ-background to higher energies and also increases their count percentage, reducing the percentage of identifiable neutron counts. This could be a reason why the ^{28}Si cut-off is not visible in the measured neutron response function. A further factor could be that the statistics are too low, such that the ^{28}Si cut-off is obscured by the high γ background.

Figures 4.13 shows the direct comparison of all measured SiC neutron response functions, normalised to their respective BF_3 count rate.

In contrast to the sCVD neutron response functions, the γ-background energy distribution increases linearly with neutron energy instead of stabilising. Using the identifiable neutron counts above their respective thresholds, the conversion factor ϵ_{SiC} with their uncertainties, mainly due to the proton recoil fit, are shown in figure 4.14. The ^{12}C cross-section, normalised to $\epsilon_{SiC_{2.45}}$, is shown as comparison.

It is assumed that the BF_3 detector response is constant for all neutron energies, as it used a neutron moderator. Although a SiC detector is used, the measured neutron response function is best compared to the ^{12}C cross section since the maximum ^{28}Si cut-off energy is at lower energies than the threshold. The deviation from the theoretical cross-section is explained by the γ-background, resulting in a shift of the threshold and the number of counts above it.

As additional comparison, figure 4.15 shows the comparison factor Γ_{SiC} / Γ_{proton}. The normalised ^{12}C cross-section is added as comparison.

Die approbierte gedruckte Originalversion dieser Diplomarbeit ist an der TU Wien Bibliothek verfügbar
The approved original version of this thesis is available in print at TU Wien Bibliothek.
TU Bibliothek Your knowledge hub WIEN

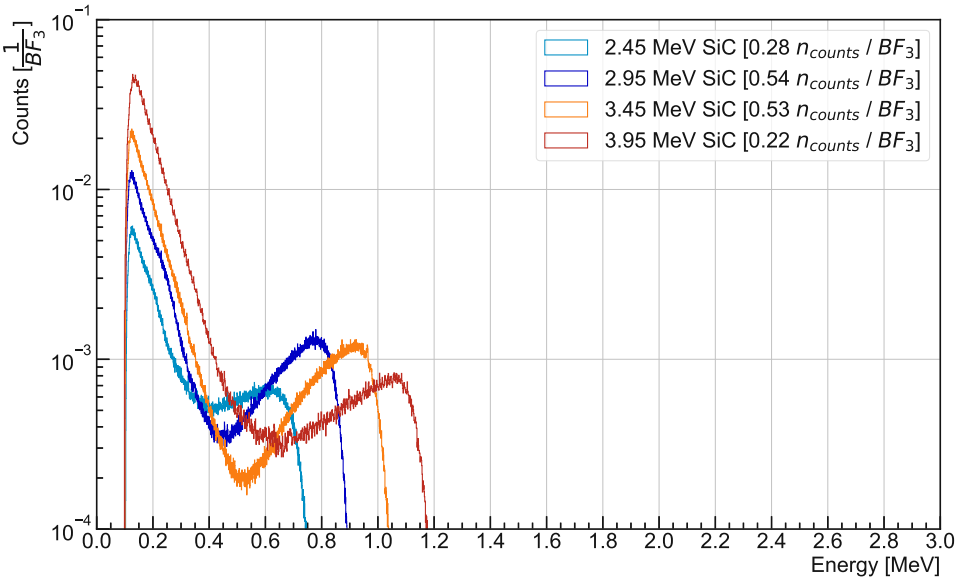

Figure 4.13: The SiC neutron response function at the four neutron energies investigated, normalised to the respective BF_3 counts.

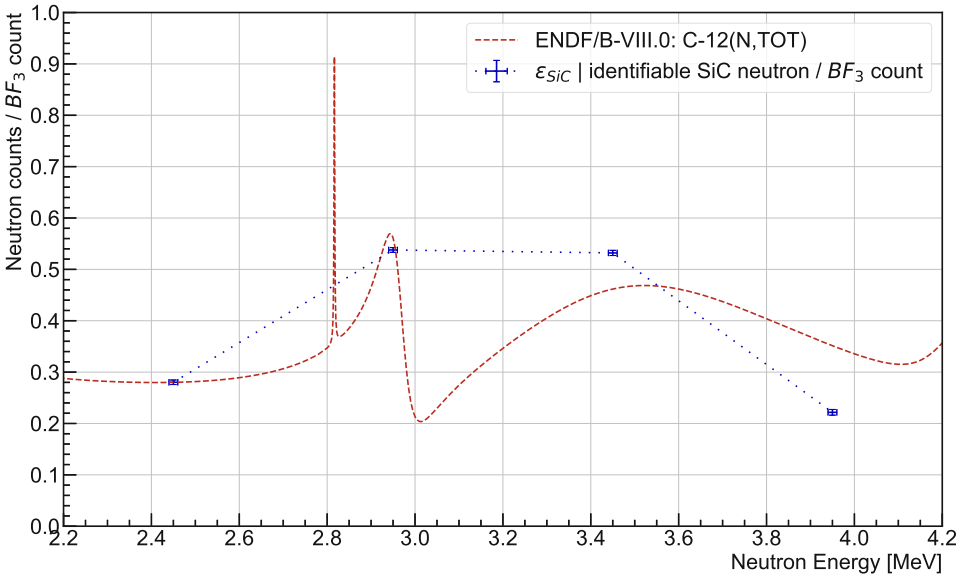

Figure 4.14: The identifiable neutron counts per BF_3 count ϵ_{SiC} for all four neutron energies. The normalised cross-section for ^{12}C is shown as comparison [25].

Die approbierte gedruckte Originalversion dieser Diplomarbeit ist an der TU Wien Bibliothek verfügbar
The approved original version of this thesis is available in print at TU Wien Bibliothek.

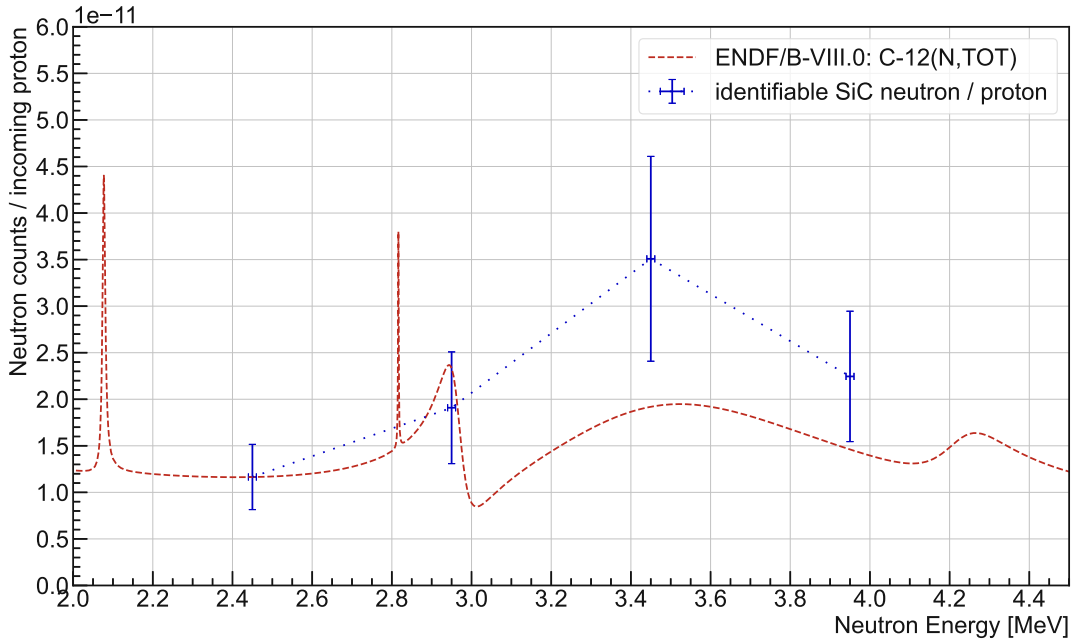

Figure 4.15: Number of identifiable SiC neutron counts per proton using the current integrator. The normalised ^{12}C cross-section is shown as comparison

The current integrator agrees very well with the cross-section at neutron energies of 2.45 MeV and 2.95 MeV. The current integrator uncertainty of ±30 % combined with the uncertain proton/neutron conversion percentage in the target prevents a comprehensive comparison between the different SiC neutron response function at the investigated neutron energies. All key factors for the SiC detector are summarised in table 4.1.

$E_{neutron}$ [MeV]	$N_{neutrons}$ [%]	ϵ_{SiC}	Γ_{SiC} / Γ_{proton}
2.45 MeV	23.1 %	0.280 ± 0.004	$(1.2 \pm 0.4) \times 10^{-11}$
2.95 MeV	21.9 %	0.538 ± 0.005	$(1.9 \pm 0.6) \times 10^{-11}$
3.45 MeV	14.4 %	0.532 ± 0.005	$(3.5 \pm 1.1) \times 10^{-11}$
3.95 MeV	5.5 %	0.222 ± 0.006	$(2.3 \pm 0.7) \times 10^{-11}$

Table 4.1: Key results from the measured SiC neutron response functions including the percentage of all counts being identifiable neutrons, the ϵ_{SiC}-factor and the conversion from protons to identifiable neutrons.

Die approbierte gedruckte Originalversion dieser Diplomarbeit ist an der TU Wien Bibliothek verfügbar
The approved original version of this thesis is available in print at TU Wien Bibliothek.

Chapter 5

Silicon detector response

The following chapter presents the measured Si detector response functions. As it will be shown, there are multiple challenges when using a Si detector to detect neutrons. Due to the lower ionisation energy compared to sCVD and SiC, the detector response is greater and therefore the CxL amplifier pulse reached its linear limit at $\pm 1\,\mathrm{V}$. All recorded counts above are still valid but cannot be converted to energy with a constant conversion factor. In addition, the theoretical isotropic angular elastic neutron cross section, also shown in the GEANT4 simulation, in combination with the Demokritos neutron spectrum convoluted with Gaussian noise with a standard deviation of 45 keV, shows no distinct feature. This, combined with the γ-background already visible in the sCVD and SiC response functions and the proton recoils from the PCB structure, prevents a clear distinction between neutron and γ counts.

Due to previously mentioned reasons, the raw response function from the Si detector is shown in mV instead of MeV for all four neutron energies, normalised to the BF_3 counter using all Si counts, not only identifiable neutron counts as beforehand.

To show a relative comparison, the raw response function is converted to energy using a constant conversion factor which is $5\times$ the conversion factor for the sCVD detector, as the ionisation energy is $5\times$ smaller for the Si detector, to compare it with the simulated neutron response function. This does not take into account the non-linearity at higher energies and is only an approximation, as the conversion factor itself is only an approximation.

The Si detector has a nominal thickness of $50\,\mu\mathrm{m}$, same as the sCVD and SiC detector. But the exact depleted volume is not known, which hinders the use of the maximum counts to be set to the nominal neutron energy due to proton recoils.

Die approbierte gedruckte Originalversion dieser Diplomarbeit ist an der TU Wien Bibliothek verfügbar
The approved original version of this thesis is available in print at TU Wien Bibliothek.
TU Bibliothek Your knowledge hub WIEN

5.1 2.45 MeV Si response function

The Si detector response function at a neutron energy of 2.45 MeV normalised to the BF_3 counter, using all Si counts, is shown in figure 5.1.

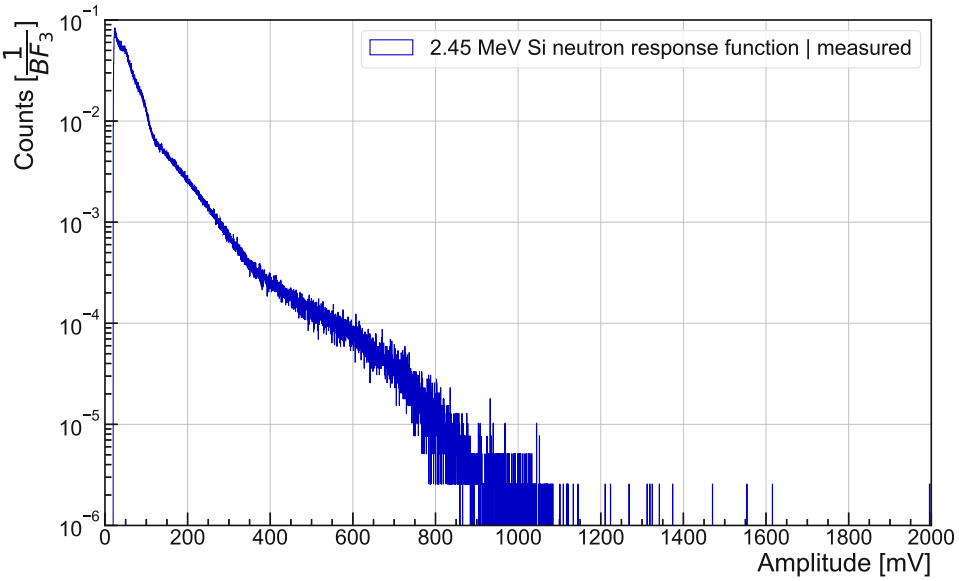

Figure 5.1: The measured Si response function in mV for the 2.45 MeV Si measurement.

The Si response function lacks any distinct features which could be used to discriminate between neutrons, protons or γ counts. At the given neutron energy, 1.83×10^{-3} % of all counts are outside the linear regime. The comparison with the simulation of the pure neutron response function is shown in figure 5.2. The y-axis uses arbitrary units, as it should only be used to compare the shape of the response function.

The simulation uses the Demokritos neutron energy distribution and is convoluted with Gaussian noise with a standard deviation of 45 keV. Some similarity between the structure in the simulation and the measurement is visible at an energy of 0.18 MeV, but it is uncertain whether this is an artefact or a genuine similarity. Due to the shape of the response function, no measured neutron response function could be obtained and therefore a comparison is not possible. The count rate for the Si detector was 13 242.5 counts/s, including the neutron counts and background from the produced γ and protons. It becomes evident that a Si detector is not capable of reliably measuring the neutron flux, assuming a similar γ or recoil proton background.

Die approbierte gedruckte Originalversion dieser Diplomarbeit ist an der TU Wien Bibliothek verfügbar
The approved original version of this thesis is available in print at TU Wien Bibliothek.

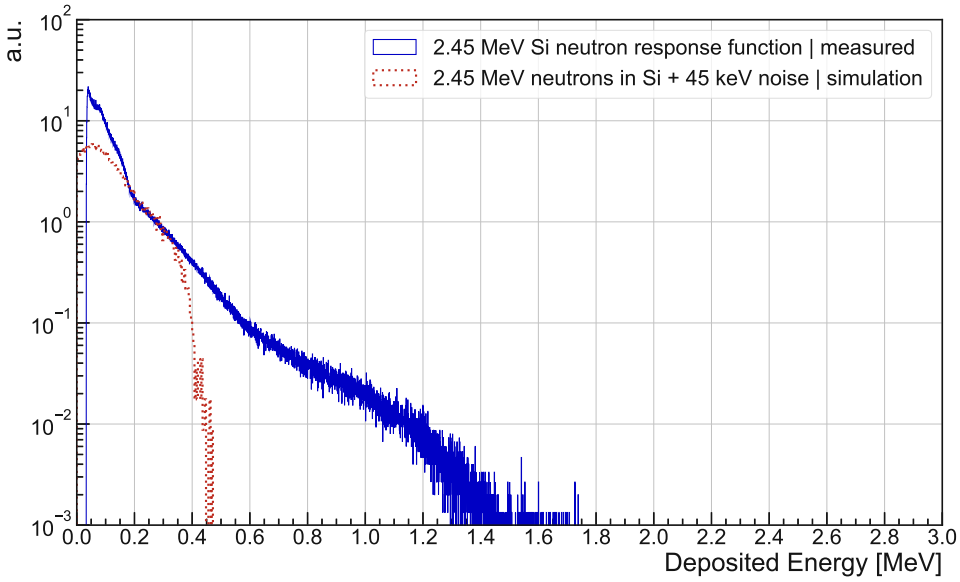

Figure 5.2: Comparison between the Si neutron response function at 2.45 MeV and the GEANT4 simulation.

5.2 2.95 MeV Si response function

The Si detector response function at a neutron energy of 2.95 MeV normalised to the BF_3 counter, using all Si counts, is shown in figure 5.3.

The Si response function lacks any distinct features which could be used to discriminate between neutrons, protons or γ counts. At the given neutron energy, 1.80×10^{-2} % of all counts are outside the linear regime. The comparison with the simulation of the pure neutron response function is shown in figure 5.4. The y-axis uses arbitrary units, as it should only be used to compare the shape of the response function.

The simulation uses the Demokritos neutron energy distribution and is convoluted with Gaussian noise with a standard deviation of 45 keV. At the given neutron energy no similarities between the measurement and the GEANT4 simulations are evident, making a conversion to energy using a distinct response function feature impossible. Furthermore, no measured neutron response function can be obtained. The count rate for the Si detector was 13 050.1 counts/s, including all counts from neutrons, protons and the γ-background. The Si detector cannot be used to measure the neutron flux reliably at this neutron energy without performing detailed simulations of the expected background.

Die approbierte gedruckte Originalversion dieser Diplomarbeit ist an der TU Wien Bibliothek verfügbar
The approved original version of this thesis is available in print at TU Wien Bibliothek.

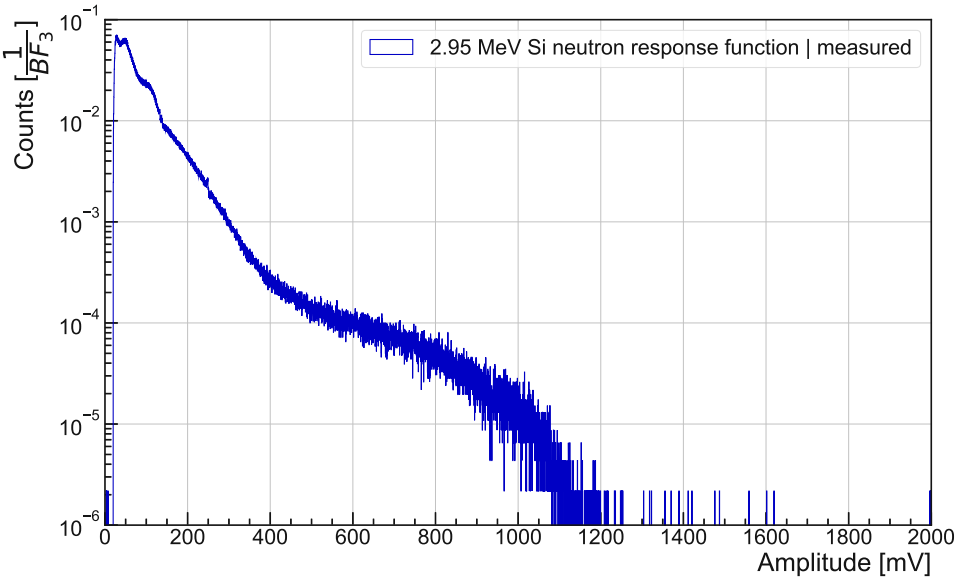

Figure 5.3: The measured Si response function in mV for the 2.95 MeV Si measurement.

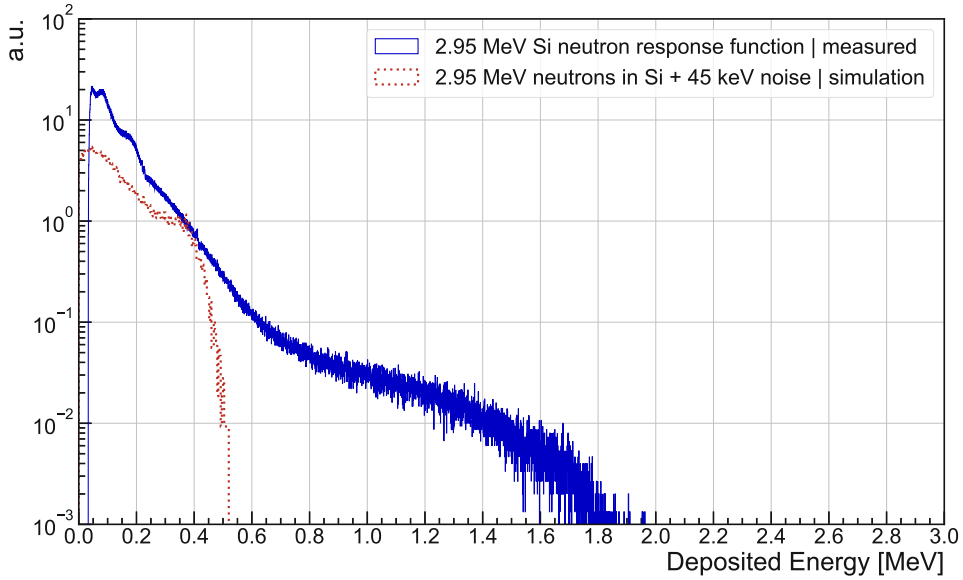

Figure 5.4: Comparison between the Si neutron response function at 2.95 MeV and the GEANT4 simulation.

Die approbierte gedruckte Originalversion dieser Diplomarbeit ist an der TU Wien Bibliothek verfügbar
The approved original version of this thesis is available in print at TU Wien Bibliothek.

5.3 3.45 MeV Si response function

The Si detector response function at a neutron energy of 3.45 MeV normalised to the BF_3 counter, using all Si counts, is shown in figure 5.5.

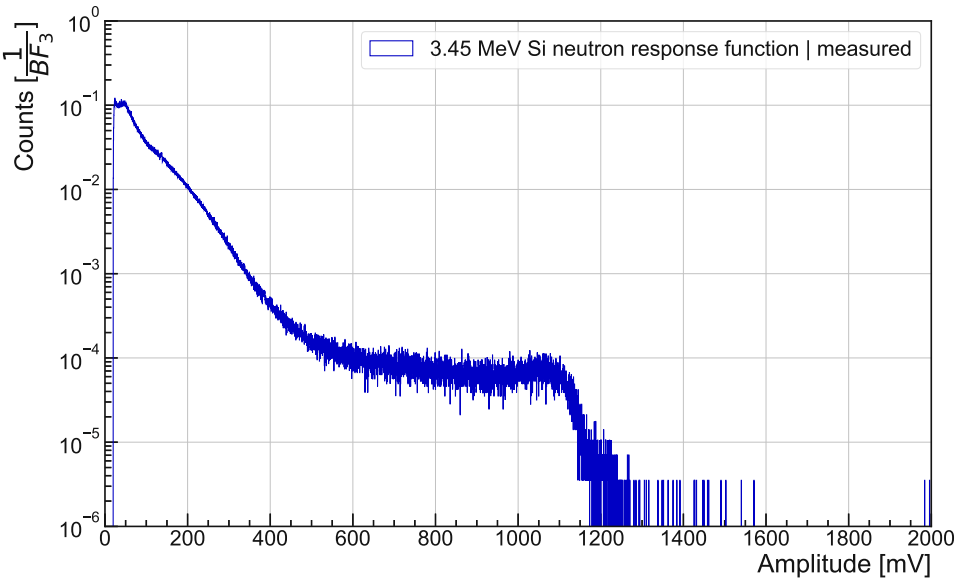

Figure 5.5: The measured Si response function in mV for the 3.45 MeV Si measurement.

The Si response function lacks any distinct features which could be used to discriminate between neutrons, protons or γ counts. At the given neutron energy 0.11 % of all counts are outside the linear regime. The comparison with the simulation of the pure neutron response function is shown in figure 5.6. The y-axis uses arbitrary units, as it should only be used to compare the shape of the response function.

The simulation uses the Demokritos neutron energy distribution and is convoluted with Gaussian noise with a standard deviation of 45 keV. At the given neutron energy no similarities between the measurement and the GEANT4 simulations are evident, making a conversion to energy using a distinct response function feature impossible. Furthermore, no neutron response function can be obtained. The count rate for the Si detector was 37 132.4 counts/s, including all counts from neutrons, protons and the γ-background.

Die approbierte gedruckte Originalversion dieser Diplomarbeit ist an der TU Wien Bibliothek verfügbar
The approved original version of this thesis is available in print at TU Wien Bibliothek.
TU Bibliothek Your knowledge hub WIEN

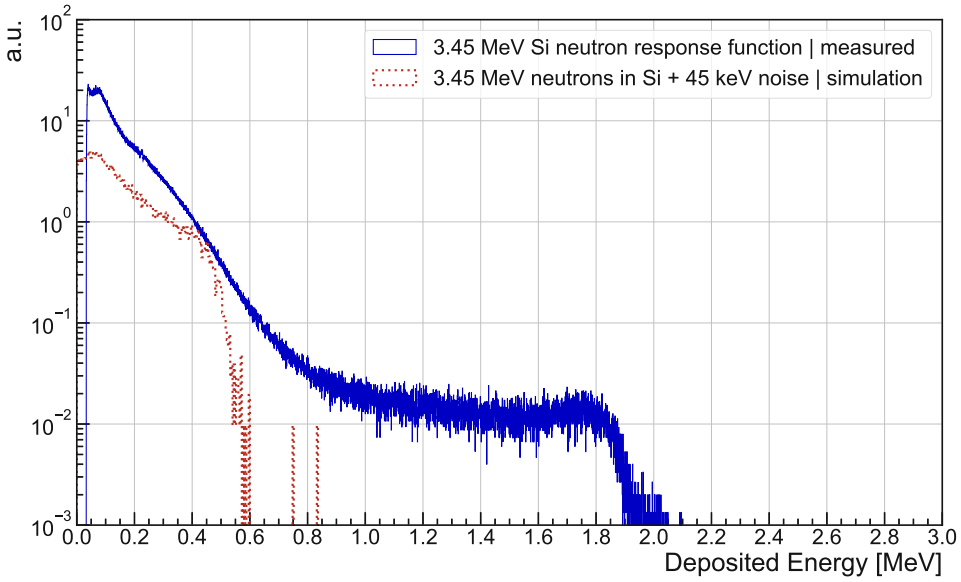

Figure 5.6: Comparison between the Si neutron response function at 3.45 MeV and the GEANT4 simulation.

The apparent peak above 1000 mV or around 1.8 MeV is most likely an illusion caused by the non-linearity of the amplifier and pile-up events. A time window of 3 µs was used for the measurement, which means that as soon as a trigger event occurs, the maximum value in the time window is used for the spectrum. This would result in a maximum possible count rate of 333 kHz. The count rate during the measurement was well below that, but as it is an averaged value, the time between interactions with the Si detector may be below the time window. If such an event occurs, only the higher pulse is counted, which might have a significant offset due to convolution with the previous pulse. Two pile-up events from the Si detector measurements are shown in figure 5.7.

The first example (blue line) shows a separation between the pulses, but as both occur in the time window, only the second peak is counted, thereby changing the count rate and also the measured response function, as the offset due to the first pulse is not taken into account. In the second example (red dashed line), only one long pulse is visible. But since the CxL pulse has always the same FWHM, this must be due to the convolution of at least two pulses. This leads to an unusable measured response function in the worst case scenario. For the presented 3.45 MeV neutron measurement the pile-up events are likely not of relevance, as they affect a fraction of all counts.

Die approbierte gedruckte Originalversion dieser Diplomarbeit ist an der TU Wien Bibliothek verfügbar
The approved original version of this thesis is available in print at TU Wien Bibliothek.

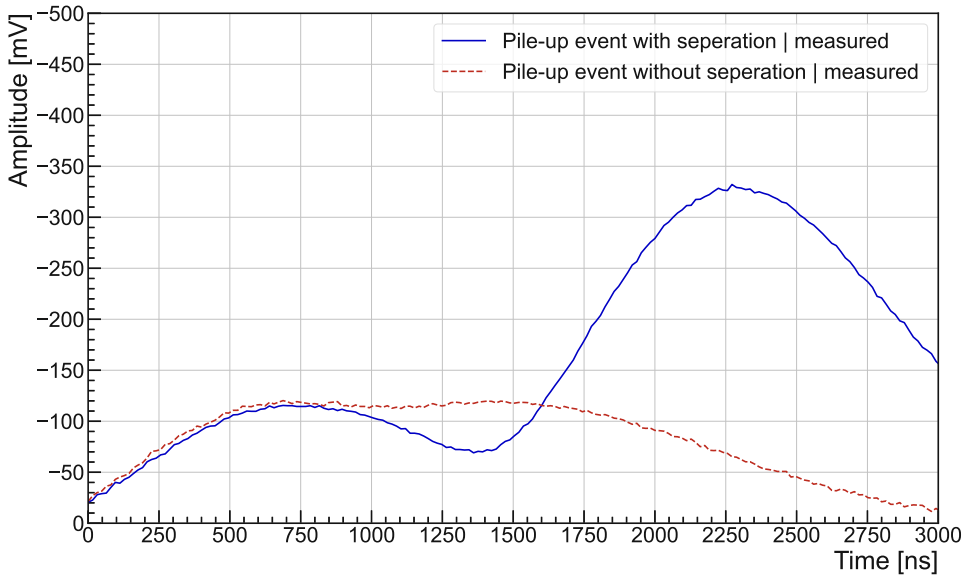

Figure 5.7: Pile-up events during the Si detector measurements. The first event (blue line) still shows two separate peaks, whereas the second event (red dashed line) shows no separation of the pulses.

5.4 3.95 MeV Si response function

The Si detector response function at a neutron energy of 3.95 MeV normalised to the BF_3 counter, using all Si counts, is shown in figure 5.8.

The Si response function lacks any distinct features which could be used to discriminate between neutrons, protons or γ counts. At the given neutron energy, 0.13 % of all counts are outside the linear regime. The comparison with the simulation of the pure neutron response function is shown in figure 5.9. The y-axis uses arbitrary units, as it should only be used to compare the shape of the response function.

The simulation uses the Demokritos neutron energy distribution and is convoluted with Gaussian noise with a standard deviation of 45 keV. At the given neutron energy no similarities between the measurement and the GEANT4 simulations are evident, making a conversion to energy using a distinct response function feature impossible. Furthermore, no neutron response function can be obtained. The count rate for the Si detector was 71 552.8 counts/s, including all counts from neutrons, protons and the γ-background.

Die approbierte gedruckte Originalversion dieser Diplomarbeit ist an der TU Wien Bibliothek verfügbar
The approved original version of this thesis is available in print at TU Wien Bibliothek.

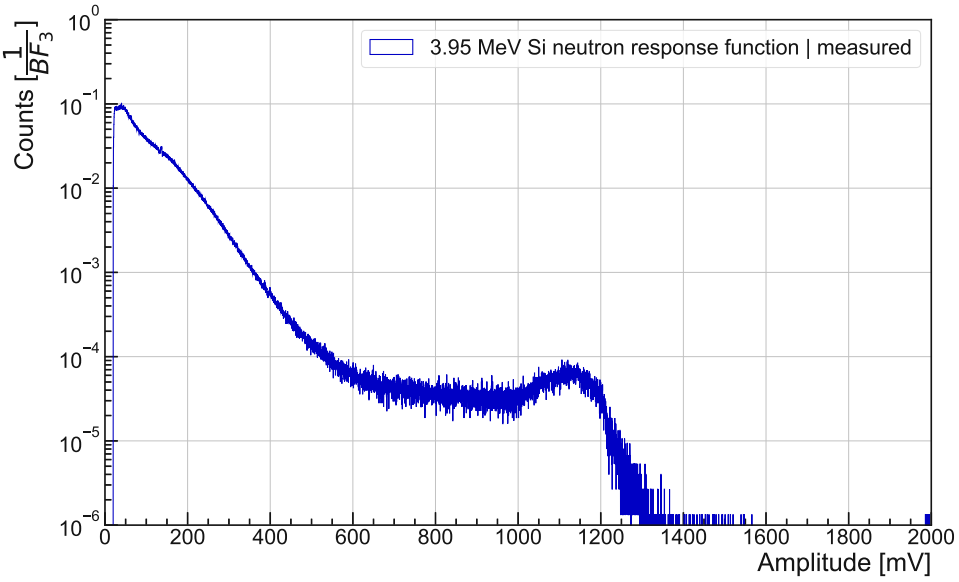

Figure 5.8: The measured Si response function in mV for the 3.95 MeV Si measurement.

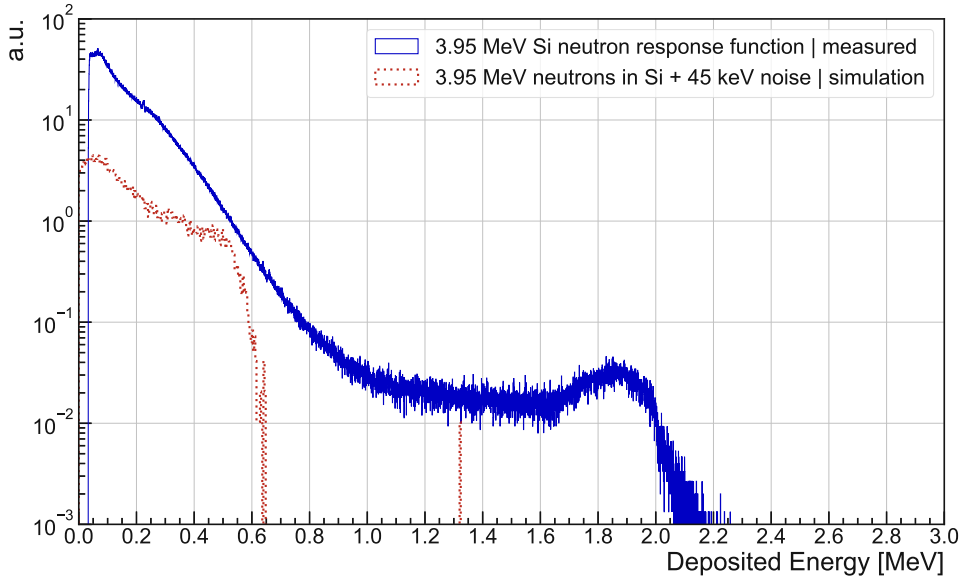

Figure 5.9: Comparison between the Si neutron response function at 3.95 MeV and the GEANT4 simulation.

Die approbierte gedruckte Originalversion dieser Diplomarbeit ist an der TU Wien Bibliothek verfügbar
The approved original version of this thesis is available in print at TU Wien Bibliothek.

The apparent peak above 1000 mV or around 1.9 MeV is most likely an illusion caused by the non-linearity of the amplifier and pile-up event. Due to the high count rate, pile-up events are more likely and therefore could be the main reason of the peak. Combined with the non-linearity and recorded amplitudes of up to 1300 mV, many counts would be at even higher amplitudes but are shifted down due to the non-linearity. This combination explains the apparent peak.

5.5 Si neutron response function comparison

The previous chapter discussed the measured Si response functions at four different neutron energies. Due to the response function shape and the absence of features associated with neutron interactions, no neutron response functions could be obtained. Therefore, a Si detector is not suitable for measuring neutron energies or fluxes. This would necessitate a thorough background analysis using measurements and simulations. Such an analysis could enable the derivation of an effective neutron response from the actual measurement. This would need to be done at each Si detector location, as slight changes in the γ-background would lead to a significantly altered measured response function due to the high sensitivity to γ.

Figure 5.10 shows all four recorded Si response functions in mV normalised to the BF_3 counter using all recorded counts.

As the number of incoming neutrons is not expected to deviate significantly for the Si detector compared to the sCVD or SiC detector, the increase in count rate can best be explained by an increased γ-background. When comparing the four response functions the low energy regions look similar, pointing to a stable γ-background for the 2.45 MeV and 2.95 MeV as well as for the 3.45 MeV and 3.95 MeV measurements. As previously discussed, the apparent peak at 3.45 MeV and 3.95 MeV are most likely a result of the CxL non-linearity above 1000 mV in combination with pile-up events.

Table 5.1 compares the count rate, Γ_{proton} obtained using the current integrator, Γ_{BF_3} and an effective ϵ_{Si} using all counts, for all four energies.

Combining the information about the ^{28}Si cross section shown in figure 1.4, which shows a relatively stable cross section for the four neutron energies, in combination with the stable number of protons and the systematic change in BF_3 counts, indicates a changing γ-background as the main contributor to the high count rate for the Si detector. Irrespective of the reason, the Si detector must be excluded as a possibility for reliable neutron flux and energy measurements.

Die approbierte gedruckte Originalversion dieser Diplomarbeit ist an der TU Wien Bibliothek verfügbar
The approved original version of this thesis is available in print at TU Wien Bibliothek.

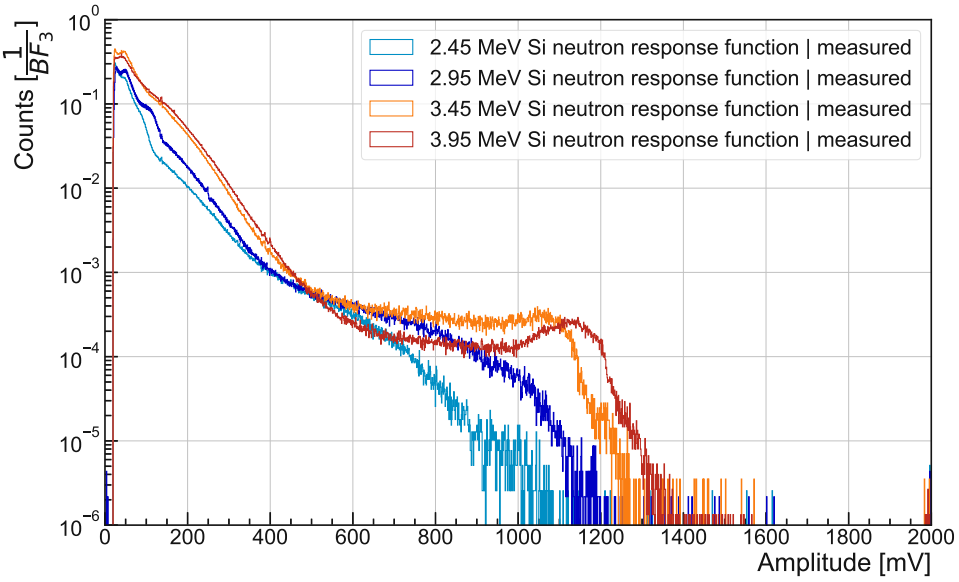

Figure 5.10: The Si response function at the four neutron energies investigated, normalised to the respective BF3 counts.

$E_{neutron}$ [MeV]	Si counts/s	Γ_{proton}	Γ_{BF_3}	ϵ_{Si}
2.45 MeV	13 242.5	2.01×10^{13}	873.6	15.16
2.95 MeV	13 050.1	1.97×10^{13}	670.9	19.45
3.45 MeV	37 132.4	1.72×10^{13}	1043.1	35.60
3.95 MeV	71 552.8	2.12×10^{13}	2065.5	34.64

Table 5.1: Key results from the measured Si response functions including the count rate, Γ_{proton}, Γ_{BF_3} and ϵ_{Si}.

The γ sensitivity and the absence of any neutron feature in the response function prevents a distinction between neutrons and background events.

Die approbierte gedruckte Originalversion dieser Diplomarbeit ist an der TU Wien Bibliothek verfügbar
The approved original version of this thesis is available in print at TU Wien Bibliothek.

Chapter 6

Detector response function comparison

The previous chapters presented and discussed the results for the sCVD, SiC and Si detector in great detail on its own. The following chapter focuses on the comparison between the detectors to determine their capabilities for future neutron applications. As no measured neutron response function could be obtained from the Si detector due to its detector response function shape and γ sensitivity, it is excluded from the following comparisons for the most parts.

The comparison will be focusing on the neutron response function shape for the sCVD and SiC detector, as well as the normalisation to the BF_3 counter and the current integrator. Due to the different conversion factor from amplitude in mV to energy in MeV for the two detectors, the bin width of the measured neutron response function histogram is slightly different. To allow for a valid comparison, all presented measured response functions in this chapter are normalised to the BF_3 counter and the bin width. This allows for an accurate comparison of the measured neutron response functions and their respective ϵ-factors. Using the ϵ-factors, the active volume thickness of the SiC detector is determined.

The chapter concludes with a sub-chapter discussing an unanticipated parasitic interaction in the data coming from the $^{14}N(p,\alpha)^{11}B$ reaction in air. The resulting α-particle was visible in the data for the sCVD and SiC detector but is most pronounced in the SiC detector data at 3.45 MeV and 3.95 MeV since proton recoils could not obscure it.

Die approbierte gedruckte Originalversion dieser Diplomarbeit ist an der TU Wien Bibliothek verfügbar
The approved original version of this thesis is available in print at TU Wien Bibliothek.
TU Bibliothek Your knowledge hub WIEN

6.1 Comparison at 2.45 MeV

The measured neutron response function at a neutron energy of 2.45 MeV was used as a baseline for all measurements, meaning the noise level was determined by comparing it with GEANT4 simulation. The determined measured neutron response functions for the sCVD and SiC detector are compared in figure 6.1.

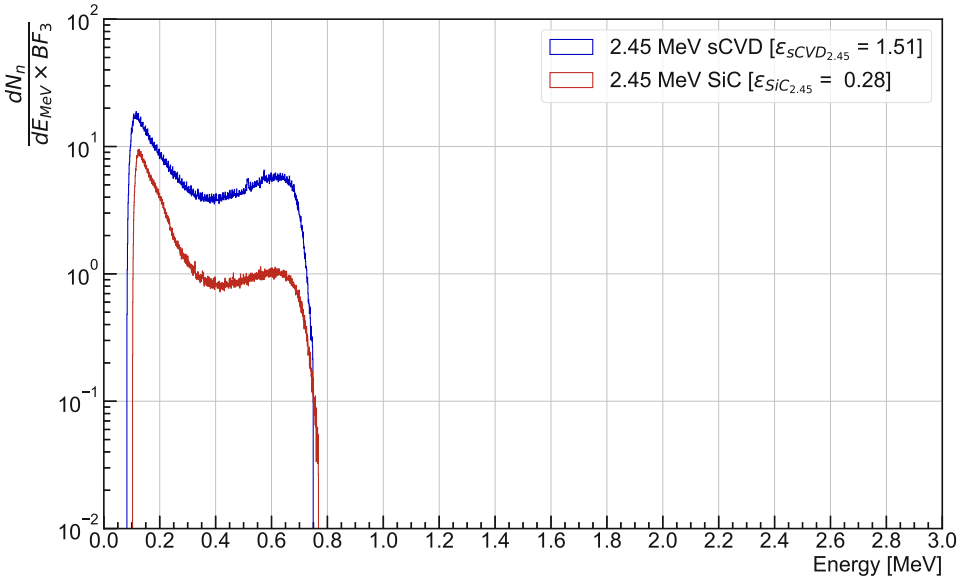

Figure 6.1: Comparison of the neutron response functions at 2.45 MeV for the sCVD and SiC detector.

The neutron response functions of both detectors are similar, as anticipated. The contribution of the 50 % ^{28}Si in the SiC detector and its cut-off are below the threshold for identifying the counts as neutron counts. This, coupled with the higher γ sensitivity results in a lower percentage of counts being above the threshold for the SiC detector, 23.1 %, compared to the sCVD detector, 38.2 %.

Using identifiable neutron counts above the threshold, $\epsilon_{sCVD_{2.45}} = 1.509 \pm 0.017$ and $\epsilon_{SiC_{2.45}} = 0.280 \pm 0.004$ were calculated. This leads to a 5.39 ± 0.10 times higher sensitivity for the sCVD detector to neutrons compared to the SiC detector.

6.2 Comparison at 2.95 MeV

The comparison for the neutron response functions at a neutron energy of 2.95 MeV between the sCVD and SiC detector is shown in figure 6.2.

Die approbierte gedruckte Originalversion dieser Diplomarbeit ist an der TU Wien Bibliothek verfügbar
The approved original version of this thesis is available in print at TU Wien Bibliothek.

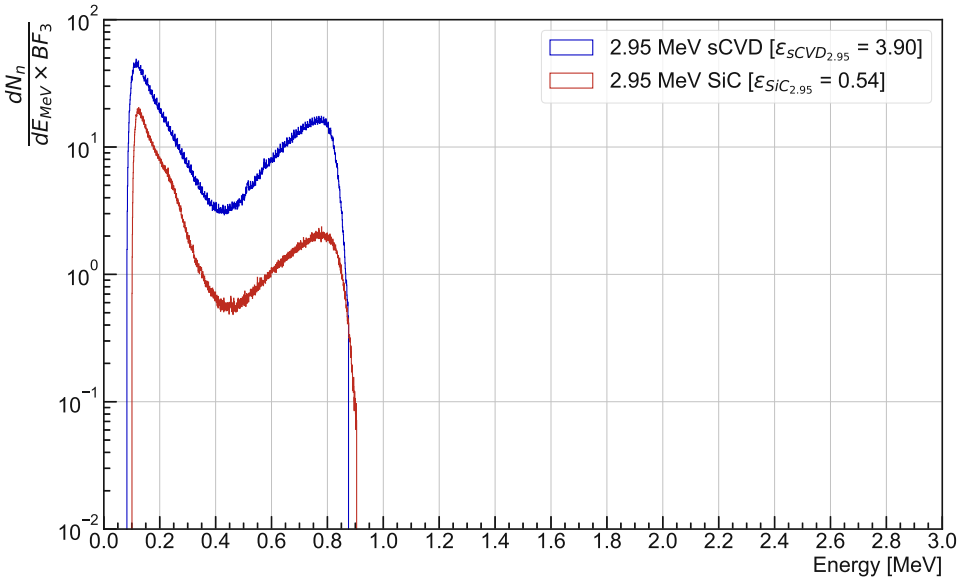

Figure 6.2: Comparison of the neutron response functions at 2.95 MeV for the sCVD and SiC detector.

The SiC measured neutron response function shows the same features as the sCVD measured neutron response function, as the counts from the ^{28}Si fraction are below the threshold and also covered by the γ-background. For the SiC detector 21.9 % of the counts are above the threshold, compared to 41.9 % for the sCVD detector.

Using identifiable neutron counts above the threshold, $\epsilon_{sCVD_{2.95}} = 3.904 \pm 0.026$ and $\epsilon_{SiC_{2.95}} = 0.538 \pm 0.005$ were calculated. This leads to a 7.26 ± 0.08 times higher sensitivity for the sCVD detector to neutrons compared to the SiC detector.

6.3 Comparison at 3.45 MeV

The comparison for the neutron response functions at a neutron energy of 3.45 MeV between the sCVD and SiC detector is shown in figure 6.3.

The SiC measured neutron response function shares the same features as the sCVD measured neutron response function, as the counts with the ^{28}Si fraction are below the threshold and also covered by the γ-background. For the SiC detector 14.4 % of the counts are above the threshold, compared to 28.9 % for the sCVD detector.

Die approbierte gedruckte Originalversion dieser Diplomarbeit ist an der TU Wien Bibliothek verfügbar
The approved original version of this thesis is available in print at TU Wien Bibliothek.

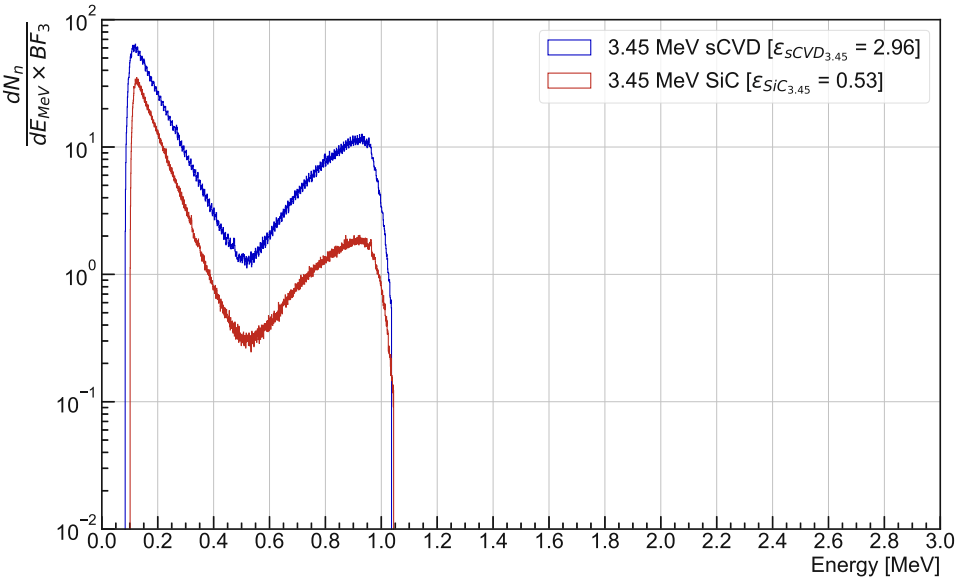

Figure 6.3: Comparison of the neutron response functions at 3.45 MeV for the sCVD and SiC detector.

Using identifiable neutron counts above the threshold, $\epsilon_{sCVD_{3.45}} = 2.962 \pm 0.021$ and $\epsilon_{SiC_{3.45}} = 0.532 \pm 0.005$ were calculated. This leads to a 5.57 ± 0.07 times higher sensitivity for the sCVD detector to neutrons compared to the SiC detector.

6.4 Comparison at 3.95 MeV

The comparison for the neutron response functions at a neutron energy of 3.95 MeV between the sCVD and SiC detector is shown in figure 6.4.

The SiC measured neutron response function shares the same features as the sCVD measured neutron response function, as the counts with the ^{28}Si fraction are below the threshold and also covered by the γ-background. For the SiC detector 5.5 % of the counts are above the threshold, compared to 13.9 % for the sCVD detector.

Using identifiable neutron counts above the threshold, $\epsilon_{sCVD_{3.95}} = 1.246 \pm 0.011$ and $\epsilon_{SiC_{3.95}} = 0.222 \pm 0.006$ were calculated. This leads to a 5.61 ± 0.16 times higher sensitivity for the sCVD detector to neutrons compared to the SiC detector.

Die approbierte gedruckte Originalversion dieser Diplomarbeit ist an der TU Wien Bibliothek verfügbar
The approved original version of this thesis is available in print at TU Wien Bibliothek.

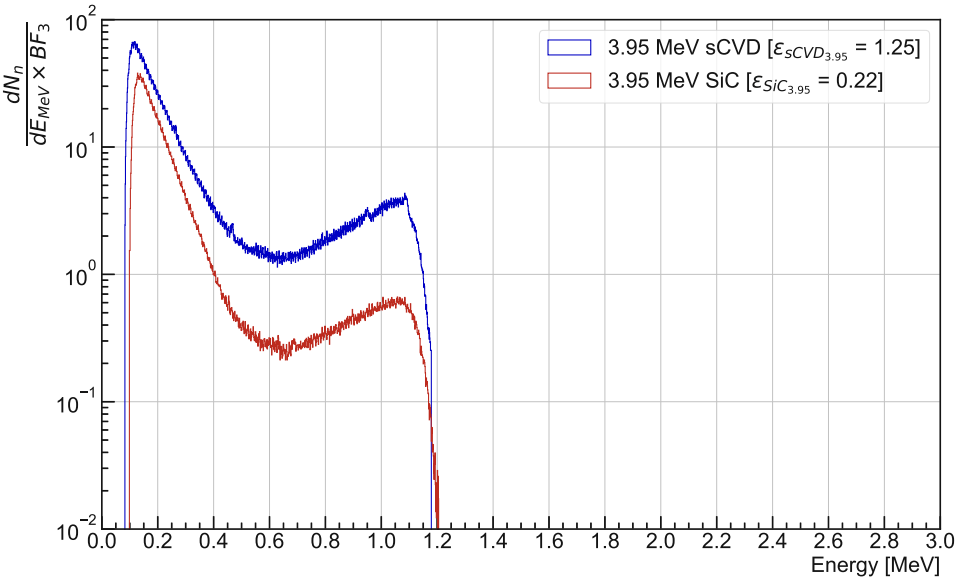

Figure 6.4: Comparison of the neutron response functions at 3.95 MeV for the sCVD and SiC detector.

6.5 ϵ_{sCVD} vs. ϵ_{SiC}

The comparison between sCVD and SiC detector is best done by using the BF_3 counter as a reference detector. Using the previous described methods, the ϵ-factors were calculated. Figure 6.5 shows the factor for the sCVD and SiC detector.

The ϵ-factor for sCVD is higher than for SiC at all neutron energies. The difference can be explained by a thinner active volume the SiC detector and the 50 % volume loss due to its ^{28}Si percentage. The sCVD detector therefore shows a more pronounced neutron response function, as the sensitivity to neutrons is higher while having a lower γ-background impact.

6.6 SiC thickness determination

The comparison of the epsilon factors in the previous section illustrates the higher neutron sensitivity for the sCVD detector compared to the SiC detector. This can be explained by the 50 % ^{28}Si which do not contribute and smaller sensor volume than anticipated. This indicates a lower active sensor thickness than the nominal thickness of the sensor. Figure 6.6 shows the calculated SiC sensor thickness when using the epsilon factors for both and a fixed thickness of 50 µm for the sCVD sensor as reference. This is done by dividing the sCVD thickness by the relative

Die approbierte gedruckte Originalversion dieser Diplomarbeit ist an der TU Wien Bibliothek verfügbar
The approved original version of this thesis is available in print at TU Wien Bibliothek.

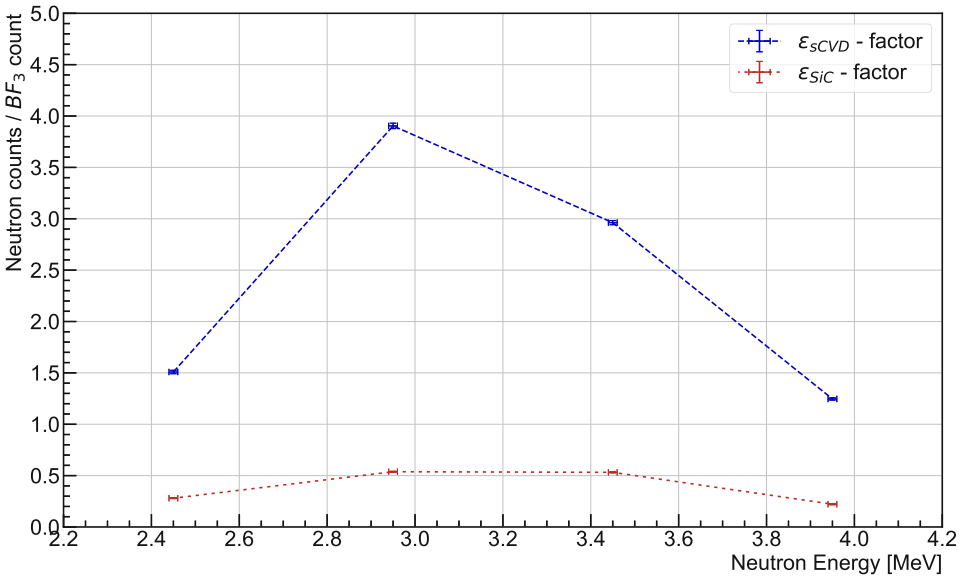

Figure 6.5: Comparison of the ratio of identified neutrons to BF_3 counts at all four investigated neutron energies for the sCVD (blue) and SiC (red) detector.

factor of ϵ_{sCVD} and ϵ_{SiC} and taking into account that only counts from the 50 % of the SiC detector is contributing.

The calculated thickness of the active SiC sensor volume is $(18.6 \pm 0.3)\,\mu m$ at 2.45 MeV, $(13.8 \pm 0.2)\,\mu m$ at 2.95 MeV, $(18.0 \pm 0.2)\,\mu m$ at 3.45 MeV and $(17.8 \pm 0.5)\,\mu m$ at 3.95 MeV. The thickness calculated at a neutron energy of 2.95 MeV appears as an outlier. Excluding this value, the average thickness is determined to be $(18.1 \pm 0.2)\,\mu m$, significantly lower than the nominal thickness of 50 µm.

6.7 Proton conversion comparison

In addition to the comparison with the BF_3 counter, the number of identifiable neutrons were also compared to the number of protons. As the exact conversion factor from protons to neutrons in the ^{3}H-target is unknown for now, this is meant as a relative comparison between the detector contestants. Figure 6.7 shows the neutron counts per proton for all four neutron energies.

Due to the big uncertainty in the number of protons, the uncertainty in the conversion factor from protons to identifiable neutrons is also quite large. Nevertheless, the same relative factor between the sCVD and SiC detector as with

Die approbierte gedruckte Originalversion dieser Diplomarbeit ist an der TU Wien Bibliothek verfügbar
The approved original version of this thesis is available in print at TU Wien Bibliothek.

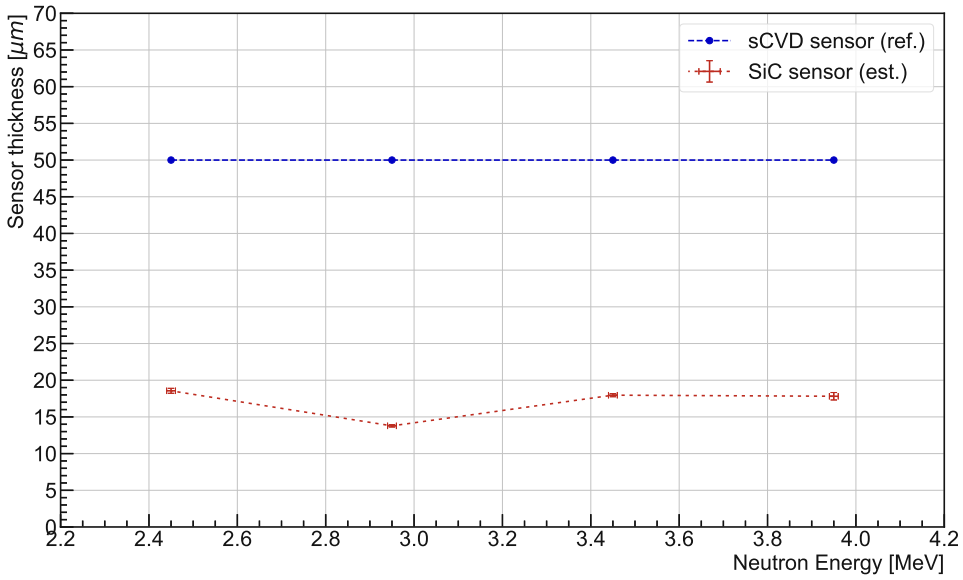

Figure 6.6: Calculated thickness of the active SiC sensor volume when using epsilon factors for both detectors and the nominal thickness of 50 µm for the sCVD detector as reference.

the BF_3 counter can be calculated. The exact values are listed in table 3.1 for the sCVD detector and in table 4.1 for the SiC detector. The conversion was at least 5.1 times higher for the sCVD detector at all neutron energies. This was in part because the Si fraction did not contribute to the neutron counts for the SiC detector and in part because of the thinner depletion zone of the SiC detector.

6.8 Identifiable neutron percentage comparison

The previous results show the detector thickness importance to the neutron detection efficiency. But scaling the thickness does also change the number of γ counts. Therefore, the percentage of identifiable neutron counts relative to all counts of the measured neutron response function is relevant. This identifiable neutron percentage is compared in figure 6.8 for both detector contestants at all four neutron energies.

From the comparison it is evident that the sCVD detector has an advantage, as its neutron identification percentage is higher than for the SiC detector. It can be explained by the higher γ-background sensitivity of the SiC detector compared to the sCVD detector. This imposes a limit on the use of SiC detectors for low

Die approbierte gedruckte Originalversion dieser Diplomarbeit ist an der TU Wien Bibliothek verfügbar
The approved original version of this thesis is available in print at TU Wien Bibliothek.

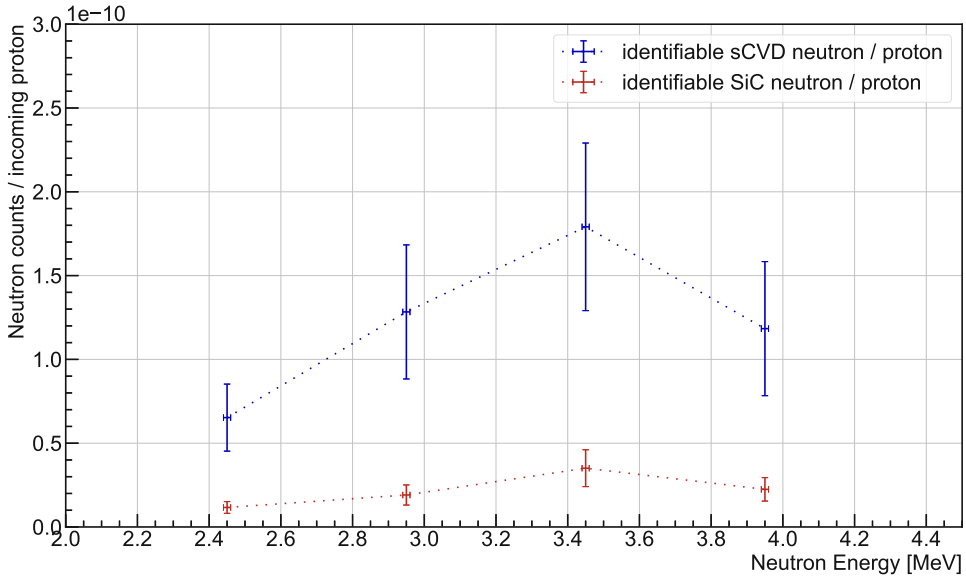

Figure 6.7: Comparison of the ratio of identified neutrons to the number of protons at all four investigated neutron energies for the sCVD (blue) and SiC (red) detector.

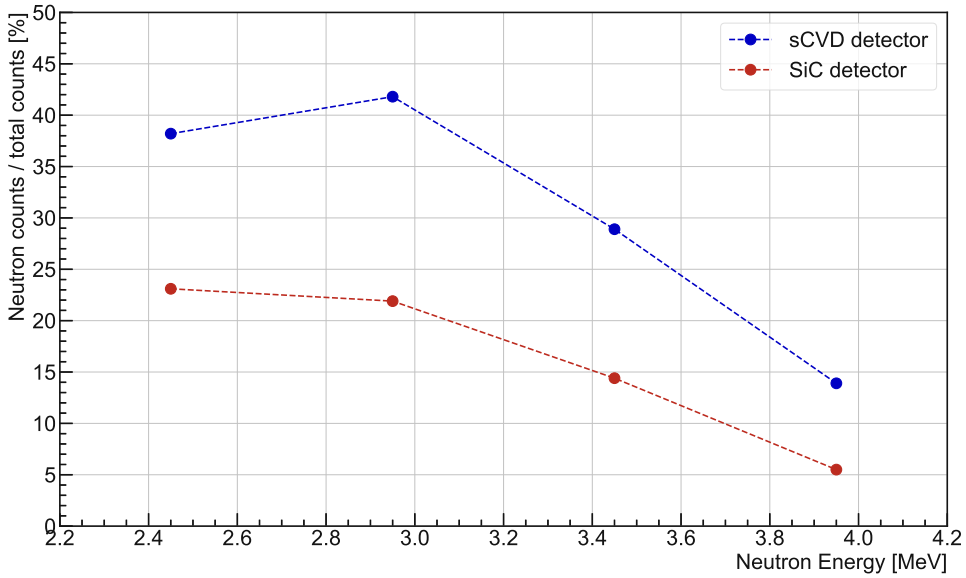

Figure 6.8: Comparison of the percentage of (identifiable) neutron counts relative to all detector counts of the measured neutron response functions.

Die approbierte gedruckte Originalversion dieser Diplomarbeit ist an der TU Wien Bibliothek verfügbar
The approved original version of this thesis is available in print at TU Wien Bibliothek.
TU Bibliothek Your knowledge hub WIEN

neutron fluxes in environments with a high γ-background.

6.9 Proton to Neutron conversion

One of the key parameters for precise efficiency calculation would be a well known conversion factor from protons to neutrons in the ^{3}H-target. Unfortunately these factors are unknown for now and therefore no efficiency calculations were performed. A step in the right direction can still be done by comparing the BF_3 counter, which is permanently installed at Demokritos, to the current integrator. The number of BF_3 counts per proton at all four neutron energies are shown in figure 6.9.

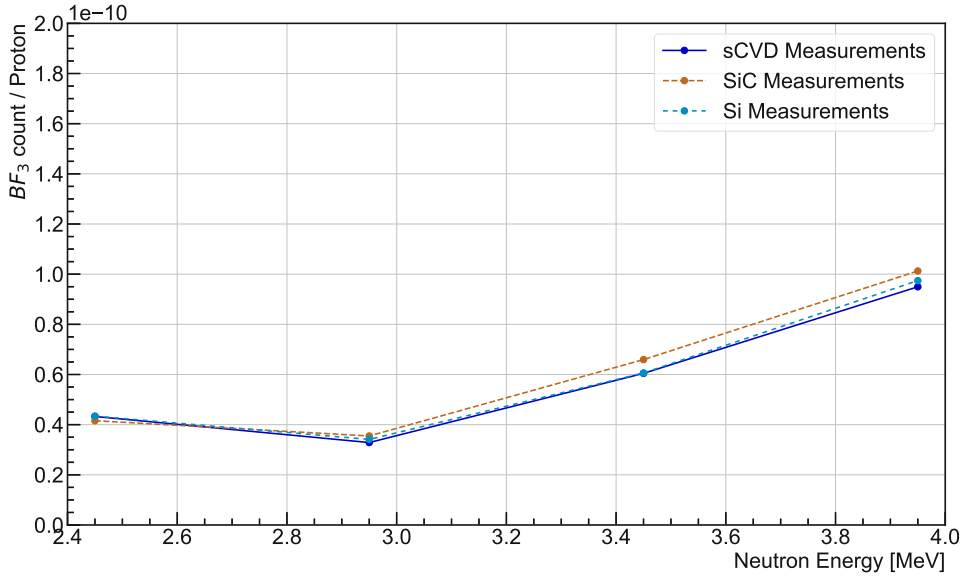

Figure 6.9: The number of BF_3 counts compared to the calculated number of protons from the current integrator.

The conversion factor is remarkably close for all measurements. Since the current integrator is known to have a large uncertainty, this suggests a systematic error that could be accounted for. The conversion factor is 4.27×10^{-11} at a neutron energy of 2.45 MeV, 3.42×10^{-11} at 2.95 MeV, 6.23×10^{-11} at 3.45 MeV and 9.79×10^{-11} at 3.95 MeV, respectively. Future research may provide an exact conversion factor, allowing efficiency measurements using the BF_3 counter and current integrator.

Die approbierte gedruckte Originalversion dieser Diplomarbeit ist an der TU Wien Bibliothek verfügbar
The approved original version of this thesis is available in print at TU Wien Bibliothek.
TU Bibliothek Your knowledge hub WIEN

6.10 Parasitic interactions

During the measurements with the SiC detector a peak at higher energies than the proton recoils was found. Figure 6.10 shows the four raw SiC response function. The data was re-binned to 11-bit in order to show the peak more prominently.

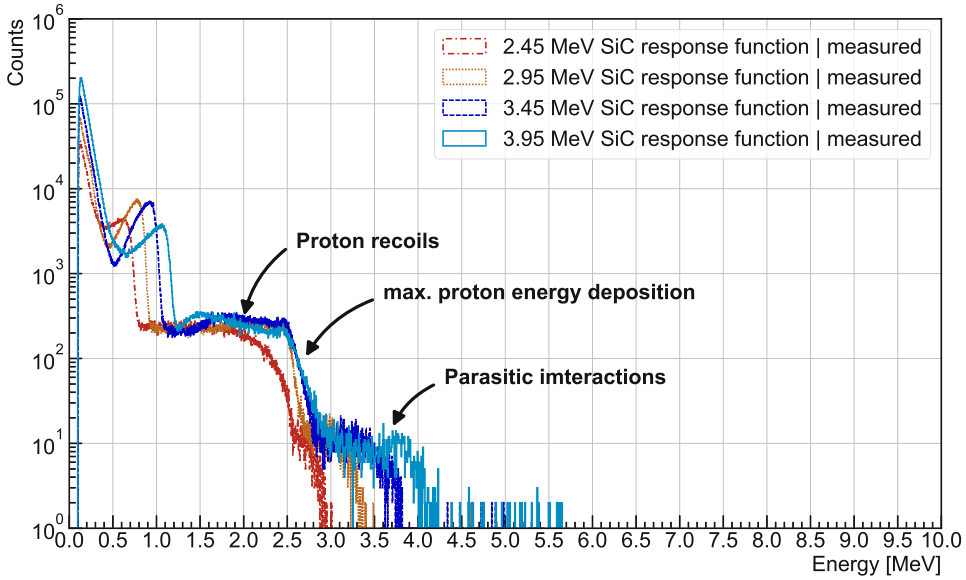

Figure 6.10: The raw SiC detector response functions at all four neutron energies, showing energy depositions at energies above the proton recoils.

Counts with a higher energy deposition than the respective proton recoils were recorded in all four measurements. To evaluate the Q-value of the parasitic interaction, the nominal neutron energy must be subtracted from the x-axis. The resulting energy spectra are shown in figure 6.11.

The peak is visible at all four measurements for the SiC detector up to Δ_E=400 keV compared to the respective neutron energy. The effect is also observed with the sCVD detector, but to a lesser extent. This is due to the fact that the proton recoils could deposit their full energy in the sCVD detector at all neutron energies, which obscures the parasitic interaction counts. The best distinction between the proton recoils and the peak was found for the SiC measurements at a neutron energy of 3.45 MeV and 3.95 MeV. Figure 6.12 shows the peak at a neutron energy of 3.45 MeV with a Gaussian fit to determine the mean energy and the maximum energy.

Die approbierte gedruckte Originalversion dieser Diplomarbeit ist an der TU Wien Bibliothek verfügbar
The approved original version of this thesis is available in print at TU Wien Bibliothek.

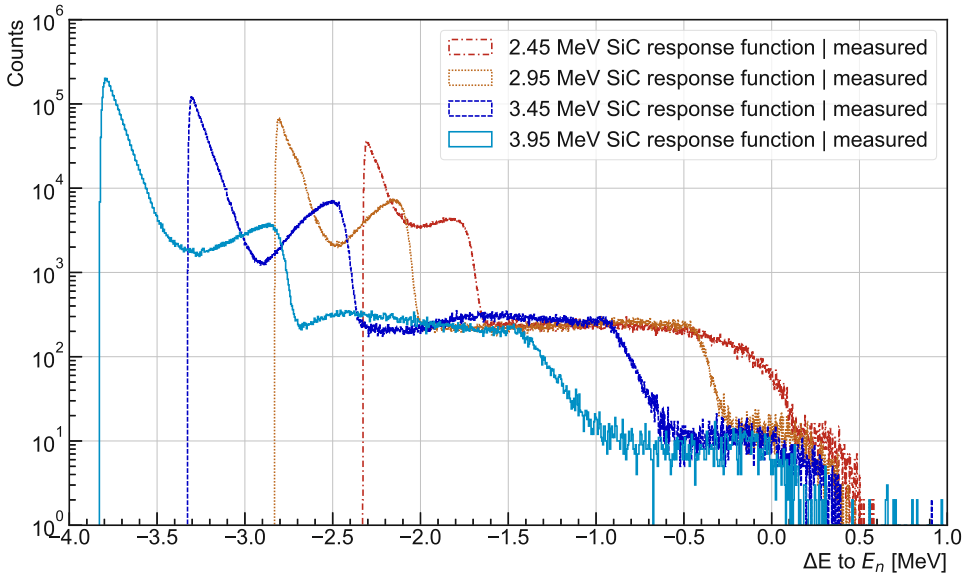

Figure 6.11: The SiC raw response functions at all four neutron energies, with their respective nominal neutron energy subtracted to evaluate the Q-value of the parasitic interaction.

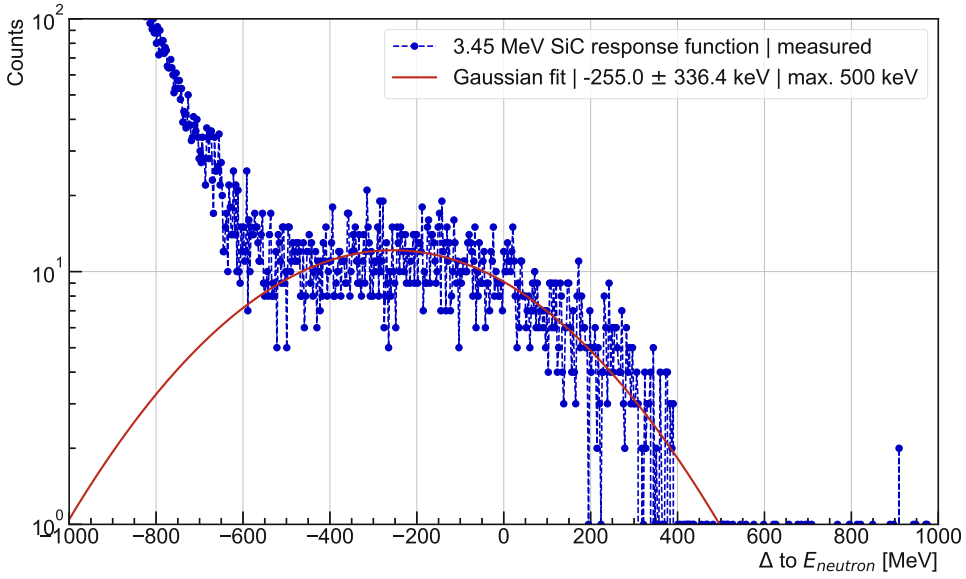

Figure 6.12: The peak of the parasitic effect at a neutron energy of 3.45 MeV with a Gaussian fit at (-255 ± 336) keV, with its maximum at 500 keV.

Die approbierte gedruckte Originalversion dieser Diplomarbeit ist an der TU Wien Bibliothek verfügbar
The approved original version of this thesis is available in print at TU Wien Bibliothek.

The Gaussian fit results in an energy estimation of (-255 ± 336) keV. As particles from an interaction can only lose energy and not gain any, the maximum energy deposition from the Gaussian fit at 500 keV must be taken into account. After investigating all possible materials surrounding the SiC and sCVD detector, the best reaction candidates were determined to be $^{14}N(n,\alpha)^{11}B$, Q = (-157.889 ± 0.012) keV, and $^{14}N(n,p)^{14}C$, Q = (625.871 ± 0.004) keV, as both detectors have a small amount of air between the PCB and the sensor itself, the Nitrogen in the air would be sufficient [23, 24].

The highest energy depositions are consequently a result form the $^{14}N(n,p)^{14}C$ reaction rather than the $^{14}N(n,\alpha)^{11}B$ reaction. As previously discussed, protons with the neutron energy can not deposit their full energy in the SiC sensor. Therefore the protons from the $^{14}N(n,p)^{14}C$ reaction, which would have an higher energy due to its Q-value, can not deposit their full energy as well. Therefore, and because of the higher total cross-section of $^{14}N(n,\alpha)^{11}B$, the Gaussian peak is likely the result from it rather than the $^{14}N(n,p)^{14}C$ reaction. Thus, both interactions are required to explain the shape of the parasitic interaction counts.

Assuming a precisely defined amount and layer thickness of nitrogen between the neutron source and the detector, these interactions could be used in future neutron facilities to cross-check the determined neutron energy. More research and measurements are needed to determine the usefulness of these in combination with solid-state detectors for neutron diagnostic applications.

Die approbierte gedruckte Originalversion dieser Diplomarbeit ist an der TU Wien Bibliothek verfügbar
The approved original version of this thesis is available in print at TU Wien Bibliothek.
TU Bibliothek Your knowledge hub WIEN

Chapter 7

Conclusion

The neutron response functions of a sCVD, SiC and Si detector to monoenergetic neutron beams with an energy of 2.45 MeV, 2.95 MeV, 3.45 MeV and 3.95 MeV were investigated at the NCSR Demokritos facility. GEANT4 simulations were conducted for comparison with the measurements and the complete experimental process was outlined in detail. This includes the theoretical aspects of solid-state detectors, the development of a new amplifier and digitiser and the processing of the detector response functions to measured neutron response functions. This enabled the comparison of the three detector contestants relative to a BF_3 reference detector and the number of protons in the Tandem accelerator.

In summary, the key results of the investigation are:

1. A threshold energy needs to be used to distinguish neutron from γ counts.
2. Proton recoils can either be used to determine the neutron energy or should be avoided otherwise.
3. A Si detector can not be used for neutron flux measurements.
4. The Si fraction in a SiC detector does not contribute to the number of identifiable neutrons.
5. The sCVD detector demonstrates the highest neutron-to-γ ratio.
6. Parasitic interaction counts were identified and investigated.
7. A discrepancy was observed between the nominal and the actual thickness of the SiC sensor.
8. A strong correlation between the BF_3-counter and the current integrator was identified.

Die approbierte gedruckte Originalversion dieser Diplomarbeit ist an der TU Wien Bibliothek verfügbar
The approved original version of this thesis is available in print at TU Wien Bibliothek.
TU Bibliothek Your knowledge hub WIEN

9. Small deviations from the simulated neutron energy distributions were discovered.

After analysing the twelve different detector response functions and comparing them with their respective GEANT4 simulations, it was evident that the significant deviation of the measurement results from the GEANT4 simulations at low energies can only be attributed to a strong γ background. To distinguish between neutron and γ counts, a threshold is needed, above which all entries are counted as identifiable neutron counts. This threshold was set to be at the valley of the angular distribution for all sCVD and SiC response functions.

The proton recoils can be used as a secondary neutron energy measurement tool if the thickness of the detector is sufficient for them to deposit their full energy. Otherwise, if the thickness is not sufficient, they should be avoided. If proton recoils are present, they need to be taken into account and further simulations are required to estimate their impact.

The Si detector response function provided no feature in its spectrum to distinguish between neutrons, the proton recoils and the γ-background. This can be explained by the theoretical angular distribution of ^{28}Si, which has no structural features comparable to the angular distribution of ^{12}C. Moreover, the γ-sensitivity is another disadvantage for direct neutron measurements. Therefore, the Si detector is the least favourable of the contestants for fusion neutron diagnostics.

The SiC neutron response function consists of counts from ^{12}C and ^{28}Si. Due to the cut-off energy of the ^{28}Si being below the threshold energy used to discriminate neutrons from γ, all neutron counts coming from an interaction with ^{28}Si do not contribute to the number of identifiable neutrons. This reduces the percentage of identifiable neutron counts compared to the overall number. This imposes a limit on the use of SiC detectors for low neutron fluxes in environments with a high γ-background.

By comparing the number of identifiable neutrons to the reference BF_3 counter, the relative factor ϵ was calculated for all SiC and sCVD measurements. The ϵ-factor was significantly higher for the sCVD detector compared to the SiC detector. This corresponds directly to the neutron sensitivity of the detector, which is needed for future neutron applications. The disadvantage of SiC compared to sCVD can only be overcome by a thicker SiC detector, which would increase the deposited energy from the γ-background, which should be avoided. Therefore, a sCVD detector is preferred over a SiC detector for precision neutron flux and energy measurements in the presence of a considerable γ-background. As a result,

Die approbierte gedruckte Originalversion dieser Diplomarbeit ist an der TU Wien Bibliothek verfügbar
The approved original version of this thesis is available in print at TU Wien Bibliothek.
TU Bibliothek Your knowledge hub WIEN

the sCVD detector is considered to be the most promising candidate for future applications in fusion technology.

Counts from parasitic $^{14}N(p,\alpha)^{11}B$ and $^{14}N(n,p)^{14}C$ reactions were present in the data for the sCVD and SiC detector. A Gaussian shaped peak at a constant offset to the neutron energy was present and investigated. The Q-value was determined using a Gaussian fit to be $(-255 \pm 336)\,\mathrm{keV}$ compared to its Q-value of $(-157.889 \pm 0.012)\,\mathrm{keV}$ for the $^{14}N(p,\alpha)^{11}B$ reaction. The energy deposition up to 400 keV can be explained by the $^{14}N(n,p)^{14}C$ reaction, which has a Q-value of $\mathrm{Q} = (625.871 \pm 0.004)\,\mathrm{keV}$. These interactions could be used in future neutron measurements to obtain an additional calibration point for determining the neutron energy.

The measured thickness of the sensitive SiC volume was found to be approximately 18 µm, significantly less than its nominal value of 50 µm. This discrepancy is particularly important because many current studies on SiC detectors reference the nominal thickness when evaluating the detector efficiency. Consequently, comparing SiC detectors to sCVD detectors with identical neutron flux can serve as an indirect method for assessing the actual thickness of the SiC sensor.

A strong correlation was identified between the BF_3-counter and the current integrator measurements. Once calibrated, these instruments could potentially function as a neutron flux monitor for approximate neutron flux estimations. This calibration could help reduce the large error margins currently associated with the current integrator readings.

Using the simulated neutron spectra for Demokritos was tremendously useful and resulted in correct calibrated neutron response function. Nevertheless, small deviations in the conversion factor from mV to MeV can only be explained by a small deviation of the real neutron energy distribution from the simulation.

In summary, the lack of any feature in the Si neutron response function and its high γ sensitivity excludes it as contestant for neutron applications within fusion reactors. In contrast, the sCVD diamond detector is preferred over the SiC detector due to its superior efficiency in discriminating between neutron counts and the γ background - a critical aspect for nuclear fusion applications.

Die approbierte gedruckte Originalversion dieser Diplomarbeit ist an der TU Wien Bibliothek verfügbar
The approved original version of this thesis is available in print at TU Wien Bibliothek.
TU Bibliothek Your knowledge hub WIEN

Acknowledgement

This work would not have been possible without the contributions of many people. I hope to include everyone, but if I miss someone, I apologise deeply. First, a huge thanks to CIVIDEC Instrumentation for providing the opportunity to conduct these measurements and for supplying the necessary equipment. A special thanks to Erich Griesmayer and Christina Weiss, who taught me almost everything I know about solid-state detectors and how to use them at all for conducting a measurement. Their support was crucial from the development of the digitiser to the data analysis, and even in reviewing and refining this thesis. And of course I also want to thank Theodor Fragner, my colleague, who I had many discussion with during the development of the data aquistion system.

I also want to thank the entire team at Demokritos. The measurements would not have been feasible without their dedication and support. They often worked extra hours during our measurement campaign to maximise our data collection. A special mention goes to Maria Diakaki for her support and Kalli Kaperoni for her work on the neutron energy distribution simulations, which were one of the key elements for the analysis of the data, and the discussions we had about the data analysis. Also a special thanks to Michael Kokkoris and Michail Axiotis. You all turned our visit to Demokritos into a wonderful time, and it was only during our discussion during the measurements that the parasitic interaction was identified.

Last but not least, I want to thank my supervisors at TU Wien, Stephan Sponar and Erwin Jericha. They not only accepted my thesis topic but also provided invaluable guidance throughout the writing process. Our meetings and discussions were essential in shaping this thesis into its present form

Furthermore, a big thank you to my family and especially to my girlfriend, who somehow tolerated my constant talking about this work. Again, thank you to all people who supported this work, it was quite frankly a team effort.

Die approbierte gedruckte Originalversion dieser Diplomarbeit ist an der TU Wien Bibliothek verfügbar
The approved original version of this thesis is available in print at TU Wien Bibliothek.

Bibliography

[1] L. Bertalot et al., "Fusion neutron diagnostics on iter tokamak", Journal of Instrumentation **7**, C04012 (2012).

[2] *National Centre For Scientific Research Demokritos – Official Web Site*, https://www.demokritos.gr/ (visited on 12/09/2023).

[3] *CIVIDEC Instrumentation - CVD Diamond Technology applications*, https://cividec.at/electronics-Cx-L.html (visited on 12/12/2023).

[4] A. V. Krasilnikov et al., "Status of ITER neutron diagnostic development", Nucl. Fusion **45**, 1503–1509 (2005).

[5] C. W. Barnes et al., "Neutron activation for ITER", Rev. Sci. Instrum. **68**, 577–580 (1997).

[6] U. Woźnicka, "Review of Neutron Diagnostics Based on Fission Reactions Induced by Fusion Neutrons", J. Fusion Energy **38**, 376–385 (2019).

[7] J. Hartman et al., "Measurements of response functions of EJ-299-33A plastic scintillator for fast neutrons", Nucl. Instrum. Methods Phys. Res. A: Accel. Spectrom. Detect. Assoc. Equip. **804**, 137–143 (2015).

[8] R. Adams et al., "A novel fast-neutron tomography system based on a plastic scintillator array and a compact D-D neutron generator." Appl. Radiat. Isot. **107**, 1–7 (2016).

[9] Yu.A. Kaschuck et al., "Neutron measurements during trace tritium experiments at jet using a stilbene detector", in Proc. 31st eps conference on plasma phys, london (2004).

[10] L. Bertalot et al., "Neutron energy measurements of trace tritium plasmas with ne213 compact spectrometer at jet", in Proceedings of 32nd eps conf. taragona p1-078 (2005).

[11] Xu Xie et al., "Application of a single crystal chemical vapor deposition diamond detector for deuteron plasma neutron measurement", Nucl. Instrum. Methods Phys. Res. A: Accel. Spectrom. Detect. Assoc. Equip. **761**, 28–33 (2014).

Die approbierte gedruckte Originalversion dieser Diplomarbeit ist an der TU Wien Bibliothek verfügbar
The approved original version of this thesis is available in print at TU Wien Bibliothek.
TU Bibliothek Your knowledge hub WIEN

[12] M. Pillon et al., "Experimental response functions of a single-crystal diamond detector for 5–20.5 MeV neutrons", Nucl. Instrum. Methods Phys. Res. A: Accel. Spectrom. Detect. Assoc. Equip. **640**, 185–191 (2011).

[13] Liu, J., Jiang, H., Cui, Z. et al., "Simultaneous measurement of energy spectrum and fluence of neutrons using a diamond detector", Sci. Rep. **12**, 10.1038/s41598-022-16235-x (2022).

[14] G. Ericsson, "Advanced Neutron Spectroscopy in Fusion Research", J. Fusion Energy **38**, 330–355 (2019).

[15] M. Rebai et al., "New thick silicon carbide detectors: Response to 14 MeV neutrons and comparison with single-crystal diamonds", Nucl. Instrum. Methods Phys. Res. A: Accel. Spectrom. Detect. Assoc. Equip. **946**, 162637 (2019).

[16] F. Franceschini and F. H. Ruddy, "Silicon Carbide Neutron Detectors", 10.5772/15666 (2011).

[17] *DEMO*, https://euro-fusion.org/programme/demo/ (visited on 12/27/2023).

[18] W. Biel et al., "Diagnostics for plasma control – from ITER to DEMO", Fusion Eng. Des. **146**, 465–472 (2019).

[19] E. Gatti, E. Gatti, and P. F. Manfredi, "Processing the signals from solid-state detectors in elementary-particle physics", Rivista Del Nuovo Cimento **9**, 1–146 (1986).

[20] W. Shockley, "Currents to Conductors Induced by a Moving Point Charge", J. Appl. Phys. **9**, 635–636 (1938).

[21] P. Kavrigin et al., "Pulse-shape analysis for gamma background rejection in thermal neutron radiation using CVD diamond detectors", Nucl. Instrum. Methods Phys. Res. A: Accel. Spectrom. Detect. Assoc. Equip. **795**, 88–91 (2015).

[22] L. D. Landau, "On the energy loss of fast particles by ionization", J. Phys. **8**, 201–205 (1944).

[23] M. Wang et al., "The AME 2020 atomic mass evaluation (II). Tables, graphs and references*", Chinese Phys. C, 10.1088/1674-1137/abddaf (2021).

[24] W.J. Huang et al, "The AME 2020 atomic mass evaluation (I). Evaluation of input data, and adjustment procedures", Chinese Phys. C, 10.1088/1674-1137/abddb0 (2021).

[25] D. A.Brown et al., "ENDF/B-VIII.0: The 8th Major Release of the Nuclear Reaction Data Library with CIELO-project Cross Sections, New Standards and Thermal Scattering Data", Nucl. Data Sheets, Special Issue on Nuclear Reaction Data **148**, 1–142 (2018).

Die approbierte gedruckte Originalversion dieser Diplomarbeit ist an der TU Wien Bibliothek verfügbar
The approved original version of this thesis is available in print at TU Wien Bibliothek.
TU Bibliothek Your knowledge hub WIEN

[26] B. Wirtz, "Semiconductors And Semimetals", 10.1016/s0080-8784(08)62457-6 (2016).

[27] A. Einstein, "Über einen die erzeugung und verwandlung des lichtes betreffenden heuristischen gesichtspunkt", Annalen der Physik **17**, 132 (1905).

[28] A. H. Compton, "A Quantum Theory of the Scattering of X-rays by Light Elements", Phys. Rev. **21**, 483–502 (1923).

[29] J. R. Oppenheimer, Milton S. Plesset, M. S. Plesset, and M. S. Plesset, "On the Production of the Positive Electron", Phys. Rev. **44**, 53–55 (1933).

[30] J. H. Hubbell and S. M. B. Seltzer, "XCOM : Photon Cross Sections Database", https://dx.doi.org/10.18434/T48G6X (2005).

[31] Marzio De Napoli and M. De Napoli, "SiC detectors: A review on the use of silicon carbide as radiation detection material", Front. Phys. **10**, 10.3389/fphy.2022.898833 (2022).

[32] H. Pernegger et al., "Charge-carrier properties in synthetic single-crystal diamond measured with the transient-current technique", Journal of Applied Physics **97**, 073704 (2005).

[33] F. Bachmair, "CVD diamond sensors in detectors for high energy physics", PhD thesis (ETH Zurich, 2016).

[34] H. G. Moser, H. G. Moser, and H. G. Moser, "Silicon detector systems in high energy physics", Prog. Part. Nucl. Phys. **63**, 186–237 (2009).

[35] *ROSY*, https://cividec.at/electronics-E2.html (visited on 12/07/2023).

[36] *Multiprocessing.shared_memory — Shared memory for direct access across processes*, https://docs.python.org/3/library/multiprocessing.shared_memory.html (visited on 12/12/2023).

[37] Charles R. Harris et al., "Array programming with NumPy", Nature **585**, 357–362 (2020).

[38] S. K. Lam, A. Pitrou, and S. Seibert, "Numba: a llvm-based python jit compiler", in Proceedings of the second workshop on the llvm compiler infrastructure in hpc, LLVM '15 (2015).

[39] P. T. Inc., *Collaborative data science*, (2015) https://plot.ly.

[40] The HDF Group, *Hierarchical Data Format, version 5*, https://github.com/HDFGroup/hdf5.

[41] *Silx 2.0.0 — silx 2.0.0 documentation*, https://www.silx.org/doc/silx/latest/ (visited on 02/02/2024).

[42] *HDF5 for Python*, https://www.h5py.org/ (visited on 02/02/2024).

Die approbierte gedruckte Originalversion dieser Diplomarbeit ist an der TU Wien Bibliothek verfügbar
The approved original version of this thesis is available in print at TU Wien Bibliothek.
TU Bibliothek Your knowledge hub WIEN

[43] S. Agostinelli et al., "Geant4—a simulation toolkit", Nucl. Instrum. Methods Phys. Res. A: Accel. Spectrom. Detect. Assoc. Equip. **506**, 250–303 (2003).

[44] J. Allison et al., "Geant4 developments and applications", IEEE Trans. Nucl. Sci. **53**, 270–278 (2006).

[45] J. Allison et al., "Recent developments in geant4", Nucl. Instrum. Methods Phys. Res. A: Accel. Spectrom. Detect. Assoc. Equip. **835**, 186–225 (2016).

[46] R. Vlastou, "The neutron facility at NCSR 'Demokritos' and neutron activation research activities of NTUA", EPJ tech. instrum., 10.1140/epjti/s40485-023-00091-8 (2023).

[47] E. Birgersson, G. Lovestam, et al., "Neusdesc-neutron source description software manual", JRC Scientific and Technical Reports (2009).

[48] A. Deruytter and P. Pelfer, "Precise determination of the branching ratio and Q-value of the ^{10}B(n,α_0)^{7}Li reaction and of the Q-value of the $^6Li(n,\alpha)^3$H reaction", J. Nucl. Energy **21**, 833–845 (1967).

[49] F.-J. Hambsch and I. Ruskov, "The ^{10}B(n,α_0)^{7}Li and ^{10}B(n,$\alpha_1\gamma$)^{7}Li Alpha-Particle Angular Distributions for En $<$ 1 MeV", Nucl. Sci. Eng. **163**, 1–16 (2009).

Die approbierte gedruckte Originalversion dieser Diplomarbeit ist an der TU Wien Bibliothek verfügbar
The approved original version of this thesis is available in print at TU Wien Bibliothek.

List of Figures

Die approbierte gedruckte Originalversion dieser Diplomarbeit ist an der TU Wien Bibliothek verfügbar
The approved original version of this thesis is available in print at TU Wien Bibliothek.
TU Bibliothek Your knowledge hub WIEN

Die approbierte gedruckte Originalversion dieser Diplomarbeit ist an der TU Wien Bibliothek verfügbar
The approved original version of this thesis is available in print at TU Wien Bibliothek.
TU Bibliothek Your knowledge hub WIEN

Die approbierte gedruckte Originalversion dieser Diplomarbeit ist an der TU Wien Bibliothek verfügbar
The approved original version of this thesis is available in print at TU Wien Bibliothek.
TU Bibliothek Your knowledge hub WIEN

Die approbierte gedruckte Originalversion dieser Diplomarbeit ist an der TU Wien Bibliothek verfügbar
The approved original version of this thesis is available in print at TU Wien Bibliothek.
TU Bibliothek Your knowledge hub WIEN

Die approbierte gedruckte Originalversion dieser Diplomarbeit ist an der TU Wien Bibliothek verfügbar
The approved original version of this thesis is available in print at TU Wien Bibliothek.
TU Bibliothek Your knowledge hub WIEN

Die approbierte gedruckte Originalversion dieser Diplomarbeit ist an der TU Wien Bibliothek verfügbar
The approved original version of this thesis is available in print at TU Wien Bibliothek.

List of Tables

Die approbierte gedruckte Originalversion dieser Diplomarbeit ist an der TU Wien Bibliothek verfügbar
The approved original version of this thesis is available in print at TU Wien Bibliothek.
TU Bibliothek Your knowledge hub WIEN